UNIVERSITÀ DEGLI STUDI DI NAPOLI “FEDERICO II”

Scuola Politecnica e delle Scienze di Base

Area Didattica di Scienze Matematiche Fisiche e Naturali

Dipartimento di Fisica “Ettore Pancini”

Laurea Magistrale in Fisica

Measurements of tunnel-ferromagnetic Josephson devices: transport and magnetic properties towards the ferrotransmon qubit

Relatori:
Prof. Francesco Tafuri
Dr. Davide Massarotti
Dr. Roberta Satariano

Candidato:
Gianpasquale Tuccillo
Matr. N94000673

Anno Accademico 2023/2024

Contents

Introduction

Superconducting hybrid circuits represent a promising frontier of solid state physics, superconducting electronics and, more recently, in the field of quantum computation, possibly contributing to enlarge the platform of potential devices for quantum circuits. Among the most successful quantum devices, the split transmon has a great relevance due to its tunability and robust coherence properties. However, its reliance on Superconducting Quantum Interference Device (SQUID) introduces limitations such as flux noise, crosstalk, and scalability issues. Addressing these challenges has become a central focus of research in quantum technologies. This thesis presents a novel superconducting hybrid circuit architecture, referred to as the ferrotransmon, designed to address some limitations of the split transmon qubit by replacing SQUID loops with a Superconductor-Insulator-Superconductor-Ferromagnet-Superconductor (SIsFS) junction. In this work, we propose using a NiFeGdNb ferromagnetic alloy as the F layer to enable tunability of qubit frequency through localized in-plane magnetic fields, thereby potentially eliminating the need for traditional SQUID elements and improving coherence, noise suppression, and scalability. A key innovation lies in the integration of on-chip Helmholtz coil structures, which provide precise control of the in-plane magnetic field - crucial for the ferro-trasmon architecture. This approach bridges material science and circuit engineering to advance quantum computing platforms. In the first chapter, we will establish foundational principles of superconductivity and quantum circuits, with a focus on the physics of Josephson junctions and their critical role in qubit design. We will introduce the transmon qubit as a backbone architecture while systematically addressing limitations inherent in SQUID-based systems, such as flux noise and design complexity. In the second chapter, we present ferromagnetic Josephson junctions and their relevance to the proposed design. Specifically, the properties of SIsFS junctions, which combine superconducting and ferromagnetic materials to achieve tunable magnetic properties. The theoretical framework for understanding these junctions will be described, along with the potential benefits they bring to superconducting qubits in terms of coherence and tunability. In the third chapter, the experimental apparatus, fabrication techniques, and characterization protocols central to this work will be outlined. We will demonstrate the progress of SIsFS junctions, focusing on the growth of the ferromagnetic barrier, an alloy of NiFeGdNb alloys, employing state-of-the-art thin-film deposition techniques. We aim to systematically detail the methodologies we employed, including analytical techniques for investigating the chemical and structural characterization, as well as vibrating sample magnetometry (VSM) to assess the magnetic properties of these films. Particular attention is given to the dilution cryostat setup used for low-temperature measurements. In the fourth chapter, we present the outcomes of our experimental measurements, including the transport properties of SIsFS junctions, vibrating sample magnetometry (VSM) data to characterize the ferromagnetic properties of NiFeGdNb alloys, and critical current modulation in response to magnetic fields generated by both an external coil and a on-chip Helmholtz coil. Together, these results validate the compatibility of SIsFS ferromagnetic junctions with quantum circuits in terms of dissipation and energy scales. The key result is the identification of a ferromagnetic alloy that enables on-chip control of these junctions, further supported by measurements using on-chip Helmholtz coil structures. These findings represent fundamental steps toward the experimental validation of the ferrotransmon. By replacing SQUID-based architectures with a hybrid Josephson junction that incorporates ferromagnetic elements, this layout will pave the way for enhanced qubit control, noise suppression, and coherence.

Chapter 1

Conventional Josephson Junctions

In this chapter, we will provide the basic concepts on the Josephson effect and establish the terminology that we will refer to throughout this thesis. We will examine the primary features and behaviors of standard Josephson junctions in preparation for discussing the unusual behavior of hybrid ferromagnetic Josephson junctions in future chapters. Initially, we will briefly revisit the fundamental principles of superconductivity, followed by an introduction to the Josephson effect, particularly examining transport properties and the electrodynamics of Josephson junctions as a function of the temperature and magnetic fields. Additionally, the chapter will be completed with an exploration of the pivotal role of Josephson junctions within superconducting quantum circuits.

1.1 Notes on superconductivity

Superconductive materials below a critical temperature and a lower critical field, exhibit properties of zero resistivity and ideal diamagnetism. Zero resistivity was first observed by Kamerlingh Onnes in 1911 in an experiment involving mercury cooled down to $4.15K$ with liquid helium. At that temperature, mercury lost its dissipative property and entered a state where the electric current could flow without any voltage drop (Figure 1.1).

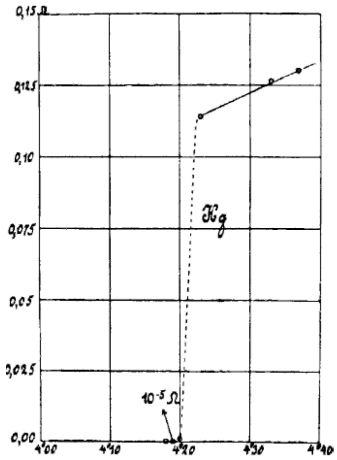

Figure 1.1: Sudden drop in resistivity at a critical temperature T_c.

An additional phenomenon noted in this novel state is the expulsion of magnetic field lines from the substance, demonstrating perfect diamagnetism, a discovery made by Meissner and Ochsenfeld, as shown in Figure 1.2. This phenomenon, later named the *Meissner effect*, remains independent of thermal history, distinguishing superconductors from ideal conductors. Consequently, superconductors cannot be categorized as such.

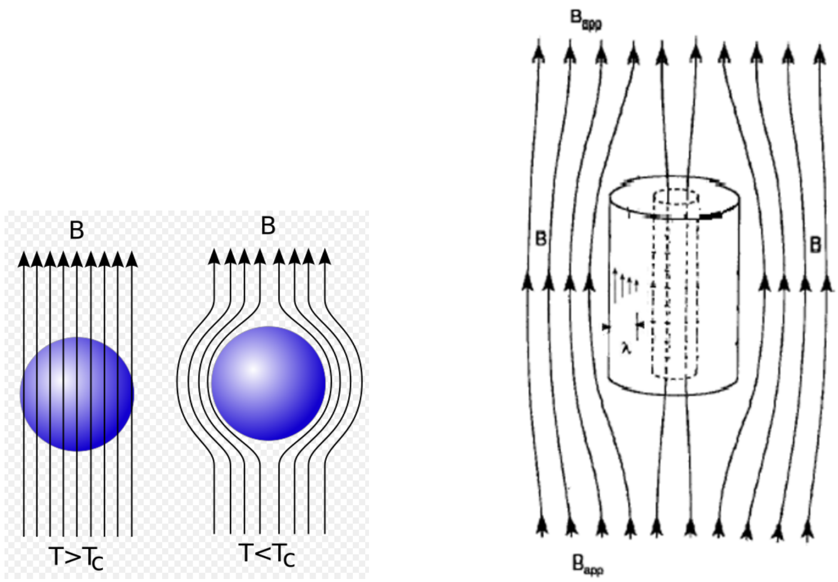

Figure 1.2: **a)**Diagram of the Meissner effect. Magnetic field lines, represented as arrows, are expelled from a superconductor when it is below its critical temperature. **b)** Illustration of field lines for a hollow cylinder and the attenuation of the magnetic field within a cylindrical superconductor.

Geometry is also a relevant factor when it comes to the behavior of a superconductor; a number of experiments [1] have proven that magnetic flux related to field lines through a hollow cylinder (Figure 1.2) can only assume values that are

integral multiples of the *magnetic flux quantum* $\Phi_0 = \frac{hc}{2e}$.
The phenomenon of complete diamagnetism and the absence of electrical resistance in superconductors were formulated in the theoretical framework developed by Fritz and Heinz London in 1935 [2]. Their work, now known as the London theory, provided a phenomenological approach to superconductivity based on a few fundamental assumptions. First, London theory assumes that in the superconducting state, electrons form a coherent quantum state characterized by a macroscopic wave function, typically denoted ψ. This wavefunction represents the collective behavior of superconducting charge carriers and can be expressed as $\psi = |\psi|e^{i\varphi}$, where $|\psi|^2$ corresponds to the *superfluid density*, or the density of electrons that contribute to superconductivity, and φ is the phase of the wavefunction. Importantly, the magnitude of the reaction remains constant below the critical temperature T_C, signifying the onset of superconductivity. The second key assumption is that superconducting electrons respond to external electromagnetic fields in a unique way. Specifically, they proposed that any electric field $\vec{E}$ within the superconductor generates a time-dependent current density $\vec{J_S}$, given by:

$$\frac{\partial \mathbf{J}_S}{\partial t} = \frac{|\psi|^2 e^2}{m}\mathbf{E}, \tag{1.1}$$

The equation indicates that in a superconductor, the electric field $\vec{E}$ drives the current density $\vec{J_S}$ without resistance. Unlike normal conductors, where Ohm's law governs a steady-state current accompanied by resistive losses, superconductors show a non-dissipative behavior, enabling $\vec{J_S}$ to rise as $\vec{E}$ is applied, without any attenuation. The second London equation provides insight into the magnetic behavior of superconductors as expressed by:

$$\nabla \wedge \mathbf{J}_S = \frac{|\psi|^2 e^2}{mc}\mathbf{B} = 0, \tag{1.2}$$

This equation is fundamental to explain the Meissner effect, the expulsion of magnetic field lines from the interior of a superconductor. According to this equation, the presence of a magnetic field inside a superconductor induces a circulating current density that opposes and effectively cancels out the field within the material. The magnetic field thus decays over a characteristic length known as the *London penetration depth* λ_L [1], which is a measure of how far the magnetic field can penetrate into the superconductor before it diminishes to zero, as shown in Figure 1.2:

$$\lambda_L^2 = \frac{|\psi|^2 4\pi e^2}{me^2}, \tag{1.3}$$

Although London's theory has achieved certain successes, it also faces substantial drawbacks. It does not possess a microscopic basis, meaning it fails to elucidate the cause of superconductivity or its dependence on temperature. Furthermore, London's theory becomes invalid near the critical temperature T_C and is unable to describe the mixed state found in Type II superconductors, where magnetic flux partially penetrates the material in quantized vortices. These limitations prompted the development of more thorough theories. The Ginzburg-Landau theory, formulated by Vitaly Ginzburg and Lev Landau [3], expands upon London's framework by introducing a free energy functional that relies on a spatially varying order parameter $\psi(\vec{r})$. The equations derived from this functional characterize the superfluid density and coherence length, providing a thermodynamic perspective on superconductivity. Complementing the Ginzburg-Landau model, the BCS theory, formulated by John Bardeen, Leon Cooper, and Robert Schrieffer, provides a microscopic view of superconductivity. BCS theory elucidates the formation of electron pairs (*Cooper pairs*) owing to an attractive interaction facilitated by lattice vibrations, resulting in a condensate with an energy gap that inhibits resistive scattering. This theory successfully accounts for the temperature dependence of the superfluid density, the energy gap, and the emergence of quantized magnetic flux, thereby serving as the cornerstone of contemporary superconductivity theory. It was later extended by *Gor'kov* [4] and *P. W. Anderson* [5]. In 1959, Gor'kov demonstrated that the GL equations could be deduced from the microscopic theory, reformulated using Green functions to handle inhomogeneity [6].

The Landau theory of second order phase transitions is based on an expansion of the free energy in powers of the order parameter ψ, which is small near the transition temperature:

$$F = F_{n_0} + \int \left\{ \frac{\mathbf{B}^2}{8\pi} + \frac{\hbar^2}{4m} \left| \left(\nabla - \frac{2ie}{\hbar c} \mathbf{A} \right) \psi \right|^2 + \alpha |\psi|^2 + \frac{\beta}{2} |\psi|^4 \right\} dV, \tag{1.4}$$

Here, α and β are temperature-dependent coefficients, $\mathbf{A}$ is the magnetic vector potential, and F_{n_0} is the free energy of the normal state. The parameters α and β determine the superconducting state, with $\alpha = \alpha_0(T - T_c)$.

Minimizing the free energy with respect to ψ and $\mathbf{A}$ leads to the GL equations 1.5 and 1.6 [7]:

$$\frac{1}{4m} \left(-i\hbar\nabla - \frac{2e}{c} \mathbf{A} \right)^2 \psi + \alpha\psi + \beta|\psi|^2\psi = 0, \tag{1.5}$$

$$\mathbf{j} = -\frac{ie\hbar}{2m} \left(\psi^* \nabla \psi - \psi \nabla \psi^* \right) - \frac{4e^2}{mc} |\psi|^2 \mathbf{A}, \tag{1.6}$$

with $\mathbf{j}$ being the current density. These coupled equations enable the assessment of the spatial variation of ψ and $\vec{j}$. Additionally, they provide a basis for introducing the concept of coherence length:

$$\xi = \sqrt{\frac{\hbar^2}{2m|\alpha_0(T_c - T)|}}, \tag{1.7}$$

$$\lambda(T) = \sqrt{\frac{mc^2\beta}{8\pi e^2 \alpha_0 (T_c - T)}}. \tag{1.8}$$

In particular, the coherence length ξ, is a fundamental parameter in the Ginzburg-Landau theory of superconductivity. It characterizes the spatial extent over which

the superconducting order parameter ψ, can vary significantly. Physically, ξ represents the distance over which Cooper pairs maintain phase coherence. This parameter is essential in the macroscopic portrayal of superconductivity within the framework of G.L. theory. Nevertheless, a shortcoming of G.L. theory is its lack of a microscopic explanation for the phenomenon. The BCS (Bardeen-Cooper-Schrieffer) theory overcomes this limitation by offering a microscopic perspective through the introduction of Cooper pairs.
The Hamiltonian (which describes the energy of the system) for BCS theory includes the kinetic energy of the electrons and an attractive interaction term:

$$\mathbf{H}_{BCS} = \sum_{\mathbf{k},\sigma} \epsilon_{\mathbf{k}\sigma} c^{\dagger}_{\mathbf{k}\sigma} c_{\mathbf{k}\sigma} - \sum_{\mathbf{k},\mathbf{k'}} V_{\mathbf{k}\mathbf{k'}} c^{\dagger}_{\mathbf{k}\uparrow} c^{\dagger}_{-\mathbf{k}\downarrow} c_{-\mathbf{k'}\downarrow} c_{\mathbf{k'}\uparrow}, \tag{1.9}$$

where $\epsilon_{\mathbf{k}}$ is the electron energy and $V_{\mathbf{k},\mathbf{k'}}$ is the interaction potential.

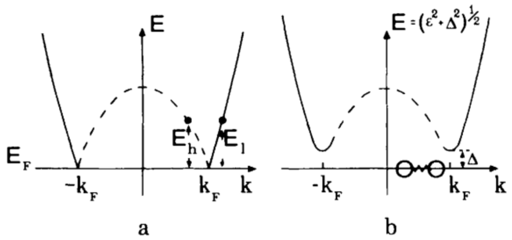

Figure 1.3: Energy momentum diagrams: the dashed line represents the energy levels below the Fermi level. In panel (a) there is the electron-hole pair creation in a normal metal. In panel (b) Cooper pairs in a superconductor [8]

.

The BCS wavefunction describes the ground state of the superconducting electrons as a coherent state of Cooper pairs:

$$|\psi\rangle_{BCS} = \prod_{\mathbf{k}} \left(u_{\mathbf{k}} + v_{\mathbf{k}} e^{i\theta_{\mathbf{k}}} c^{\dagger}_{\mathbf{k}\uparrow} c^{\dagger}_{-\mathbf{k}\downarrow} \right) |0\rangle \,, \tag{1.10}$$

where $u_{\mathbf{k}}$ and $v_{\mathbf{k}}$ are coefficients determined by minimizing the free energy, $c^{\dagger}_{\mathbf{k}\uparrow}$ and $c^{\dagger}_{-\mathbf{k}\downarrow}$ are the creation operators for electrons with momentum $\mathbf{k}$ and spin $\uparrow$ or $\downarrow$. The non-vanishing product of these two coefficients is the amplitude of the Cooper pair $(-\mathbf{k}\downarrow, \mathbf{k}\uparrow)$ [7]:

$$u_{\mathbf{k}} v_{\mathbf{k}} = \frac{1}{2} \frac{\Delta_{\mathbf{k}}}{E_{\mathbf{k}}}, \tag{1.11}$$

$E_{\mathbf{k}}$ is the single particle excitation energy in Figure 1.3,

$$E_{\mathbf{k}} = \sqrt{\xi^2_{\mathbf{k}} + \Delta^2_{\mathbf{k}}}, \tag{1.12}$$

where $\Delta_{\mathbf{k}}$ represents the previously mentioned energy gap.
A look at the excitation spectrum E_k suggests that for excitation energy $k_B T$ lower than the energy gap $\Delta_{\mathbf{k}}$, the system is in its superconductive phase; in

contrast, for excitation k_BT higher than the gap, the superconductor switches to the normal phase. According to this, the energy gap $\Delta_{\mathbf{k}}$ takes the place of an order parameter and it has the temperature dependence (Figure 1.4):

$$\Delta_{\mathbf{k}}(T) \sim 1.74\frac{\pi}{\gamma}k_BT_c\sqrt{1-\frac{T}{T_c}}, \tag{1.13}$$

where $\gamma \approx 1.78$ and T_c are associated with the energy gap through a universal relation [8] in the weak-coupling limit:

$$T_c = \frac{\Delta_{\mathbf{k}}(0)}{1.76k_B}. \tag{1.14}$$

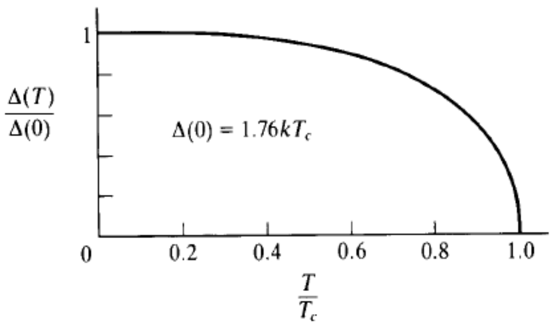

Figure 1.4: Temperature dependence of the energy gap in the BCS theory. Strictly speaking, this curve holds only in a weak-coupling limits but it is a good approximation in most cases [7].

One of the key features of the BCS theory is the energy gap Δ that forms on the Fermi surface. This gap represents the energy required to break a Cooper pair apart and is temperature-dependent. At absolute zero, the energy gap reaches its maximum value and decreases with increasing temperature, disappearing at the critical temperature T_C (Figure 1.3).

1.2 Josephson effect

The Josephson effect is commonly depicted as the flow of a supercurrent through an insulating barrier of the order of 1-2 nanometers separating the two superconductors. Such a device, named as *Josephson junction* (JJ), is represented in Figure 1.5.

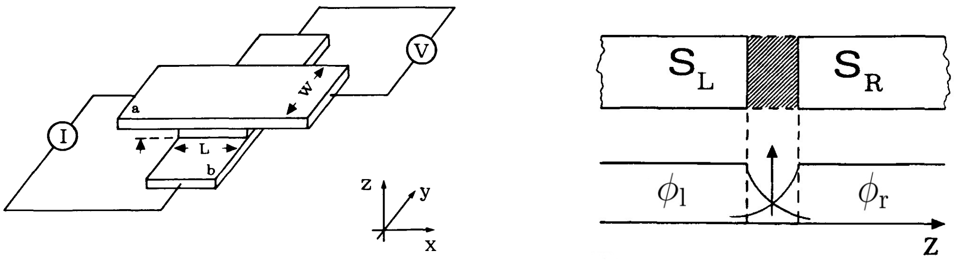

Figure 1.5: **a)** Structure of a Josephson junction, **a** and **b** refer to the two superconductive electrodes. **b)** Order parameters overlap in the insulating barrier between the two electrodes.

The most impressive effect of the Josephson feature is the supercurrent flow through a small barrier between two superconductors without a voltage drop, as experimentally observed for the first time in 1963 [9]. Josephson found that the current flow through the barrier is deeply correlated with the phase difference between the two superconductors. The nature of this phase correlation is truly quantum, the phase difference $\varphi = \phi_L - \phi_R$ between the two superconductors of the junction is a macroscopic variable, regulated by the two Josephson equations:

$$I_s = I_c sin\varphi, \tag{1.15}$$

$$\frac{\partial \varphi}{\partial t} = \frac{e^* V}{\hbar}, \tag{1.16}$$

where e^* equals 2e, V is the voltage drop across the two electrodes, I_s is the supercurrent through the device and I_c is the *critical current*, which is proportional to the carriers tunneling coefficient, and it depends on the geometry, the material and the thickness of the barrier like a decaying exponential function (Figure 1.5)[8]. The first equation indicates that the current flowing without dissipation through the junction is solely determined by the phase difference between the two superconducting electrodes. When there is a time variation in the phase difference between the two electrodes, a voltage develops across the junction. Specifically, the relationship between the phase difference and the applied voltage V is given by the Josephson equation 1.16. Furthermore, this equation is derived purely from the fundamental principles of quantum mechanics and includes only fundamental constants, making it a universal equation [10].

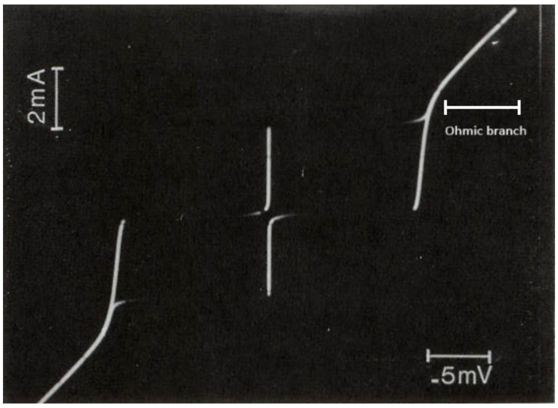

Figure 1.6: Current-Voltage $I(V)$ characteristic at $T = 1.52\ K$ for a conventional $Sn - Sn_xO_y - Sn$ junction [8].

Starting from the superconducting branch ($V = 0$), when the current reaches the critical current value I_c, there is a voltage jump. The finite voltage branch is divided into two parts by the inflection point; the first part at lower voltages is due to quasiparticle tunneling, while in the second part at higher voltages, the electrons reach an excitation level (well beyond the sum of the superconductors' gaps) such that electrons can be considered normal, and the $I - V$ characteristic shows an ohmic branch.

Since there is no voltage drop, no energy is dissipated inside the Josephson junction when it is in the superconducting state. However, energy is stored within the junction [11]. To determine this energy, consider a scenario where the phase changes from φ_1 to φ_2. During this process, an external system that induces the phase change performs the following work on the supercurrent:

$$W_S = \int_{t_1}^{t_2} I_S(t)V(t)dt. \tag{1.17}$$

Upon substituting equations 1.15 and 1.16, it becomes evident that W_S is determined solely by the initial phase φ_1 and the final phase φ_2, instead of the intermediate stages of the process. Specifically, this is expressed as:

$$W_S = \frac{\hbar I_c}{2e} \int_{\varphi_1}^{\varphi_2} \sin\varphi \, \mathrm{d}\varphi = \frac{\hbar I_c}{2e}(\cos\varphi_1 - \cos\varphi_2). \tag{1.18}$$

This leads to the notion of the textitpotential energy of the supercurrent:

$$U_S(\varphi) = E_J(1 - \cos\varphi) + \text{const},, \tag{1.19}$$

$$E_J = \frac{\hbar I_c}{2e}, \tag{1.20}$$

allowing the expression $W_S = U_S(\varphi_2) - U_S(\varphi_1)$; where E_J is identified as the *Josephson energy.*

Due to the energy storage and conservation within the Josephson junction, it can be described by a *nonlinear inductance* L_s. To explicate the properties of this kind of reactance, we examine a general process $\varphi(t)$ with its small variation $\tilde{\varphi}(t)$, such as $\varphi \to \varphi + \tilde{\varphi}$. By substituting this expression into the Josephson equations and performing a Taylor series expansion of $\sin(\varphi + \tilde{\varphi})$ with respect to $\tilde{\varphi}$, the following relation between the voltage and supercurrent is derived:

$$\tilde{I}_S = L_S^{-1}(t) \int \tilde{V}\, dt, \tag{1.21}$$

with L_S^{-1} being the *inductance of the junction.*

$$L_S^{-1} = L_c^{-1} \cos\varphi, \tag{1.22}$$

where L_c is the *characteristic inductance of the junction*:

$$L_c \equiv h/2eI_c, \tag{1.23}$$

In addition to the supercurrent, other phenomena that can be observed include:

- Displacement currents arising from the junction finite capacitance.
- Thermal motion of carriers, which also generates thermal and shot noise, leading to current fluctuations and quasiparticle currents.

When the voltage between the two superconducting electrodes varies over time, a displacement current, which depends on the capacitance C of the junction, flows through the device:

$$I_D = C\frac{dV}{dt}. \tag{1.24}$$

The capacitance can be expressed as the well-known plane-condenser capacitance:

$$C = \frac{\epsilon_r \epsilon_0 A}{t}, \tag{1.25}$$

where ϵ_r is the relative permittivity, ϵ_0 is the vacuum permittivity, A is the area, and t is the thickness of the barrier. The specific capacitance of the junction, C/A, is a slower decaying function of t than the critical current density $J_c = I_c/A$, which is exponential in thickness (Figure 1.5 b). Thus, the specific capacitance is nearly constant across a wide range of critical current densities and is approximately of the order of $\mu F/cm^2$ for conventional junctions [8].
When the temperature $T > 0$, thermal motion breaks Cooper pairs into single-electron excitations called quasiparticles, which differ from normal electrons in metals due to their dependence on the superconducting energy gap. At zero voltage ($V = 0$), quasiparticles cannot tunnel across the junction because the energy required to overcome the total superconducting gap $\Delta_L + \Delta_R$ is not supplied. However, near the critical temperature T_c (or slightly below it), the thermal energy $2k_BT$ becomes comparable to or larger than $\Delta_L + \Delta_R$. This allows quasiparticles to dominate the current, leading to an Ohmic response described by:

$$I_N(V) = \frac{V}{R_N}. \tag{1.26}$$

In the presence of normal resistance R_N, the normal current $I_N(V)$ flows through the junction. This ohmic regime, attributed to quasiparticles, is observed for $V > (\Delta_L + \Delta_R)/e$ at all temperatures. While the normal current can exhibit high non-linearities as a function of V, these are typically attributed to the normal resistance. The interplay of normal current and supercurrent suggests the existence of a finite relaxation time in these systems. We define the *characteristic voltage of the junction* V_c as:

$$V_c \equiv I_c R_N, \tag{1.27}$$

and by recalling the previous definition of L_c we can define the *Josephson oscillation frequency* [7]:

$$\omega_c = V_c \frac{e^*}{\hbar} = \frac{R_N}{L_c}. \tag{1.28}$$

This parameter is crucial in practical applications, such as microwave devices based on the Josephson effect, which are important in superconducting circuits. In conventional Josephson junctions, ω_c is of the order of several terahertz, resulting in the fastest pulse-rise times being in the range of a few picoseconds [12]. The normal current is a dissipative term that generates *thermal noise*, significant in the low voltage range and for thermal energy greater than $\hbar\omega_c$, and *shot noise*, which is dominant in the high voltage range [8].

1.2.1 Phase electrodynamic

Commonly, the dynamics of a Josephson junction are explained using an equivalent electrical circuit model in which the junction is placed in parallel with a resistor and a capacitor (Figure 1.7). This model is known as the *Resistively and Capacitively Shunted Junction (RCSJ)* model. The RCSJ model is able to interpret most of the I-V characteristics of the junction [8] [11].

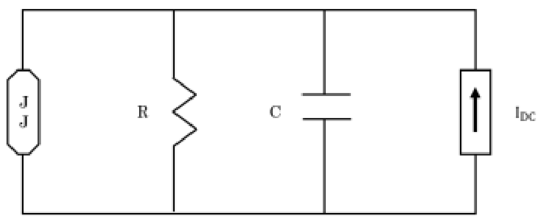

Figure 1.7: Equivalent circuit of a current-biased Josephson junction according to the RCSJ model..

The junction is biased with a high impedance current source. This setup allows us to directly observe a zero voltage state and the critical current in the current-voltage characteristics. Using *Kirchoff's second circuit law* we find:

$$I_{DC} = I_c sin\varphi + I_N(V) + C\frac{dV(t)}{dt}, \tag{1.29}$$

with I_{DC} polarization current; using equation 1.16 and considering the magnetic flux quantum $\Phi_0 = \frac{h}{e^*}$ we obtain:

$$I_{DC} = \frac{\Phi_0}{2\pi R_N}\frac{d\varphi}{dt} + \frac{\Phi_0 C}{2\pi}\frac{d^2\varphi}{dt^2} + I_c \sin\varphi, \tag{1.30}$$

that is, an equation of motion for the phase difference between the superconductors. This equation can be rewritten in terms of a potential U_j:

$$I_{DC} - I_c \sin\varphi = \frac{2\pi}{\Phi_0}\frac{\partial U_J}{\partial \varphi} \Rightarrow U_J = \frac{\Phi_0}{2\pi}[I_c(1-\cos\varphi) - I_{DC}\varphi], \tag{1.31}$$

U_J is also known as *washboard potential*, and its dependence on the phase is shown in Figure 1.8. The dynamics of a Josephson junction can be compared to a particle in a tilted washboard potential, which dictates the behavior of this system. The potential impacts the phase difference φ, analogous to the position of the particle. At low bias currents, the phase particle oscillates near the minima of the potential, indicative of the superconducting state without voltage. As the bias current rises, the potential's tilt increases. When I_{DC} exceeds I_c, the particle escapes the potential minima and "rolls" down the washboard, resulting in a non-zero voltage across the junction, marking the resistive state. This is similar to a particle in a tilted periodic potential experiencing damping, where damping symbolizes the junction's dissipative processes.

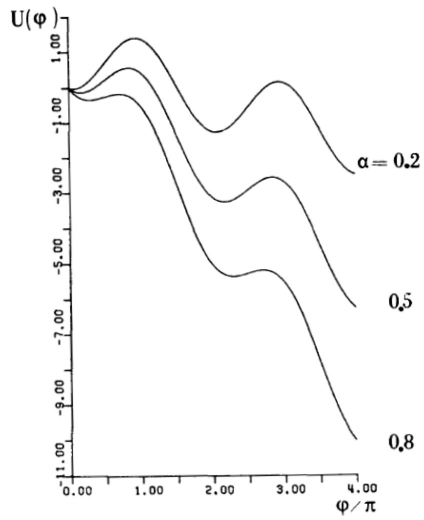

Figure 1.8: Washboard potential for different values of bias current $\alpha = \frac{I}{I_c}$; the applied current determines the tilt of the potential.

Damping plays a significant role in determining the dynamic behavior of a Josephson junction, particularly its current-voltage characteristics and phase dynamics. In the RCSJ model, to characterize the capacitance effect for a Josephson junction, and quantify the damping, we introduce the dimensionless *Stewart-McCumber* parameter:

$$\beta \equiv (\omega_p R_0 C)^2 = \frac{2eI_cR^2C}{\hbar}. \tag{1.32}$$

with ω_p being the *plasma frequency*:

$$\omega_p = \frac{1}{\sqrt{L_c C}}, \tag{1.33}$$

ω_p is the oscillation frequency of particles at the well's minimum in the superconducting state.
An additional significant parameter frequently associated with the Stewart-McCumber parameter is the damping factor Q^{-1}, given by:

$$Q^{-1} = \frac{1}{\sqrt{\beta}}, \tag{1.34}$$

where Q represents the quality factor of an oscillator. The value of β_c differentiates between two distinct dynamical regimes: **underdamped** ($\beta_c > 1$) and **overdamped** ($\beta_c < 1$). These regimes manifest through different behaviors in the phase dynamics of the junction.

In the overdamped regime ($\beta_c < 1$): Within this regime, the resistive component primarily influences the dynamics of the junction, rapidly dispersing energy and preventing the phase particle from accumulating sufficient momentum to traverse multiple wells. Consequently, the retrapping current I_r nearly matches the switching current I_{sw}, resulting in non-hysteretic I-V characteristics. The junction transitions smoothly and reversibly between superconducting and resistive states, with negligible energy stored in the capacitance, thereby avoiding oscillations and eliminating hysteresis in the (I-V) curve (Figure 1.9).

In the underdamped regime ($\beta_c > 1$): the phase particle exhibits a characteristic roll-down motion in the tilted washboard potential. When the current exceeds the switching current I_{sw}, the phase particle gains enough energy to escape from its potential well, causing the junction transition from the superconducting to the resistive state. As the current is reduced, the particle does not immediately return to the initial well but instead continues to move "downhill" in the potential landscape due to inertia, preventing the junction from reentering the superconducting state. Only when the current is reduced to the retrapping current I_r, which is significantly lower than I_{sw}, the phase particle loses enough energy to be retrapped in a potential minimum [7]. This behavior results in hysteresis in the current-voltage (I-V) characteristics of the junction (Figure 1.10). In this regime, the RCSJ model becomes less accurate due to the prominence of non-linear and inertial effects, requiring more sophisticated models for precise descriptions [10].

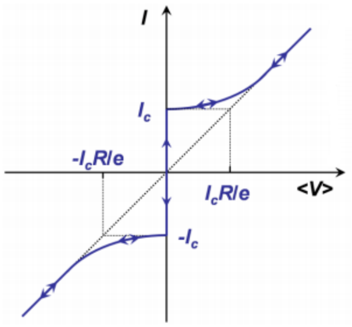

Figure 1.9: Absence of hysteresis in a overdamped junction.

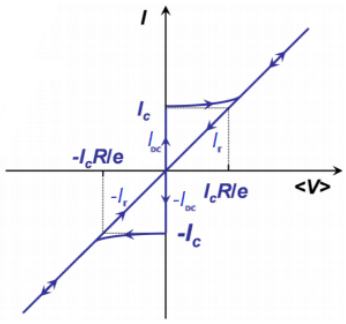

Figure 1.10: Hysteresis of an underdumped juction.

TJM Model: The *Tunneling Junction Model* (TJM) serves as an essential framework for investigating superconducting circuits. Building upon the classical RCSJ model, the TJM incorporates thermal noise effects, leading to a more accurate portrayal of the dynamics in Josephson junctions. Due to the arbitrary character of the corrections it is considered a model rather than an exact theory. This model enhances the classical approach by substituting the simple sinusoidal current-phase relationship and the external parallel resistance in equation 1.30 with a more elaborate expression grounded in microscopic theory. The resulting equation to be addressed is:

$$I = \frac{\hbar}{2e} C \frac{\partial^2 \varphi}{\partial t^2} + I(\varphi), \tag{1.35}$$

where $I(\varphi)$ is specified by microscopic theory. Under the adiabatic approximation, where the voltage $V(t)$ is both small and changes slowly relative to the gap frequency $2\Delta/\hbar$, the equation simplifies to:

$$I = \frac{\hbar}{2e} C \frac{\partial^2 \varphi}{\partial t^2} + I_{qp}(V(t)) + I_{J2}(V(t)) \cos \varphi(t) + I_{J1}(V(t)) \sin \varphi(t), \tag{1.36}$$

where:

- $I_{qp}(V(t))$ is the quasiparticle current, which represents dissipative transport due to the tunneling of quasiparticles;
- $I_{J1}(V(t))$ is the first Josephson current component, which is proportional to $\sin\varphi(t)$. It represents the main supercurrent contribution responsible for the Josephson effect;
- $I_{J2}(V(t))$ is the second Josephson current component, proportional to $\cos\varphi(t)$, which arises from higher-order corrections to the current-phase relationship. It accounts for additional effects related to the junction's microscopic properties [13].

Compared to the RCSJ model, the TJM encompasses more complex phenomena, offering a superior characterization of subgap leakage currents. One of the notable features of the model is the *supercurrent suppression parameter* α, which allows the critical current to be modified to reflect the observed behavior in experiments. This parameter typically lies in the range $0.3 \leq \alpha \leq 0.9$, effectively reducing the classical critical current to match experimental setups [14]. Additionally, singularities in the energy gap can be smoothed using phenomenological rules. A common approach is to apply the *Lorentzian smoothing technique*, which modifies the behavior of the singularities as follows:

$$\ln|X| \to \ln\left(X^2+\delta^2\right)^{1/2}, \tag{1.37}$$

$$\mathrm{sign}(X) \to \frac{2}{\pi}\arctan\left(\frac{X}{\delta}\right), \tag{1.38}$$

where δ is a dimensionless phenomenological parameter describing the smearing of the energy gap edges. The smoothing eliminates discrepancies in the imaginary part of $I_{p,q}$ at low frequencies. In some cases, *Gaussian smoothing* may be applied. The time-domain formulation of the TJM is particularly useful for analyzing fluctuation sources in the junction [10]. The time-domain expressions for the supercurrent and normal current are given by:

$$I_S(t) = \int_{-\infty}^{t} dt' I_p(t-t')\sin\left(\frac{1}{2}[\phi(t)+\phi(t')]\right), \tag{1.39}$$

$$I_N(t) = \int_{-\infty}^{t} dt' I_q(t-t')\sin\left(\frac{1}{2}[\phi(t)-\phi(t')]\right), \tag{1.40}$$

where $\varphi(t)$ is the phase difference across the junction, and the kernels $I_p(\tau)$ and $I_q(\tau)$ are related to the tunnel current amplitudes $I_{p,q}(\omega)$ by a Fourier transform. For temperatures much lower than the critical temperature $T \ll T_c$, the kernels simplify to:

$$I_p(\tau) = \frac{2\pi\Delta(0)}{ehR_N} J_0(\tau/\tau_g)Y_0(\tau/\tau_g), \tag{1.41}$$

$$I_q(\tau) = \frac{2\pi\Delta(0)}{ehR_N} J_1(\tau/\tau_g)Y_1(\tau/\tau_g) - \frac{\hbar}{eR_N}\delta'(\tau), \tag{1.42}$$

where J_0, J_1 and Y_0, Y_1 are Bessel functions of the first and second kind, respectively, and τ_g is related to the energy gap as $\tau_g = 2\omega_g^{-1} = \hbar/\Delta(0)$. These kernels oscillate with the gap frequency ω_g and decrease as τ^{-1}. The slow degeneration linked to the infinite memory of the system leads to computational challenges. To address this, kernels are often modified by incorporating an exponential decay term $\exp(-\tau/\tau_s)$, where (τ_s) is known as a *smearing time* determined from the previously used energy gap smearing. This modification helps to reduce computational load, thus making the TJM more feasible for practical calculations. Nonetheless, the complete microscopic TJM model remains more computationally complex compared to the simpler RSJ and RSJN models. It does, however, provide a more accurate representation of junction dynamics when capacitance and quantum effects are pronounced. Another key benefit of the TJM is its ability to estimate the *subgap resistance* (R_{sub}), a vital parameter for defining junctions properties for qubits. In qubit applications, achieving low dissipation is crucial for coherence, as dissipation sources such as subgap leakage currents can significantly hinder qubit performance [15]. The TJM model becomes particularly useful as a metric for evaluating subgap resistance, with high subgap resistances suggesting minimal dissipative quasiparticle activity. This low density of quasiparticles implies that the states below the superconducting gap remain unpopulated by quasiparticles, which is beneficial because a rise in quasiparticles—akin to two-level system (TLS) noise—adversely affects qubit coherence [16]. Hence, a high R_{sub} indicates reduced dissipation and enhanced coherence, crucial for qubit fidelity in quantum applications.

Thermal fluctuations: Moreover, it is crucial to account for the fact that at non-zero temperatures, thermal fluctuations significantly impact the behavior of the phase particle in Josephson junctions. Even if the current applied is beneath the critical current I_C, thermal activation can cause the phase particle to escape from its potential well. This escape process is stochastic, meaning that the exact timing and occurrence of these events are governed by chance, influenced by the temperature of the system and the height of the potential barrier. The higher the temperature, the more likely it is for thermal energy to push the phase particle over the barrier, and this rate of escape increases accordingly. This phenomenon of thermal escape is well described by Kramers' theory for thermal activation, where the escape rate is given as an exponential function of the ratio between the barrier height and the thermal energy [17]. Mathematically, this escape rate Γ_{TA} is proportional to $exp(-U/k_BT)$, where U is the potential barrier that represents the energy difference between the bottom of a potential well and the peak of the barrier separating it from an adjacent state, k_B is Boltzmann's constant, and T is the temperature. This dependence highlights the exponential sensitivity of the escape process to temperature [18]. However, at very low temperatures, thermal activation becomes negligible. The energy available from thermal fluctuations is no longer sufficient to allow the phase particle to cross the potential barrier. Instead, quantum tunneling through the barrier becomes the dominant escape mechanism; it should be noted that this only applies to underdamped junctions at very low temperatures. This phenomenon is referred to as macroscopic quantum tunneling (**MQT**). In MQT, the phase particle "tunnels" through the potential barrier because of quantum mechanical effects, without having to possess the energy to overcome it thermally. MQT is a quintessential quantum phenomenon. Although quantum tunneling is a common process at microscopic scales (such as in atomic systems), MQT involves the tunneling of a macroscopic quantity, the phase variable in a Josephson junction. The observation of MQT in Josephson junctions has provided strong evidence for the quantum nature of macroscopic variables, illustrating that quantum mechanics can govern large-scale systems under appropriate conditions [19]. The rate of MQT is determined by the characteristics of the junction, such as the height and shape of the potential barrier, and is described by a quantum mechanical extension of Kramers' theory. In superconducting circuits, like the ones used in quantum computing that employ phase cubits, the management and manipulation of MQT are essential. Macroscopic quantum tunneling (MQT) in Josephson junctions arises when the phase difference p behaves as a quantum variable, allowing tunneling through the potential barrier in the washboard potential at low temperatures. Unlike thermal activation, where a particle escapes over the barrier due to thermal energy, MQT occurs through quantum tunneling, becoming dominant as the temperature decreases. This behavior is typically analyzed using the WKB approximation and experimentally observed via the escape rate, which deviates from classical thermal predictions [18, 20, 21].

1.2.2 Josephson effect in magnetic field

Here, we describe the behavior of a Josephson junction in a magnetic field (Figure 1.11).

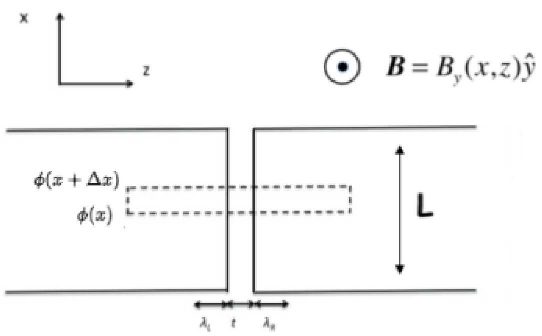

Figure 1.11: Geometric Configuration of the Junction.

When an external magnetic field B is applied orthogonally to the transport direction, it causes interference of the Cooper pair wave functions, which alters the transport properties of the junction. This phenomenon leads to a spatial variation of the critical current density along the junction barrier, resulting in a specific magnetic dependence of I_C.

The fundamental equation connecting the phase, electric current, and magnetic field is expressed as: ,

$$\nabla\varphi = \frac{2e}{\hbar}\left(\frac{m\mathbf{J}}{2e^2\rho} + \mathbf{A}\right), \tag{1.43}$$

where ρ denotes the Cooper pair density and $\mathbf{A}$ represents the vector potential. The influence of the bulk super-currents J can be ignored as they are either orthogonal to the integration boundary (as shown in Figure 1.11) or negligibly small within the interior of the superconductors. A magnetic field $B = B_y(x, z)$ is applied to the junction, permeating the electrodes to the extent of the London penetration depths λ_L and λ_R (with L and R denoting the left and right regions, respectively). Calculating the gauge-invariant phase difference between two points along the barrier, with coordinates x and $x + dx$, reveals the impact of the externally applied magnetic field:

$$\varphi(x + \Delta x) - \varphi(x) = \frac{2e}{\hbar}\oint \mathbf{A}\cdot d\mathbf{l}, \tag{1.44}$$

using Stokes' theorem in the limit $\Delta x \to 0$, we obtain:

$$\frac{\partial\varphi}{\partial x} = \frac{2\pi B_y d}{\Phi_0}, \tag{1.45}$$

with B_y being the local magnetic induction, and $d = t + \lambda_L + \lambda_R$. Integrating this last equation yields:

$$\varphi = \frac{2eB}{yd}x + \varphi_0. \tag{1.46}$$

The Josephson equation then becomes:

$$J_s = J_c sin\left(\frac{2eB}{yd}x + \varphi_0\right), \tag{1.47}$$

if we integrate over the junction width the supercurrent (assuming a rectangular junction) we have a Fraunhofer pattern as illustrated in Figure 1.12:

$$I_s(\Phi) = J_s W L\left|\frac{sin\left(\pi\frac{\Phi}{\Phi_0}\right)}{\pi\frac{\Phi}{\Phi_0}}\right|, \tag{1.48}$$

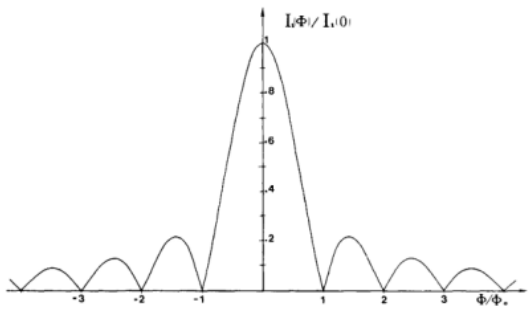

Figure 1.12: Critical current vs Flux through a rectangular junction.

while for a circular junction [8], we obtain an Airy pattern:

$$I_s(k) = \pi R^2 J_s \left| \frac{J_1(kR)}{\frac{1}{2}(kR)} \right|, \tag{1.49}$$

where $k = \frac{2\pi d}{\Phi_0}$ and J_1 are the *Bessel funcion*, as shown in Figure 1.13:

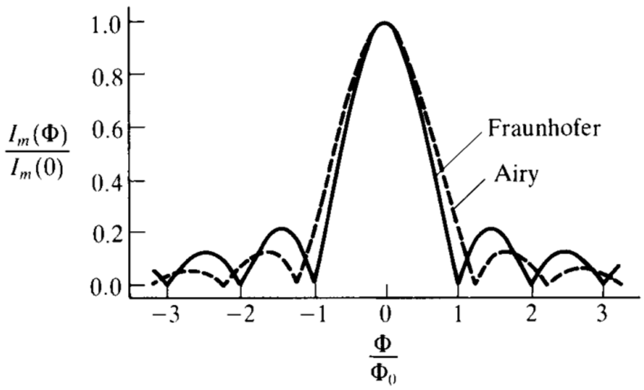

Figure 1.13: In contrast to the pattern of a rectangular junction, the circular one shows that the first minimum is anticipated at stronger fields.

These are examples of cases where the current can be calculated analytically assuming a uniform J_C throughout. However, in experimental scenarios, various factors can influence this value. The shape of the junction, the characteristics of the electrodes or the barrier, and even their potential irregularities contribute to unique phase variations across the barrier. This results in Meissner screening, magnetic interference effects, the creation and trapping of vortices (normal regions within the superconductor), shielding, and spontaneous super-currents [22]. All these phenomena can alter the shape and the amplitude of the magnetic dependence of the critical current.

1.3 Superconducting quantum circuit: the transmon

In the previous sections, we have discussed the fundamental concepts of the Josephson effect and the physics of Josephson junctions. These principles allow us to manipulate and measure the macroscopic quantum phase difference between two superconducting electrodes. This unique feature can be used to transfer the laws of quantum mechanics, typically applied to microscopic entities, onto a circuit. This capability is particularly valuable in the study and use of superconducting qubits, which are increasingly being investigated due to their advantageous fabrication and their simpler manipulation compared to qubits based on atoms or ions [23]. Superconducting qubits, acting as artificial atoms, have configurable energy-level spectra determined by circuit element parameters. This parameter space allows predictable performance in terms of transition frequencies, anharmonicity, and complexity. The theory for the quantized Josephson junction is defined by assuming that the phase difference φ and the charge Q are operators that satisfy the commutation relation [24]:

$$[\hat{\varphi}, \hat{Q}] = i. \tag{1.50}$$

The mechanical analogue of the tilted washboard potential thus turns into an analogue of a quantum-mechanical description of a particle in a periodic potential, following the correspondence described in Table 1.1. Therefore, in the absence of

Particle	**Josephson Junction**
$\left(H = \frac{p^2}{2m} - U\cos\left(\frac{x}{a}\right) - Fx\right)$	$\left(H = \frac{(Q-Q_g)^2}{2C} - E_J\cos(\varphi) - \frac{\hbar}{2e}I_b\varphi\right)$
Coordinate (x)	Phase (φ)
Momentum $\left(p = -\frac{\hbar}{i}\partial_x\right)$	$\propto$ charge $\left(\frac{\hbar Q}{2e} = -2ei\partial_\varphi\right)$
Velocity $\left(v = \frac{dx}{dt} = \frac{p}{m}\right)$	$\propto$ voltage $\left(\frac{2eV}{\hbar} = \frac{\partial\varphi}{\partial t} = \left(\frac{2e}{\hbar}\right)^2 \frac{1}{C}\frac{\hbar Q}{2e}\right)$
Mass (m)	$\propto$ capacitance $\left(\left(\frac{2e}{\hbar}\right)^2 C\right)$
Force (F)	$\propto$ bias current $\left(\frac{\hbar}{2e}I_b\right)$

Table 1.1: Analogy between the quantities of the quantum theory of a particle in a periodic potential and the quantum theory of a Josephson junction [25].

dissipation, the behavior of a Josephson junction can be described by a Hamiltonian H, which is a function of the phase difference φ and the charge Q transferred between the electrodes:

$$H = \frac{(Q - Q_g)^2}{2C} - E_J\cos(\varphi) - \frac{\hbar}{2e}I_b\varphi, \tag{1.51}$$

where I_b is the bias current and Q_g is the gate charge. As already introduced, the state of the junction is characterized by a macroscopic wave function Ψ. In the time-independent case, it satisfies the Schrödinger equation:

$$4E_C(-i\partial_\varphi - Q_g/e)^2\Psi_n - E_J\cos(\varphi)\Psi_n = E_n\Psi_n. \tag{1.52}$$

This is called the Mathieu differential equation, its eigenfunctions Ψ_n are Mathieu functions, and E_C is the charging energy. Depending on the ratio E_J/E_C, we can distinguish two different regimes: phase regime and charge regime. For $E_J \gg E_C$, the Josephson junction operates in the phase regime or 'tight-binding limit'. In this regime, φ is well defined and Q has large quantum fluctuations. For $E_J \ll E_C$, the Josephson junction operates in the charge regime or 'nearly free-electron limit'. It occurs when there are few Cooper pairs: n is well defined, and φ has large quantum fluctuations; therefore, the charging nature of the capacitor is dominating. In this situation, the junction is known as a Cooper-pair box (CPB) [26]. By considering $E_L = \varphi_0^2/L$, the inductive energy due to an inductance L shunting the junction, there are three relevant energies which identify the operation of a qubit, and we can distinguish three basic designs for superconducting qubits: charge qubit, flux qubit, and phase qubit. The circuit engineering and subsequent qubit type differentiation occurs by modification of the energy scales identified by the ratios $E_L/(E_J - E_L)$ and E_J/E_C. In Table 1.2, some configurations are reported: when the ratio ($E_J \leq E_C$) holds, the qubit becomes

Configuration	**Ratio** ($E_L/(E_J - E_L)$)	**Ratio** (E_J/E_C)
Cooper-pair box	(0)	($\ll 1$)
Quantronium	(0)	(~ 1)
Fluxonium	($\ll 1$)	(~ 1)
Transmon	(0)	($\gg 1$)
Phase qubit	(~ 1)	($\gg 1$)
Flux qubit	($\gg 1$)	($\gg 1$)

Table 1.2: Different configurations corresponding to the chosen ratios.

highly sensitive to charge noise, which is more challenging to mitigate than flux noise. Achieving high coherence under these conditions is very difficult. Moreover, current technologies offer greater flexibility in engineering the inductive (or potential) part of the Hamiltonian. Consequently, working within the ($E_J \leq E_C$) limit enhances the system's sensitivity to changes in the potential Hamiltonian [26]. This discussion will focus on the state-of-the-art superconducting qubits that fall into the regime where ($E_J \gg E_C$). One common approach is to shunt the junction with a large capacitor ($C_B \gg C_J$), effectively reducing the qubit's sensitivity to charge noise. This circuit is commonly known as the transmon qubit (transmission-line shunted plasma oscillation qubit), a modification of the CPB [26].

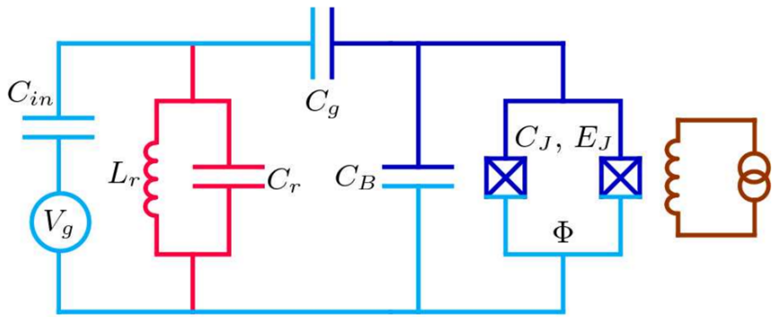

Figure 1.14: Circuit diagram of a transmon qubit, showing a Josephsonjunction (providing nonlinearity via the Josephson energy E_J) shunted by a large capacitance (reducing charge noise by increasing the total capacitance C, thus lowering the charging energy $E_C = e^2/2C$). The transmon operates in the $EJ > Ec$ regime, where it is less sensitive to charge noise, achieving enhanced coherence properties.

By increasing the ratio E_J/E_C, the transmon mitigates charge noise fluctuations, improving coherence times without sacrificing qubit anharmonicity [27].

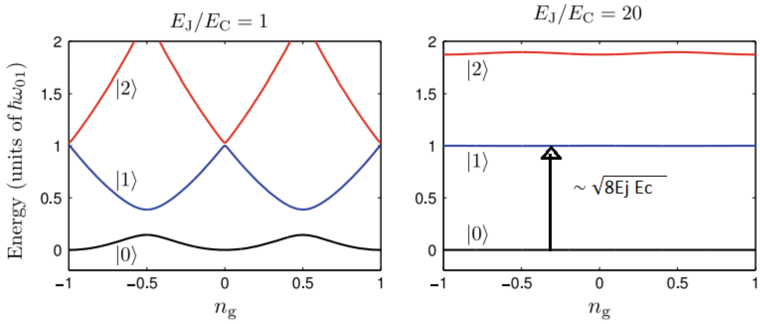

Figure 1.15: Eigenenergies E_m (first three levels, $m = 0, 1, 2$) of the qubit Hamiltonian are shown as a function of the effective offset charge n_g for various ratios of E_J/E_C. Energies are scaled by the transition energy E_{01} between levels 0 and 1. [27]

The typical E_J/E_C ratio in a transmon is on the order of 100, which exponentially reduces the qubit's sensitivity to charge noise [28]. In this regime, the transmon exhibits near-exponential suppression of charge dispersion, enhancing coherence times. By balancing the anharmonicity and minimizing charge noise, the transmon qubit provides a robust platform for quantum information processing. The charge noise sensitivity decays exponentially with $\sqrt{E_J/E_C}$, while the anharmonicity follows a power-law decay. A typical transmon has a ratio of $E_J/E_C \sim 100$, with operating frequencies in the range of a few GHz to 10 GHz, and anharmonicities between 100 MHz and 300 MHz [26]. In this parameter range, the low-energy eigenstates are largely localized within the potential well. To gain insight into the behavior, we can expand the potential term $E_J \cos(\varphi)$ into a power series for small φ values as follows:

$$E_J \cos(\varphi) \approx E_J \left(1 - \frac{\varphi^2}{2} + O(\varphi^4)\right). \tag{1.53}$$

The leading quadratic term results in a quantum harmonic oscillator (QHO), but the quartic term introduces a deviation from purely harmonic energy levels. This alteration is responsible for the anharmonicity in the energy spectrum of the two level system.
To enable qubit frequency control and perform gate operations, additional degrees of freedom are necessary to adjust the resonance between qubits [29]. A practical method to achieve tunability is by replacing the single Josephson junction with a DC-SQUID, consisting of two identical junctions in a loop. Interference between the SQUID's two arms allows for adjustment of the effective critical current by applying an external flux, subject to the quantization condition:

$$\varphi_1 - \varphi_2 + 2\varphi_e = 2\pi k, \tag{1.54}$$

where $\varphi_e = \pi\Phi_{\text{ext}}/\Phi_0$. Under this condition, the SQUID can be treated as a single effective Josephson junction with a Josephson energy E_J^{eff} that depends on the applied flux. The effective Josephson energy of the split transmon can be adjusted by manipulating the external flux. Consequently, the Hamiltonian of the system

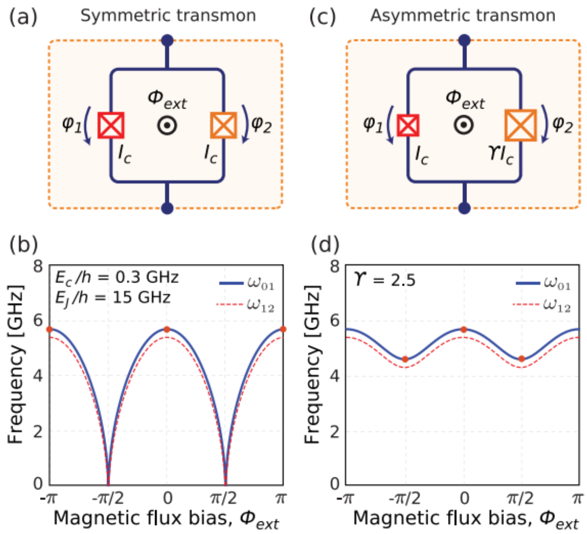

Figure 1.16: The modular qubit circuit representation for a capacitively shunted transmon qubit is shown, along with the corresponding transition frequencies between the two lowest energy states as a function of the applied magnetic flux. Panels (a) and (b) show the symmetric transmon qubit, where the energy is determined by E_J and a shunting capacitor providing the charging energy E_C. Panels (c) and (d) display the asymmetric transmon, where the junction asymmetry is defined by $E_{J2}/E_{J1} = 2.5$ [26].

contains a component that is influenced by the cosine function of the external flux:

$$H = 2E_{J1}\cos(\varphi_{\text{ext}}). \tag{1.55}$$

Thus, the qubit frequency becomes periodically tunable with the external flux. However, split transmons exhibit sensitivity to random fluctuations in the flux (i.e., flux noise). The slope of the qubit's spectrum reveals how strongly flux noise influences the qubit frequency. Sensitivity to flux noise is minimized only at multiples of the flux quantum ($\Phi_{\text{ext}} = k\Phi_0$ where $k \in \mathbb{Z}$), as shown in Figure 1.16. Recent developments aim to reduce flux noise sensitivity while preserving the tunability. Asymmetric split transmons achieve this by varying the junction areas within the SQUID, resulting in a reduced tuning range that compensates for fabrication without sacrificing coherence. The Hamiltonian of the system is:

$$E_J^{\text{eff}} = E_{J1} + E_{J2} - 2E_{J1}\cos(\varphi_{\text{ext}}). \tag{1.56}$$

Here, E_{J1} and E_{J2} represent the Josephson energies of the two junctions, and $d = (1 - \alpha + 1)$ is the asymmetry parameter with $\alpha = E_{J2}/E_{J1}$. The tunability of the qubit frequency, achieved via a DC-SQUID threaded with magnetic flux, enables faster gate operations. However, this method introduces sensitivity to flux noise, resulting in dephasing times of approximately tens of microseconds [29]. Additionally, the milliampere-level currents required to control the DC and RF lines, which are inductively coupled to the SQUID, allow for flux tunability but also lead to crosstalk between qubits and potential heating issues, thereby limiting scalability [30]. These issues are particularly evident in multi-qubit systems, where noise and thermal effects compromise the fidelity and coherence times of qubits. This thesis proposes a new superconducting hybrid circuit designed to overcome the specific limitations of the split transmon. As detailed in the following chapters, this novel approach integrates a ferromagnetic layer on top of a conventional tunnel junction creating a SIsFS hybrind Josephson junction.

Chapter 2

Ferromagnetic Josephson Junctions

This chapter will explore the principles and functionalities of magnetic Josephson junctions (MJJs). Since this thesis is devoted to the optimization of ferromagnetic materials for their integration as a barrier in MJJs, we will first provide an overview on ferromagnetism and ferromagnetic materials. Then, considering the metallic nature of standard ferromagnetic barrier, we introduce the proximity effect as the key mechanism governing the transport at the Superconductor (S) / Ferromagnet (F) interface. At the end, we analyze the unique characteristics of magnetic Josephson junctions (MJJs), focusing on both their transport properties and magnetic response to an applied field, with particular emphasis on SIsFS junctions. As discussed at the end of the chapter, these SIsFS junctions can combine the memory properties of standard SFS junctions with the tunneling behavior of SIS junctions, thus providing advanced functionalities both for superconducting digital and quantum electronics.

2.1 Notes on ferromagnetism

Ferromagnetism is a fundamental example of spontaneous broken symmetry in condensed matter physics, where certain materials exhibit spontaneous magnetization below a critical temperature, known as the Curie temperature T_{Curie}. This spontaneous magnetization arises due to the alignment of atomic magnetic moments within the material, resulting in a net magnetic moment even in the absence of an external magnetic field. The magnetization M thus acts as the order parameter in ferromagnetic systems, characterizing the second-order transition from a disordered (paramagnetic) phase at $T > T_{Curie}$ to an ordered (ferromagnetic) phase [31]. The behavior of ferromagnetic materials near the Curie temperature can be described using the same methodology applied to the second-order transition in superconductors. For a second-order phase transition, the free energy F can be expanded in terms of the order parameter M as:

$$F(M) = F_0 + a(T - T_{Curie})M^2 + bM^4 + \cdots \,, \tag{2.1}$$

where F_0 is the free energy of the disordered phase, a and b are positive constants, and T is the temperature. The term $a(T-T_{Curie})$ ensures that the coefficient of M^2

changes sign at $T = T_{Curie}$, signaling the onset of the phase transition. Minimizing the free energy with respect to M yields the equilibrium magnetization:

$$M(T) = \begin{cases} \sqrt{\frac{a(T_{Curie}-T)}{b}} & \text{for } T < T_{Curie}, \\ 0 & \text{for } T \geq T_{Curie}. \end{cases} \tag{2.2}$$

This equation shows that the magnetization decreases continuously to zero as the temperature approaches T_{Curie} from below, a hallmark of second-order phase transitions [32].
A ferromagnet at a temperature below its Curie temperature thus shows spontaneous magnetization. However, the magnetization is not necessarily homogeneous. Ferromagnetic materials spontaneously divide into regions called domains, where atomic magnetic moments align uniformly. This configuration minimizes the total energy of the system. For a ferromagnet, the following terms has to be considered.

- **Exchange Energy:** The exchange energy is a fundamental aspect of ferromagnetic materials and arises from the quantum mechanical interaction between the spins of adjacent electrons. This interaction, described by the Heisenberg exchange model, favors parallel alignment of neighboring spins. The exchange energy can be expressed mathematically as:

$$E_{\text{exchange}} = -J \sum_{\langle i,j \rangle} \mathbf{S}_i \cdot \mathbf{S}_j, \tag{2.3}$$

  where J is the exchange constant, and S_i and S_j represent the spins of electrons at neighboring atomic sites. When $J > 0$, the parallel alignment of spins is energetically favorable, which is the hallmark of ferromagnetic ordering [33]. The exchange interaction originates from the Pauli exclusion principle and Coulomb repulsion between electrons. Electrons with parallel spins avoid spatial overlap, thereby reducing Coulomb repulsion, which stabilizes the system. This quantum mechanical phenomenon is what causes the long-range spin alignment characteristic of ferromagnetism, which typically spans distances from micrometers to millimeters [33]. Although the exchange interaction primarily influences adjacent spins (on a scale of a few ångströms), its impact extends over significantly larger distances, resulting in coherent spin alignment across magnetic domains. In ferromagnetic materials, the strength of the exchange interaction determines the Curie temperature (T_{Curie}), above which thermal agitation disrupts the alignment of spins, leading to a transition to the paramagnetic state. Materials like iron, cobalt, and nickel have high exchange constants, resulting in significant Curie temperatures, making them strong ferromagnets [31].

- **Magnetocrystalline Anisotropy energy** The magnetocrystalline anisotropy energy (E_a) relates the direction of magnetization with the orientation of the lattice. When an external magnetic field attempts to align the electron spins, the electron orbit also tends to align. However, since the electron orbit is strongly coupled to the lattice, it resists any attempt to rotate the spin axis. Therefore, the magnetocrystalline anisotropy energy represents the energy needed to overcome the spin-orbit coupling. It is thus the energy scale that distinguishes soft ferromagnetic materials from hard ones. For cubic crystals, such as iron Fe and nickel Ni, the anisotropy energy E_a can be written as:

$$E_a = K_1(\alpha_1^2\alpha_2^2 + \alpha_2^2\alpha_3^2 + \alpha_3^2\alpha_1^2) + K_2(\alpha_1^2\alpha_2^2\alpha_3^2) + \cdots , \tag{2.4}$$

whre, K_1 and K_2 denote the magnetocrystalline anisotropy constants, while α_1, α_2, and α_3 represent the direction cosines of the magnetization vector relative to the crystal axes $\langle 100 \rangle$, $\langle 110 \rangle$, $\langle 111 \rangle$, respectively. The constant K_1 is critically significant as it quantifies the anisotropy's intensity. Figure 2.1 presents the magnetization response to an external magnetic field, applied along various crystal axes. This behavior is affected by the magnetocrystalline anisotropy of iron, which determines its favored magnetization orientations within the crystal. For iron, the Figure 2.1 shows that the magnetization process can be achieved with relatively low fields, usually in the range of a few tens of oersteds, along the $\langle 100 \rangle$ direction, which is therefore known as the "easy direction" of magnetization. In contrast, significantly higher fields, typically on the order of several hundred oersteds, are necessary to saturate iron along the $\langle 110 \rangle$ direction, which is thus called the "hard axis" of magnetization.

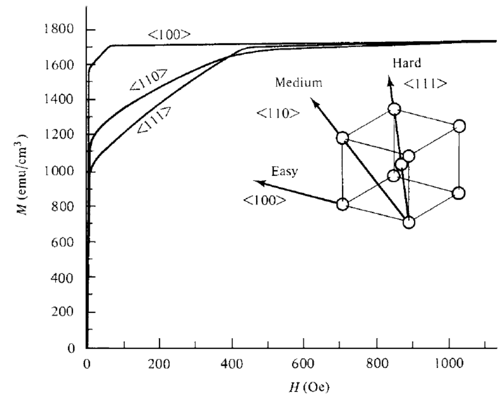

Figure 2.1: Magnetization curves for a crystal of iron [34].

Soft magnetic materials have low anisotropy, making it easier to reorient their magnetization, while hard magnetic materials exhibit high anisotropy, requiring significant energy to change their magnetization direction [31]. Furthermore, Figure 2.2 shows the variation of the anisotropy constant K_1, magnetization M_s, and Curie temperature T_{Curie} as a function of the weight percent of Ni in Ni-Fe alloys. This graph highlights how the anisotropy constant K_1 decreases as the Ni content increases, reaching a minimum near the composition of permalloy ($Ni_{80}Fe_{20}$).

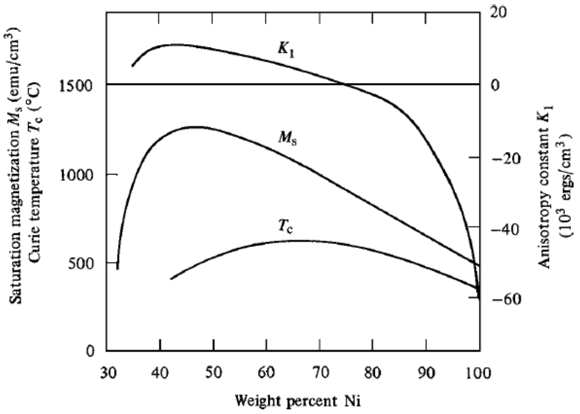

Figure 2.2: Variation of the anisotropy constant K_1, magnetization M_s, and Curie temperature T_{Curie} as a function of the weight percent of Ni in Ni-Fe alloys [31].

Material	K_1 (J/m^3)
Fe	4.8×10^4
Ni	-5.7×10^3
Py	≈ 0

Table 2.1: Magnetocrystalline anisotropy constants K_1 for Fe, Ni, and Py. Data from [34] and [35].

The table clearly shows that iron and nickel exhibit significantly large anisotropy constants, whereas permalloy, an alloy composed of nickel and iron, possesses an anisotropy constant nearly equal to zero. This vanishing constant anisotropy is what classifies permalloy as a soft magnetic material, despite large values of K_1 of its components, iron and nickel. The reduced anisotropy in permalloy arises from the cancellation of opposing anisotropy contributions from its constituent elements (iron and nickel), a direct consequence of the alloy's tailored composition and crystallographic structure [34].

- **Magnetostatic Energy** arises due to the presence of demagnetizing fields (also called stray field outside the sample) at the material's surface [34]. These demagnetising fields or stray fields are generated by the magnetic poles that form at the edges of magnetic samples due to the non-uniform distribution of magnetization. According to Maxwell's laws, magnetic field lines must either form closed loops or extend to infinity. At the boundaries of a magnetic material, where the magnetization is not continuous, opposing magnetic poles (north and south) emerge, creating demagnetizing fields inside the materials. The magnetostatic energy is given by:

$$E_{\text{ms}} = \frac{\mu_0}{2} \int \mathbf{H}_d \cdot \mathbf{M} \, dV, \tag{2.5}$$

where μ_0 is the permeability of free space, H_d is the demagnetizing field, M is the magnetization vector, and dV is the volume element. Stray fields are magnetic fields that extend outside the material due to the non-uniform distribution of magnetization. The strength and direction of stray fields depend on the shape of the material and the *distribution of magnetization.* In thin films, stray fields are stronger in the perpendicular direction, which can lead to a reorientation of the magnetic moment. As a result, the magnetic moment is typically forced to lie in-plane, where the stray field effects are weaker. Minimizing stray fields is crucial in many applications, such as magnetic storage devices, where they can cause unwanted interactions between neighboring magnetic elements [36]. The so-called closure domain in Figure 2.3c eliminates the dipolar energy but introduces a number of domain walls.

- **Zeeman Energy** refers to the interaction between magnetization and an external magnetic field. This energy attains its minimum value when the magnetization vector M is parallel to the external magnetic field B. The expression for Zeeman energy is provided by:

$$E_Z = -\mathbf{M} \cdot \mathbf{B}, \tag{2.6}$$

The total energy density, which includes all contributing terms, can be expressed as:

$$E_{\text{total}} = E_{\text{ex}} + E_a + E_{\text{ms}} + E_Z, \tag{2.7}$$

If exchange interactions were the only forces acting within a ferromagnetic material, the system would exhibit uniform magnetization. However, other energy terms, such as magnetostatic and anisotropy energies, drives the formation of domains—regions of uniform magnetization that minimize the system's total energy (Figure 2.3). To minimize the magnetostatic energy, ferromagnetic materials often subdivide into *magnetic domains* with opposing magnetization directions [31]. This subdivision reduces the overall stray field by canceling out the magnetic poles at the domain boundaries. For example, in a material with two domains magnetized in opposite directions (Figure 2.3b), the stray fields from one domain are partially canceled by the fields from the adjacent domain. These walls possess finite widths, which result from a balance between exchange energy and magnetocrystalline anisotropy.

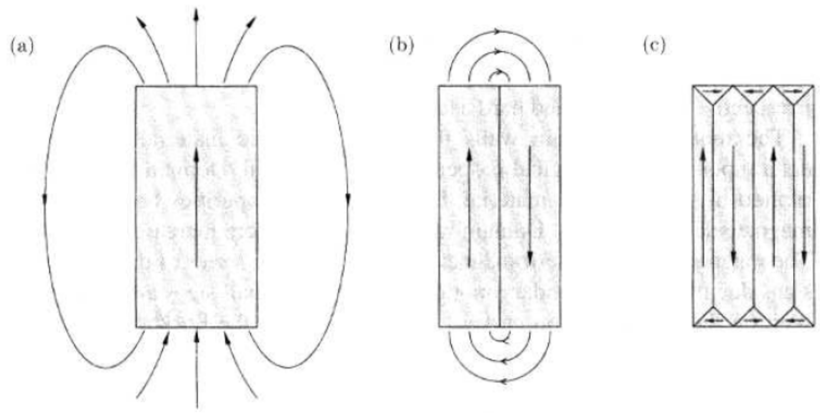

Figure 2.3: A sample which is **(a)** uniformly magnetized, **(b)** divided into two domains, and **(c)** with a simple closure domain structure [31].

Two predominant types of domain walls exist: *Bloch Walls* and *Néel Walls*. In Bloch Walls, spins rotate out of the plane of the wall, a characteristic seen in thicker ferromagnetic films or bulk materials. Conversely, in Néel Walls, spins rotate within the plane of the wall, typically present in thinner films where surface effects are significant [31]. Domain wall dynamics are critical in magnetization processes. When subjected to an external magnetic field, domain walls move, leading to the expansion of domains that align with the field. However, this motion is not uniform; it occurs in discrete jumps as a result of pinning at crystal defects, such as non-magnetic inclusions, or grain boundaries. Such behavior leads to the phenomenon known as **magnetic hysteresis**, observable in the hysteresis loop of the material (Figure 2.4) [34].

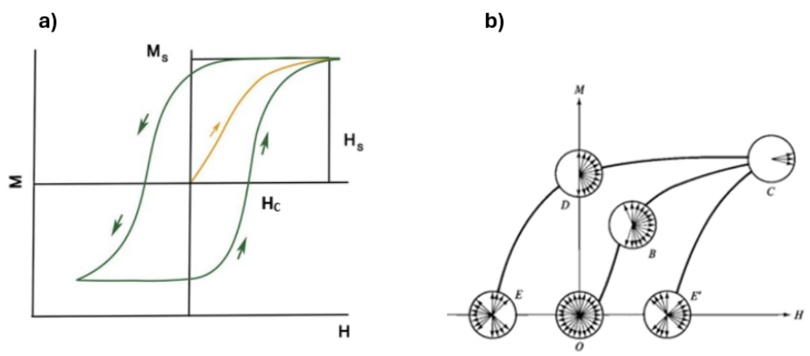

Figure 2.4: The separation of a crystal into distinct domains occurs due to the reduction of the overall sample's magnetostatic energy.

In crystals with minimal defects (particularly in bulk materials), domain walls exhibit greater mobility, resulting in narrow hysteresis loops and soft magnetic properties. This is because the absence of defects allows domain walls to move more freely in response to an applied magnetic field, minimizing energy dissipation and leading to low coercivity.
In contrast, in materials with substantial defects or pronounced magnetocrystalline anisotropy, the movement of domain walls is hindered. This results in

wider hysteresis loops and hard magnetic properties. However, even in these materials, the initial magnetization process (from the demagnetized state) can proceed at relatively low fields, as shown in Figure 2.4b (from point O to B). When an external field is applied to a demagnetized sample, the magnetization M increases with the applied field H according to the initial magnetization curve (OC curve in Figure 2.4). Initially, domains whose spontaneous magnetization is aligned with the applied field grow due to the motion of domain walls, resulting in a rapid increase in magnetization as the field increases. Once the 'knee' of the initial magnetization curve is reached (point B in Figure 2.4), the magnetization of the sample increases further due to the rotation of the domains. Since the magnetocrystalline anisotropy energy must be overcome, a large increase in the field H leads to a relatively small increase in M. When all the domains are aligned in the direction of the field, the maximum magnetization, called the saturation magnetization M_s (Figure 2.4a) is reached, and the field at which the magnetization saturates is called the saturation field H_s (Figure 2.4a).
When the external field is reduced, the M(H) curve differs from the initial one. Specifically, at zero field, the magnetization assumes a finite value because, after the field is removed, the magnetization vectors of the domains do not return to their initial direction but instead align with the nearest easy magnetization direction to the field previously applied. This magnetization is called the remanent magnetization M_r. Assuming that the easy magnetization axes are randomly distributed, the domain vectors are uniformly distributed over half a sphere, as shown at point D in Figure 2.4b. By applying a field in the negative direction to a sample in the remanent state, the directions of the magnetization vectors that were aligned with $+H$ are reversed, bringing the sample to a state of zero magnetization (point E in Figure 2.4b). The coercive field H_c is defined as the field value at which the sample demagnetizes after being saturated [37]. Ferromagnetic materials can be thus categorized based on their magnetic properties, such as coercivity, remanence, and saturation magnetization. These classifications —soft/hard depending on coercivity (Figure 2.5), weak/strong depending on magnetization (Figure 2.6)— highlight differences in how the material responds to external magnetic fields and how it retains magnetization.

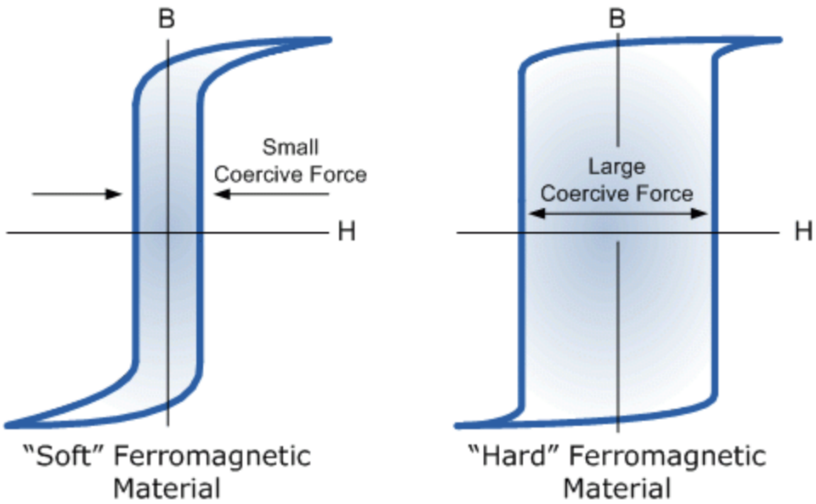

Figure 2.5: Difference in hysteresis loops in a soft ferromagnet versus a hard ferromagnet.

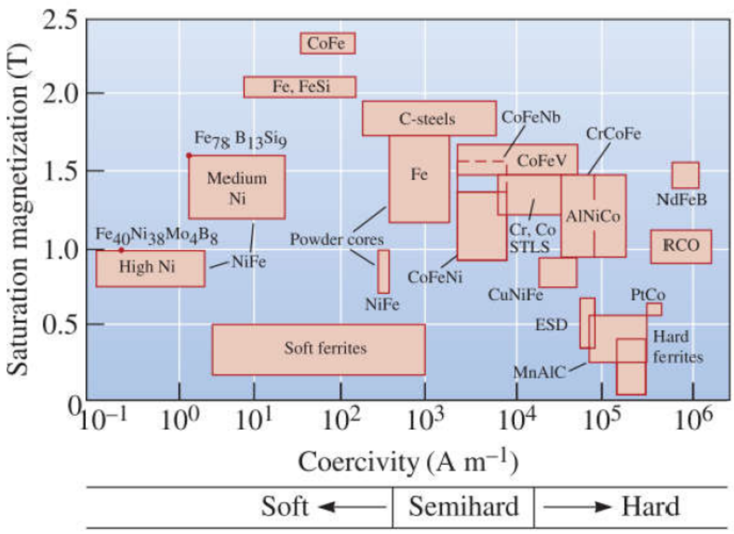

Figure 2.6: Categorization of saturation magnetization and coercivity for different materials. [38]

- **Weak Ferromagnets** exhibit low magnetization due to partial alignment of magnetic moments, often arising from competing interactions such as in antiferromagnetic-like or frustrated structures;
- **Soft Ferromagnets** are characterized by low coercivity, meaning they are easy to magnetize and demagnetize. Examples include Permalloy (Ni-Fe alloys), which demonstrates nearly negligible crystalline anisotropy for specific compositions;
- **Strong Ferromagnets**, such as iron and cobalt, feature higher saturation

magnetization due to strong exchange interactions. They are most often used in permanent magnetic alloys;

- **Hard Ferromagnets**, with high coercivity (greater than 10^4 A/m), retain their magnetization even after the external magnetic field is removed. Their high coercivity arises from significant magnetocrystalline anisotropy, which locks the magnetic moments along preferred axes of magnetization.

Finally, thin ferromagnetic films, which are one of the main topic of this thesis, possess distinct characteristics that set them apart from bulk materials. The reduced dimensionality heightens the influence of surface and interface effects, which often outweigh bulk energies. A notable outcome is the alteration of magnetocrystalline anisotropy. In bulk materials, anisotropy is determined by crystal structure, but in thin films, it is frequently governed by surface phenomena or strain, often orienting magnetization within the plane [39]. In elements like Permalloy ($Ni_{80}Fe_{20}$), these surface effects disrupt the almost isotropic behavior noticed in bulk, resulting in distinctive anisotropic properties in thin films. The diminished thickness also affects the domain structure, leading to reduced domain sizes due to the minimization of magnetostatic energy. In extremely thin films, the system might shift to a single-domain state, simplifying the magnetic configuration. Domain walls in thin films deviate from those in bulk materials, with Néel walls, which reduce out-of-plane stray fields, becoming the prevalent wall type [39]. Moreover, the interplay between exchange energy and anisotropy narrows the wall thickness in thinner films. These thin film phenomena have profound implications for ferromagnetic Josephson junctions. Domain arrangements in the thin ferromagnetic layer induce local fluctuations in the magnetic flux trough the junction, subsequently modulating the junction's critical current, as it will be shown in the Section 2.3.

2.2 Proximity effect

The proximity effect at superconductor/ferromagnet (S/F) interfaces describes the mutual influence between a superconductor and a neighboring metal or ferromagnet. Specifically, it refers to the capability of the superconductor to extend its properties into the adjacent material. In superconductor/normal metal (S/N) systems, this effect leads to a reduction in the critical temperature of the superconductor as the thickness of the normal metal layer increases [10]. At the same time, a weak superconducting state may emerge in the normal metal. The precise outcomes depend on the boundary conditions of the system. The S/N proximity effect can be effectively modeled using Ginzburg-Landau theory [40]. In this framework, for bulk superconductors, the transition between the normal and superconducting phases is a second-order phase transition described by an order parameter that changes from 0 in the normal state to 1 in the superconducting state. In S/N interfaces, the transition between the two phases is more gradual, and for temperatures close to the critical temperature $T \approx T_c$, the energy functional is expressed as:

$$F_{GL} = a(T)|\psi|^2 + \gamma(T)|\nabla\psi|^2 + \frac{b(T)}{2}|\psi|^4, \tag{2.8}$$

where ψ is the order parameter. The corresponding Ginzburg–Landau equation in one dimension is:

$$a(T)\psi - \gamma(T)\frac{\partial^2\psi}{\partial x^2} = 0. \tag{2.9}$$

The solution to this equation is an exponentially decaying function [3]:

$$\psi = \psi_0 \exp\left(-\frac{x}{\xi_N}\right), \tag{2.10}$$

where $\xi_N = \sqrt{\gamma/a} = \sqrt{\gamma/\alpha(T-T_c)}$ defines the characteristic decay length of the order parameter within the normal metal. This coherence length represents the spatial range over which Cooper pair correlations extend into the normal metal and sets the scale of superconducting proximity effects in such structures.

According to BCS theory, as mentioned in Section 1.1, typical Cooper pairs are composed of two electrons with opposite spins. By contrast, ferromagnetic substances host an exchange field that aligns electron spins in the same direction. These properties exemplify fundamentally competing long-range order parameters. Considering that the energy scale of ferromagnetism (ranging from hundreds of meV to a few eV) greatly exceeds that of superconductivity (which in the context of this thesis, is only a few hundreds of μeV for aluminum structures), a significant suppression of superconductivity is expected in superconductor/ferromagnet (S/F) bilayers. Nevertheless, in S/F hybrid nanostructures, the proximity effect can still emerge, although Andreev reflection is partially suppressed. This phenomenon arises from the difference in densities of states at the Fermi level for spin-up and spin-down electrons in the ferromagnetic metal. As a result, an electron in the majority spin band is less likely to undergo hole retroreflection into the minority spin band. The suppression of Andreev reflection is enhanced with increasing spin polarization (P) of the ferromagnetic metal, where P is defined as: P=(N↑-N↓)/(N↑+N↓) with N↑ and N↓ symbolizing the densities of states at the Fermi level [41, 42]. Moreover, the induced electron-hole pair experiences the exchange splitting of the spin bands in the ferromagnet. When Cooper pairs from the superconductor penetrate the ferromagnetic layer, the exchange field (h_{ex}) induces rapid dephasing, causing oscillations in the superconducting order parameter within the F material [40]. This contrasts with the exponential decay observed in normal metals. A schematic of this phenomenon is shown in Figure 2.7. The exchange field imparts finite momentum to Cooper pairs, leading to spatial oscillations in the order parameter. This arises from **Zeeman splitting**: the spin-up electron in a Cooper pair experiences a potential energy reduction ($\hbar = \mu_B h_{ex}$) and a kinetic energy increase, while the spin-down electron undergoes the opposite effect. The resulting momentum shift $2\delta k = \mu_B h_{ex}/v_F$ causes the order parameter to oscillate with wave vector $2\delta k$. Quantum mechanically, this momentum shift introduces a linear phase increase with distance (x) from the

S/F interface. In 1964, Larkin-Ovchinnikov and Fulde-Ferrel (FFLO) proposed a state where superconductivity and ferromagnetism coexist, characterized by a sinusoidal modulation of the order parameter over the superconducting coherence length (ξ_S) [43, 44]. While direct evidence of the FFLO state in bulk superconductors remains elusive, its signatures, such as oscillatory order parameters, align with theoretical predictions and experimental observations in S/F heterostructures [45].

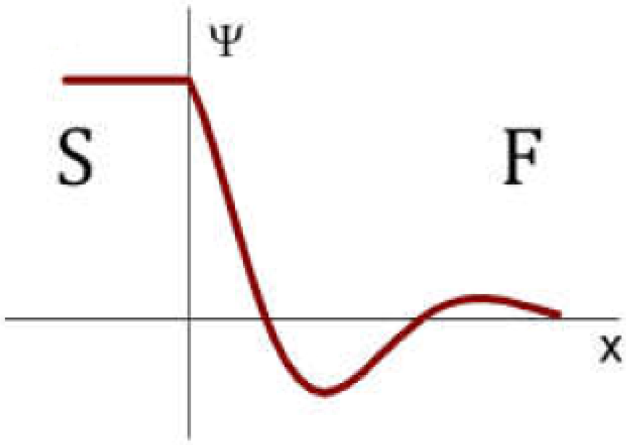

Figure 2.7: Schematic representation of the order parameter behavior at the ferromagnetic boundary.

Therefore, Cooper pair wave function in ferromagnetic layers exhibits a damped oscillatory behavior, which can described by:

$$\psi_f(x) \propto e^{-x/\xi_f} \cos\left(\frac{2\pi x}{\lambda_f}\right), \tag{2.11}$$

where x is the distance from the interface. Here, ξ_f is the decay length, and $\lambda_f = \frac{\hbar v_F}{2h}$ is the oscillation wavelength with v_F representing the Fermi velocity [46], both of which depend on the exchange field's strength and the material's scattering properties [47]. In the dirty limit, ξ_F is defined as:

$$\xi_F = \sqrt{\frac{\hbar D}{2h}}, \tag{2.12}$$

where D is the diffusion coefficient and h is the exchange energy. Since h is typically much larger than the thermal energy $k_B T_c$, ξ_F is significantly shorter than the coherence length in normal metals (ξ_N). For strong ferromagnets like iron (Fe) or cobalt (Co), where $h_{ex} \sim 1$ eV, ξ_F is only a few Ångströms, while in weaker ferromagnets such as copper-nickel (CuNi) and palladium-nickel (PdNi), it remains below 10 nm.
The S/F proximity effect theory identifies three different behaviors of T_c as a function of the ferromagnetic layer thickness (d_F) in S/F bilayers, depending on the thickness of the superconducting layer (d_S):

- **a) Thick Superconducting Layer ($d_S \gg \xi_S$):** When (d_S) is sufficiently large, (T_c) exhibits oscillations as a function of the thickness of the ferromagnetic layer (d_F). The approximated relation is $T_c(d_S) \sim (0.4 - 0.8)T_{C_0}$, where T_{C_0} denotes the critical temperature of the superconductor in absence of the ferromagnet. This phenomenon is shown in Figure 2.8.

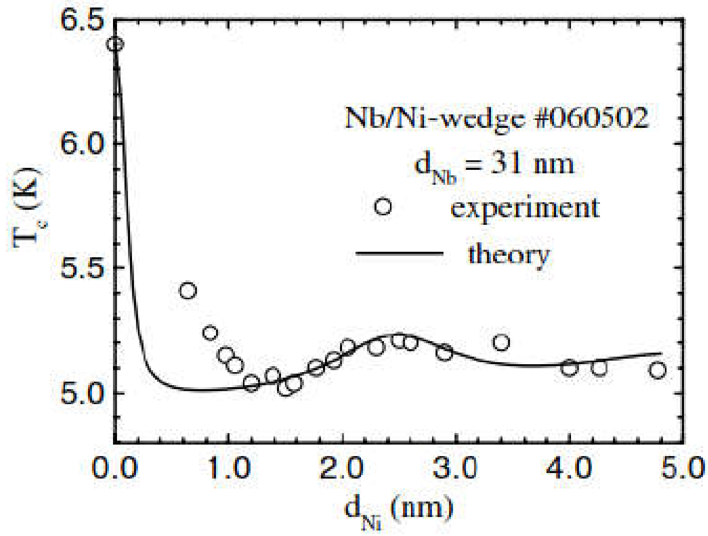

Figure 2.8: dependence of critical temperature in Nb/Ni bilayer as a function of the ferromagnetic layer thickness, for a Nb layer thickness of 31 nm (d_{Nb} = 31 nm) [48]. The transition temperature T_c rapidly diminishes as the ferromagnetic layer thickness increases and exhibits an oscillatory pattern nearing a threshold value.

- **b) Re-entrant superconductivity ($d_S \sim \xi_S$):** When d_S values are smaller, re-entrant superconductivity might manifest. In this scenario, the critical temperature T_c is initially reduced to zero as d_F increases, but with further increments in d_F, superconductivity restores again showing damped oscillations around a certain symptotic value. Figure 2.9 illustrates this phenomenon for various thicknesses of the Nb layer (d_{Nb}). Notably, for d_{Nb} = 7.3 nm, superconductivity is inhibited for d_{CuNi} ranging from 5 nm to 13 nm.

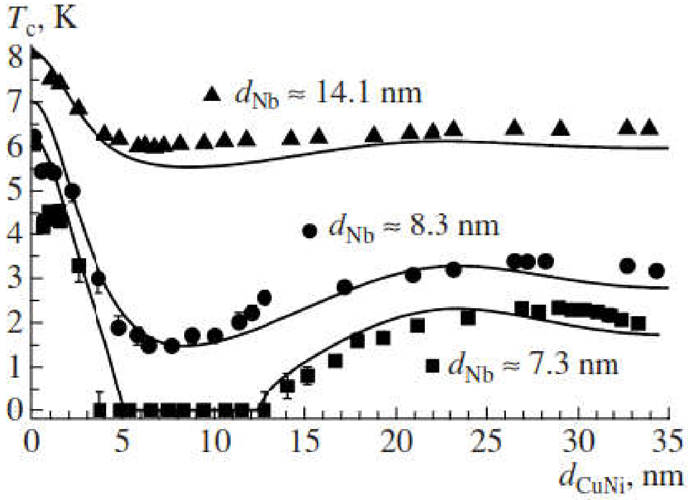

Figure 2.9: Dependence of the critical temperature on the thickness of CuNi $T_c(d_{CuNI})$ in Nb/CuNi bilayer, for different thicknesses of the Nb superconducting layer [49].

- **c) Thin superconducting layers ($d_S < \xi_S$):** In cases where the superconducting layer is extremely thin, the superconducting T_C quickly falls down to zero upon increasing d_F. Figure 2.10 shows the dependence of T_C with the thickness of Nb (d_{Nb}) in Ni/Nb bilayers, for a Ni layer thickness of $d_{Ni} = 8$ nm. The value of T_C steadily decreases as the Nb thickness increases and ultimately disappears at a critical thickness ($d_S \approx 13.9$ nm). This critical point marks the smallest thickness that supports superconductivity in the presence of interactions with the Ni ferromagnetic layer [48].

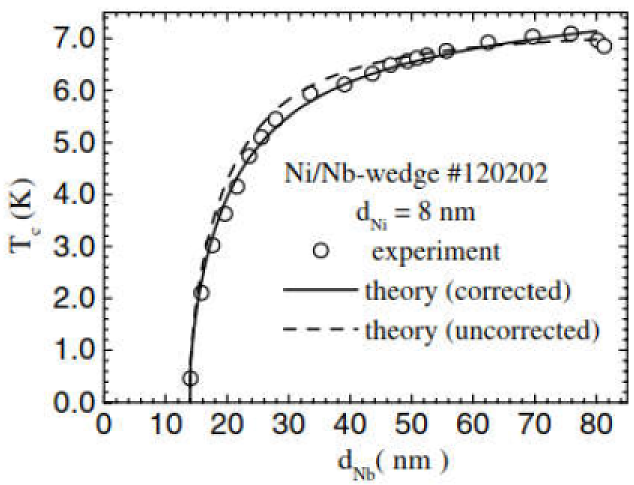

Figure 2.10: Dependence of the critical temperature T_c on the Nb layer thickness in Ni/Nb bilayers where the Ni layer is held constant at $d_{Ni} = 8$ nm.

2.3 Standard SFS

Superconductor-ferromagnet-superconductor (SFS) junctions represent a sophisticated class of Josephson junctions where the interaction between superconducting and ferromagnetic states is prominent, as thoroughly examined in prior sections. The behavior of these junctions, encompassing novel phenomena such as the $0-\pi$ transition, is rooted in these fundamental principles, thereby extending their significance to hybrid quantum systems and upcoming quantum devices. A hallmark of SFS junctions is the oscillatory dependence of the critical current Ic on the ferromagnetic barrier thickness d_F. This oscillatory behavior arises from the interference of Cooper pairs within the ferromagnetic layer and can be expressed as [40]):

$$I_c \propto \exp\left(-\frac{d_F}{\xi_{F1}}\right)\left|\cos\left(\frac{d_F}{\xi_{F2}}+\phi_0\right)\right|, \tag{2.13}$$

where ξ_{F1} and ξ_{F2} are the real and imaginary components of the magnetic coherence length, respectively. As the thickness d_F increases, the sign of I_c alternates, leading to a 0 or π junction state depending on whether the ground state phase difference across the junction is 0 or π. This phenomenon, where the junction transitions between 0 and π states as the ferromagnetic layer thickness is varied, was first observed experimentally in Nb/CuNi/Nb junctions [46]. The current-phase relation (CPR) of SFS junctions deviates from the simple sinusoidal form typical of SIS junctions. In the 0 state, the CPR can be described as [50]:

$$I_s(\varphi) = I_c \sin(\varphi), \tag{2.14}$$

with $I_c < 0$. In proximity to the $0-\pi$ transition, the presence of higher harmonics becomes prominent, resulting in more intricate current-phase relationships (CPRs) characterized by multiple energy minima. These minima permit the stabilization of non-conventional phases, like φ or φ_0 junctions. The multi-valued nature of the CPR introduces dynamic effects that facilitate the stabilization of these nontrivial phases and affect the junction's switching dynamics, thereby making them crucial factors in practical applications. Ferromagnetic junctions have additionally been suggested for use as phase shifters within superconducting quantum frameworks [51], where they demonstrated utility in modifiable superconducting circuits. More recently, these junctions have served as critical elements for sophisticated quantum phase manipulation [52].

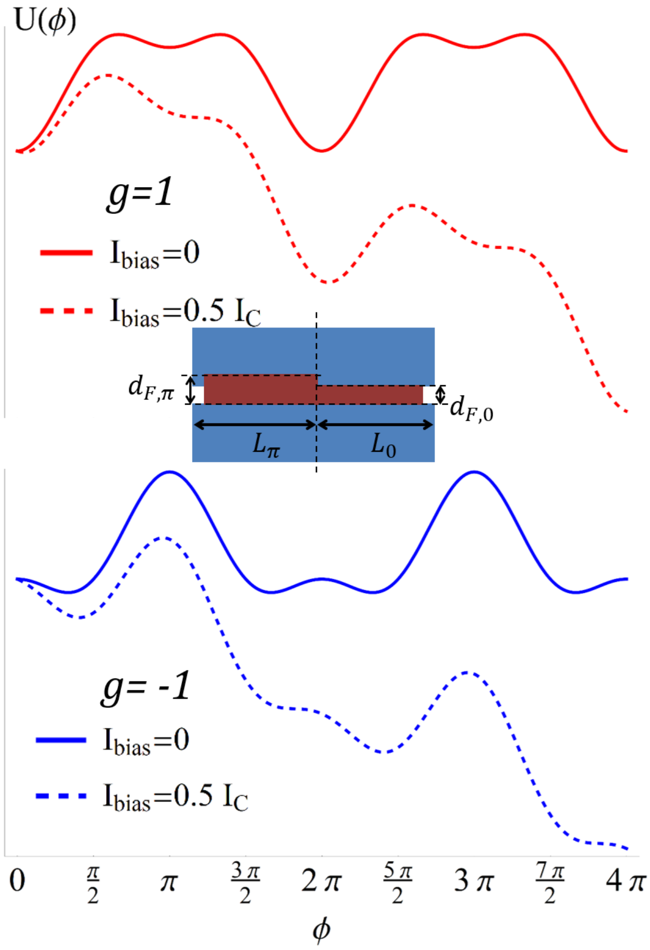

Figure 2.11: Washboard potential for $g = \pm 1$ in absence and in presence of external bias current

It is possible for a $0-\pi$ phase transition to occur in the system when the critical current does not vanish completely due to the presence of higher harmonics in the current-phase relation (CPR). For example, the CPR up to the second harmonic can be written as:

$$I_s(\varphi) = I_{c1}\sin\varphi + I_{c2}\sin(2\varphi), \tag{2.15}$$

where the critical current is a linear combination of I_{c1} and I_{c2}. Even if I_{c1} vanishes, the total critical current remains finite [53]. Two distinct cases can be identified:

- If the ratio I_{c2}/I_{c1} is positive, and the first harmonic changes its sign by varying control parameters, such as temperature or the thickness of the ferromagnetic barrier, a $0-\pi$ transition is observed.
- If the ratio I_{c2}/I_{c1} is negative, the superconducting phase transitions continuously, passing through all values between 0 and π. In this scenario, two critical currents corresponding to the phase differences $-\varphi$ and φ can be measured, forming φ-junctions [51].

φ-junctions were first demonstrated by Sickinger et al. [54], combining a 0-junction and a π-junction to produce a current-phase relation with a non-zero second harmonic. The presence of two distinct switching currents in φ-junctions is attributed to the phase particle dynamics within the system. The washboard potential in the presence of a second harmonic is given by:

$$U(\varphi) = E_{c1}\left(1 + \frac{g}{2} - \cos\varphi - \frac{g}{2}\cos(2\varphi)\right), \tag{2.16}$$

where $g = I_{c2}/I_{c1}$. For $g < 0$, the phase particle can reside either in the φ-well or in the $(\varphi + \pi)$-well. If the particle escapes from the φ-well, the higher mean switching current is observed, whereas escape from the $(\varphi + \pi)$-well corresponds to a lower switching current. On the other hand, for $g > 0$, the maxima and minima in the washboard potential are inverted compared to the previous case. Generally, the phase particle is trapped in the lower potential well, and a higher critical current can only be observed under conditions of low damping. However, this situation is rare in SFS junctions, which typically exhibit overdamped behavior.

Conventional Cooper pairs in superconductors form spin-singlet states (antiparallel spins), which are strongly suppressed in ferromagnetic materials due to the exchange field. In contrast, spin-triplet Cooper pairs—with parallel spins—can propagate through ferromagnetic layers, as their spin alignment renders them immune to pair-breaking effects. While triplet pairs typically require non-collinear magnetization or engineered spin-active interfaces to emerge, their potential to enhance coherence in hybrid systems has motivated extensive theoretical study. In SFS junctions with such non-collinear magnetization or spin-active interfaces, spin-triplet pairs can propagate over significantly longer distances than singlet pairs, extending the effective coherence length. However, realizing triplet pairing experimentally demands more complex structures than conventional SFS junctions. Although these effects are central to superconducting spintronics, their detailed exploration falls outside the scope of this thesis, which focuses on the functionality of SFS junctions as cryogenic magnetic switches. The presence of spontaneous magnetization in the ferromagnetic barrier introduces hysteresis in the critical current's Fraunhofer pattern. The flux contribution from the F layer, Φ_F, is given by:

$$\Phi_F = \mu_0 M_F L d_F, \tag{2.17}$$

where M_F is the magnetization of the F layer, L is the junction's cross-sectional width, and d_F is the F layer thickness. Therefore, the total magnetic flux through the junction, Φ becomes:

$$\Phi = \mu_0 H L d_m + \mu_0 M_F L d_F, \tag{2.18}$$

where $d_m = 2\lambda_L + d_F$ represents the effective magnetic penetration depth, including the London penetration depth (λ_L). This additional flux from the F layer magnetization leads to a shift in the Fraunhofer pattern, resulting in hysteretic behavior of the critical current (I_C) versus applied magnetic field (H). The direction of the shift depends on the direction of the magnetic field sweep. Sweeping from positive to negative fields (down curve) results in a shift towards negative fields due to the positive remanence of the ferromagnet, and vice versa for the up curve (see Figure 2.12).

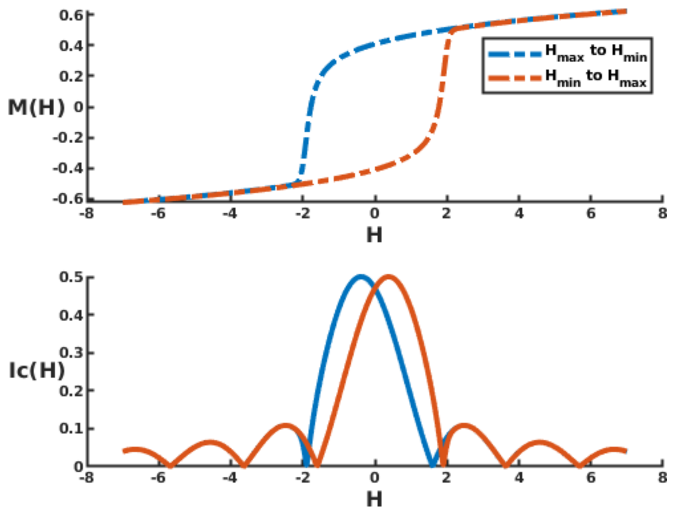

Figure 2.12: The blue and orange curves represent the magnetic response when the magnetic field is directed downward and upward, respectively.

In the simplified case of a homogeneous, single-domain F barrier, we can approximate $\mu_0 M_F \approx \mu_0 M_S \approx \mu_0 M_r$, where M_S and M_r are the saturation and remanent magnetization, respectively. This leads to an offset in the Fraunhofer pattern given by:

$$\pm\mu_0 H_{shift} = \mp\mu_0 M_S \frac{d_F}{d_m}. \tag{2.19}$$

This equation quantifies the shift in the Fraunhofer pattern due to the magnetization of the F layer, highlighting the interplay between the ferromagnetic properties and the superconducting behavior in SFS Josephson junctions. These domains create local variations in magnetic flux that directly influence the junction's critical current (I_C). Variations in the domain structure and domain-wall motion can lead to dynamic changes in the magnetic flux, thereby altering the Josephson current [55]. The use of SFS junctions as units cells in Random Access Memory (RAM) has been demonstrated in Nb/PdFe/Nb junctions [56]. In these memory elements, below the saturation field of the F layer, two critical current levels can be distinguished, corresponding to two memory states. The switch between these states can be achieved by applying magnetic field pulses. A magnetic field bias is typically applied to set the optimal operating point, i.e., the field at which the difference between the higher and lower critical current levels (ΔI) is maximized. If the inital state is the higher critical current state (HI in Figure 2.13), the memory can be switched to the state LO in Figure 2.13, by applying a positive magnetic field pulse. During the rising edge of the pulse, the critical current follows the up curve (red curve in Figure 2.13). On the falling edge of the pulse, the critical current follows the decreasing curve, and after the pulse, the junction settles into the 'LO' state (Figure 2.13).

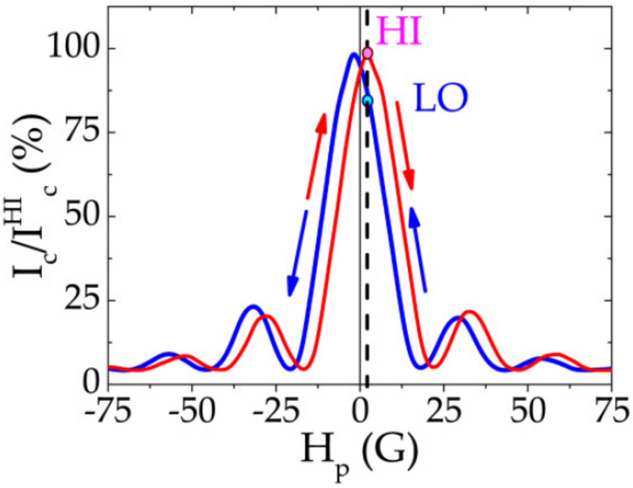

Figure 2.13: Blue and red curves refer to the magnetic field pattern in the downward and upward direction of the magnetic field, respectively. In each plot it's highlighted the low- and high-I_c level states (LO and HI) and the working point (dashed black line) [57].

2.4 SIsFS Josephson Junctions

Due to the presence of metallic barriers, SFS junctions exhibit significant dissipation, posing challenges for their integration into superconducting digital and quantum circuits. In contrast to use the few ferromagnetic insulators, one can exploit Josephson junctions with an insulating barrier and a standard ferromagnetic material in a Superconductor-Insulator-Superconductor-Ferromagnet-Superconductor (SIsFS) configuration. Indeed, SIsFS junctions represent a major advancement in Josephson junction technology, combining the benefits of both SIS and SFS configurations. These hybrid structures harness the unique properties of insulating and ferromagnetic layers, enabling precise control over the junction's electrical and magnetic characteristics, while offering enhanced functionality for superconducting devices [58].

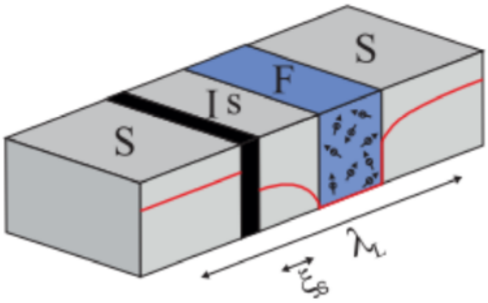

Figure 2.14: SIsFS junction. The red line represents the pair potential distribution across the structure: achieving bulk values within both S-electrodes, it is diminished within the superconducting interlayer s, and disappears in the ferromagnetic layer. The London penetration depth (λ_L) and the superconductor coherence length (ξ_S) are indicated [58].

The SIsFS junction comprises two superconducting electrodes separated by an insulating layer (I) and a ferromagnetic layer (F). The insulating barrier acts as a tunneling barrier, allowing Cooper pairs to transfer between the superconducting layers while reducing detrimental leakage currents. The ferromagnetic layer introduces oscillatory behavior in the superconducting wavefunction due to the exchange field [57], crucial for phenomena such as 0-π transitions, and memory properties [59]. An essential feature of SIsFS junctions is the existence of three distinct modes of transport, as shown in Figure 2.15 [58]. These modes arise due to the interplay between the superconducting, insulating, and ferromagnetic layers, and are determined by the thickness of the ferromagnetic layer, d_s, relative to the superconducting coherence length, d_{sC}.

- **Mode 1 ($d_s \gg d_{sC}$):** In this regime, **(a)** for small F thickness, in the case of $I_{C_{SIS}} \ll I_{C_{SFS}}$ the transport properties are dominated by the SIS part of the junction, the ground state phase difference φ is controlled by the SFS part, allowing for 0- or π-ground states. Consequently, the product $I_c R_n$ is similar to that of a standard SIS junction. The insulating barrier effectively confines the superconducting current, with minimal leakage through the ferromagnetic layer. **(b)** For large values of d_F and exchange field value, the structure behaves like a standard SFS junction.

- **Mode 2 ($d_s \ll d_{sC}$):** In this regime, a weak link is observed across the entire barrier, leading to a significantly diminished supercurrent (represented by the pink curves) similar to that observed in an SIFS junction. The critical current decreases, and the transport properties are characterized by a combination of SIS-like and SFS-like contributions, reflecting the competing effects of the insulating and ferromagnetic barriers.

- **Mode 3 ($d_s \approx d_{sC}$):** In this regime, the junction becomes extremely sensitive to variations of decay lenghts parameters, exhibiting a strong dependence on both temperature and the exchange energy (Figure 2.16). The latter tunes the effective transition temperature T_c^* which is the transition temperature of the sF interlayer, leading to the appearance of a proximity-like tail in the I_cR_N dependence (Figure 2.16).

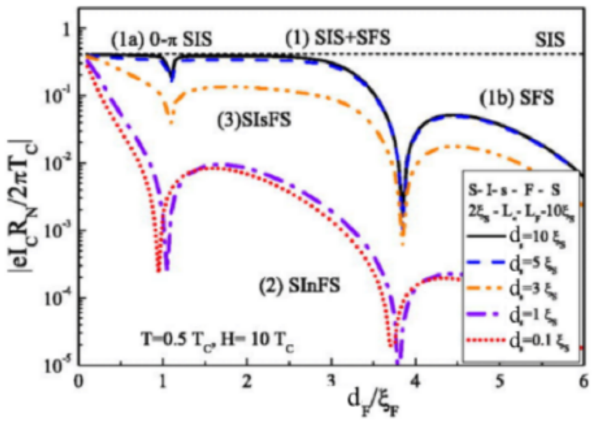

Figure 2.15: The characteristic voltage (I_cR_N) as a function of ferromagnetic layer thickness (d_F) is shown for SIsFS structures with varying superconducting interlayer thicknesses (d_s) at $T = 0.5T_c$. Both d_s and d_F are normalized by their respective coherence lengths, ξ_s and ξ_F. The dashed black line indicates the I_cR_N product for a conventional SIS tunnel junction. Interface parameters are: $\gamma_{BI} = 1000$ (sF interface), $\gamma_{BFS} = 0.3$ (FS interface), and $\gamma = 1$.

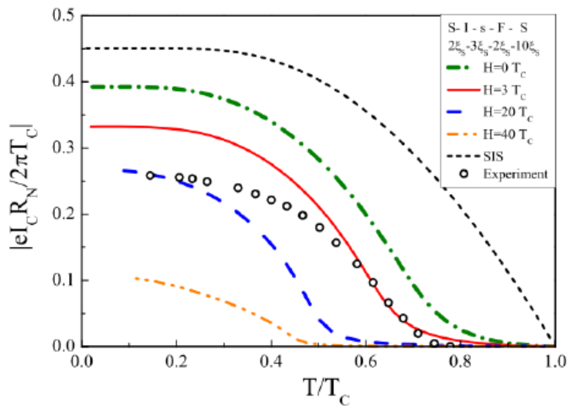

Figure 2.16: The characteristic voltage of SIsFS structures is temperature-dependent across varying exchange field strengths in the F-layer. The short-dashed line illustrates the typical behavior of a conventional SIS tunnel junction. Importantly, the exchange field modifies the effective critical temperature, marking the sF bilayer's transition to the normal state. Experimental measurements on Nb-Al/AlO_x-Nb-$Pd_{0.99}Fe_{0.01}$-Nb junctions verify the presence of this effective critical temperature.

When the SIsFS junction operates in Mode (1a) and is far from the 0-π transition, the current-phase relation follows a standard sinusoidal form (Equation

1.15). Therefore, in rectangular Josephson junctions (JJs), the $I_c(H)$ curves exhibit a Fraunhofer-like dependence as shown in Figure 2.13. In this case, the total magnetic flux through the junction is given by:

$$\Phi = \mu_0 M_F L d_F + \mu_0 H L d_m, \tag{2.20}$$

where $d_m = 2\lambda_L + d_s + d_F + d_I$ represents the thickness of the material penetrated by the applied field. This configuration, with $d_s > d_{sC}$ and $d_s < \lambda_L$, enables the design of switchable elements with high quality factors and low dissipation, making them suitable for digital [59] and quantum electronics [57].
Specifically, the main goal of this thesis is to design a junction that can be integrated into an hybrid transmon architecture, known as the ferro-transmon. The core idea of the ferro-transmon is to integrate a tunnel magnetic Josephson junction into the SQUID loop of a transmon [60]. Compared to a conventional SQUID, the SIsFS JJ offers the possibility to tune I_c, and, consequently E_J, by acting with an external magnetic field pulse in the plane of the loop Φ_L. Formally, the dependence of E_J on Φ_z and Φ_L is given by:

$$E_J\left(\Phi_z, \Phi_L\right) = E_{J\Sigma}(\Phi_L) \cos\left(\pi \Phi_z / \Phi_0\right) \sqrt{1 + d^2(\Phi_L) \tan^2\left(\pi \Phi_z / \Phi_0\right)}, \tag{2.21}$$

where $E_{J\Sigma}(\Phi_L) = E_J^{SIS} + E_J^{SFS}(\Phi_L)$.
The use of a SIsFS as memory element usually requires a magnetic field bias to set the optimal working point in order that ΔI is as large as possible (Figure 2.13). However, for this kind of application it is better to try to engineer the F barrier in such a way to exploit asymmetric minor loops, thus achieving a finite ΔI at a zero-field working point [61]. In this way, it is possible to avoid application of the static magnetic field during qubit operations that may be detrimental for qubit coherence. This means that it may be worth exploring circuit design with a single SIsFS, thus completely eliminating the effect of flux-noise due to the static field [57]. As discussed in Chapter 4, this layout also has significant implications for scalability.

Chapter 3

Materials and Experimental Setup

In this chapter, we present experimental setups and methods used for fabrication, magnetic characterization, and transport measurements of thin ferromagnetic films and Josephson Junctions studied in this thesis. We will first discuss the deposition techniques of ferromagnetic thin films for their optimization as interlayers in magnetic Josephson junctions. Our discussion will cover the analytical and chemical methods employed to study their morphology and composition, as they are crucial for investigating their magnetic properties, which are determined by the measurements with a vibrating sample magnetometer. Finally, we will describe the measurement setup employed to investigate the transport properties of Josephson junctions at temperatures as low as 10 mK. Particular emphasis will be placed on detailing the cooling system, the filtering apparatus, the electronic rack, and the measurement techniques that enable high precision and low noise data acquisition.

3.1 Ferromagnetic materials: thin film deposition and characterization

In this Section, we describe our process to grow NiFe-based alloy thin films by co-sputtering, as well as their chemical and morphological characterization, which provides useful information for discussing the magnetic and transport properties of the resulting devices. This thesis will additionally illustrate the use of chemical-structural analysis methods for characterizing the morphological and structural features of Nb-PyGd alloy samples, eventually extracting parameters useful for the interpretation and discussion of their magnetic and transport properties.

3.1.1 Thin-film growth

Thin films were produced utilizing the sputtering method, which is one of the physical vapor deposition (PVD) techniques. PVD approaches rely on atomic deposition, allowing the film to grow atom by atom on the substrate, without involving chemical processes [62]. During PVD processes, the material aimed for deposition (the target) is vaporized and travels as vapor within a vacuum or

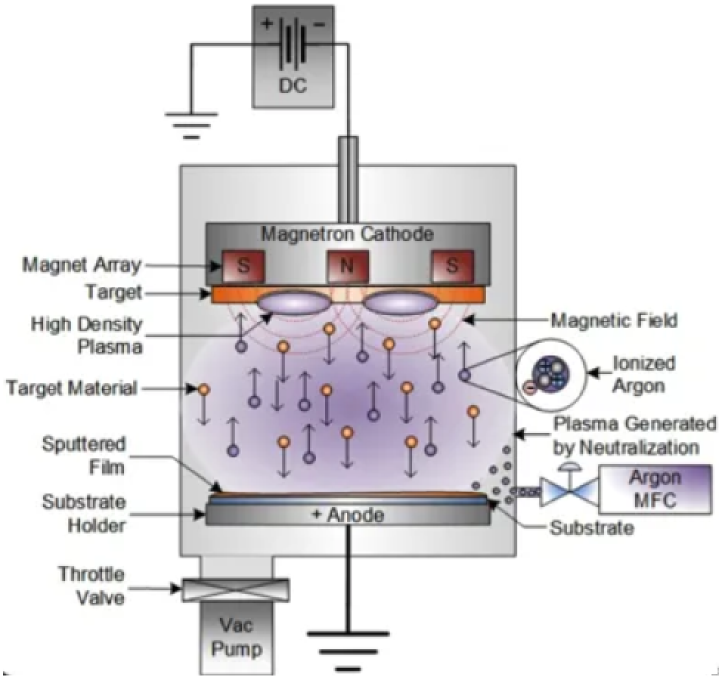

Figure 3.1: Schematic drawing of the DC Magnetron Sputtering Process.

plasma until it condenses onto the substrate. The DC sputtering method (Figure 3.1) is widely applied for growing conductive thin films [63]. In this method, the target is connected to a DC power source, while the substrate, grounded, faces the target. Argon, an inert gas, is introduced into the deposition chamber after achieving a vacuum level of approximately 10^{-7} Torr. A negative voltage is applied between the target and ground, leading to a gas discharge. Argon ions, positively charged, are accelerated towards the target, striking with sufficient energy to release atomic-sized particles, which condense on the substrate thus forming the film. Furthermore, ion-target collisions generate secondary electrons that sustain the plasma. For maintaining plasma, a gas pressure of several hundred mTorr is generally essential [64].
To optimize this method and reduce chamber pressure, vital for film purity, permanent magnets are placed beneath the target in the "DC magnetron sputtering" setup. This arrangement confines secondary electrons near the target's surface through magnetic fields. The confinement of electrons enhances gas ionization, enabling lower chamber pressures for the same applied potential, while minimizing substrate damage due to electron impacts. Compared to other deposition methods, such as thermal evaporation or electron beam evaporation, sputtering provides several benefits: it effectively retains the stoichiometric ratios of alloys [39], yielding uniform films with strong adherence to the substrate. Recent research underscores ongoing improvements in sputtering methods, especially in boosting deposition efficiency and film quality through the refinement of plasma ionization and magnetic field [65].
We have used the system shown in Figure 3.3. The system consists of three vac-

uum chambers. The first chamber is equipped with an ion gun to etch and/or clean the surface of the film. The second chamber is equipped with three magnetron sources for the deposition of different materials and for the co-deposition too. The third chamber has a single magnetron source for permalloy.
For realizing bilayer of Al/FeNi alloys for their magnetic characterization, we begin by cleaning the Al film surfaces using ion etching. This step effectively removes any contaminants and oxides that may be present. The samples were placed on a sample holder in the load lock where at a pressure of 10^{-5} Torr, Argon was introduced until the chamber reached a pressure of 2.15 mTorr, sufficient to start the etching process. The etching was done in 4 cycles of 3'/2'/2'/2' with 2' of rest between each cycle to allow the filament to cool down and avoid overheating. An operation of *pre-sputtering* for 2' was done before moving the sample inside the co-deposition chamber. After the etching process the sample holder was moved, without breaking the vacuum, from the loading chamber to the co-deposition chamber (*Triple magnetron sputtering source* in Figure 3.2, 3.3) with a rod. The $Fe_{76}Ni_{16}Gd_6$ and Nb sputter sources, used in this thesis, have been mounted at a 45° angle to the substrate for the co-deposition. The target-to-substrate distance is adjustable and was fixed at 10 cm for the experiments. Achieving high-purity thin films requires an ultra-high vacuum (UHV) environment. The system employs a rotary pump in conjunction with a turbomolecular pump. The rotary pump reduces pressure to approximately 10^{-3} Torr, enabling the turbomolecular pump to further lower the pressure to 10^{-7} Torr, a level suitable for sputtering processes. Argon, an inert gas, is introduced via a vacuum-tight line equipped with a flowmeter for controlled injection.

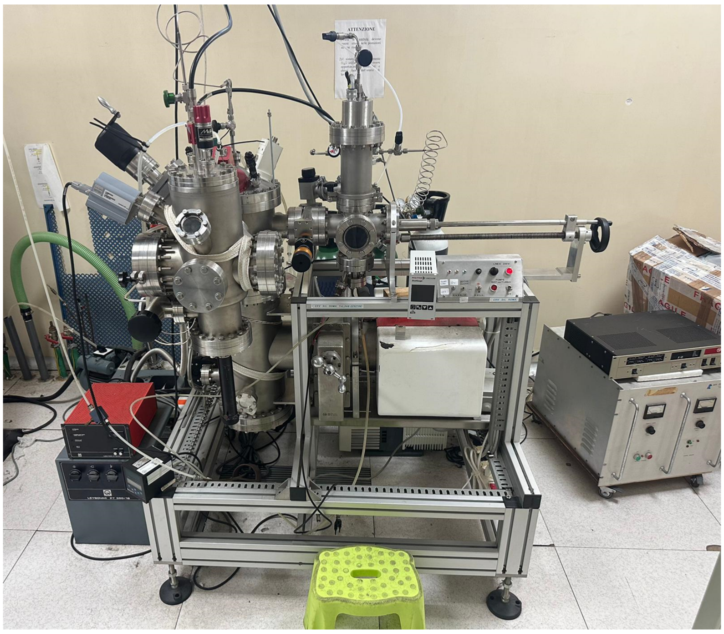

Figure 3.2: Photo of the deposition system.

This multi-stage pumping system ensures minimal contamination during film growth. The films were sputtered under an Ar pressure of 4 mTorr and an Ar flow rate of 40 sccm. The Nb content of the 300∼400 nm-thick films (discussed in the next section) was controlled by varying the Nb source power from 0 to 380 W, while maintaining a constant power of 120 W on the $Fe_{76}Ni_{16}Gd_6$ source. FeNiGdNb films were deposited on sapphire substrates, whereas FeNiGd films were deposited on Corning glass substrates.

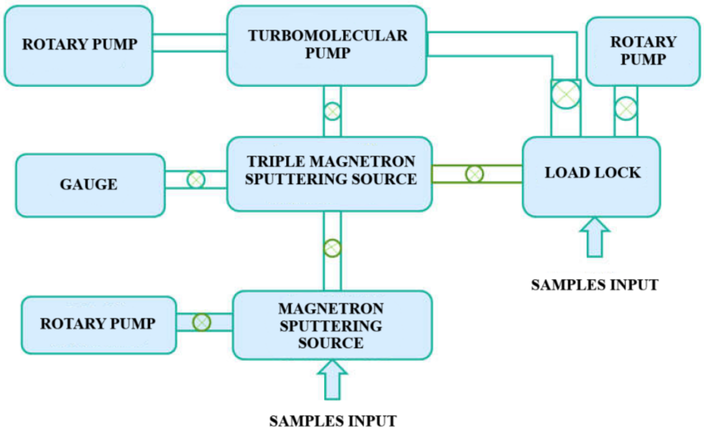

Figure 3.3: Block diagram of the deposition system.

3.1.2 Chemical and structural analysis

When conducting EDS analyses, it was essential to utilize films with thicknesses of the order of hundreds of nanometers to guarantee adequate signal strength. To suppress background noise, Corning glass and sapphire substrates were employed.

Energy Dispersive Spectroscopy (EDS) technique: The samples were analyzed using a *Scanning Electron Microscope* (SEM) equipped with an *EDS* probe to capture detailed surface images and perform chemical analysis (Figure 3.4). The SEM employs a finely focused electron beam to scan the sample's surface, generating secondary electrons that detectors process into high-resolution, black-and-white images with excellent depth of field. Unlike optical microscopes, SEMs achieve about 1000 times higher resolution due to the shorter wavelength of electrons typically in the range of 1 to 20 nm [66]. The resolving power of a microscope is inversely proportional to the wavelength of the radiation used, giving electron microscopes a significant advantage. The SEM comprises several key components: an electron source, a system of electromagnetic lenses to focus the beam, a sample chamber equipped with detectors, and a computer to manage operational parameters. Electrons are typically emitted via thermionic emission from a tungsten filament and accelerated toward a positively charged anode. At the electron gun output, the beam diameter ranges from $10 \div 50$ μm, and condensing electromagnetic lenses narrow it further to $200 \div 5$ nm. Objective lenses then focus the beam on the sample, while electromagnetic coils inside the lenses enable scanning by directing the beam along X and Y coordinates of the sample surface. As the high-energy electron beam (up to 30 keV) interacts with the sample, it penetrates

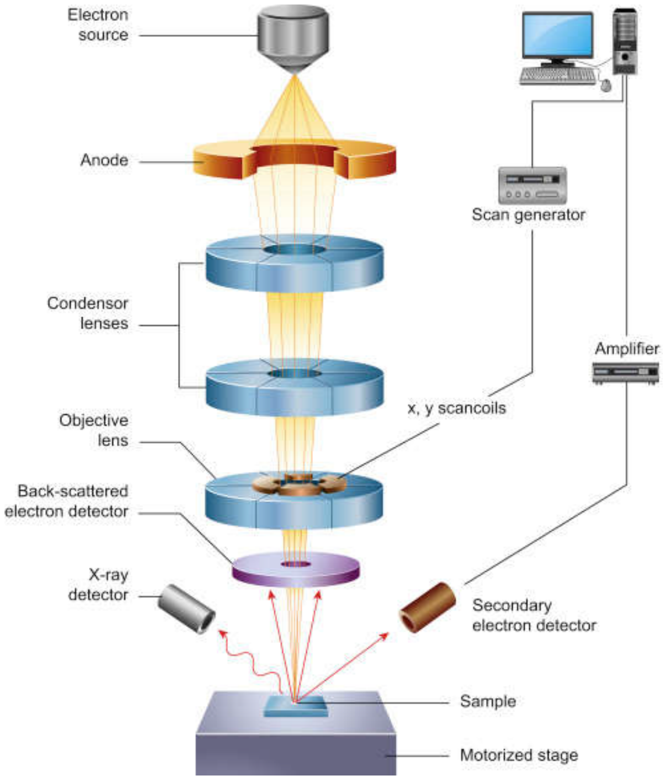

Figure 3.4: Components of the SEM.

up to 1 μm, producing secondary electrons, backscattered electrons, and X-rays. Secondary electrons, originating from the outermost layers of the sample, provide surface topography.; backscattered electrons, resulting from elastic scattering, reveal atomic number contrasts in grayscale images; X-rays, emitted during electron transitions within atoms, characteristic of the elements in the sample. The EDS probe captures this spectrum, displaying photon energies and intensities as a histogram. By comparing the spectrum to standard references, the elemental composition and concentrations are determined. Additionally, compositional maps can be generated by correlating X-ray signals with the position on the sample surface, producing color-coded 2D images that depict element distribution.

EDS results: The analysis, conducted at the MUSA (Multifunctional Materials Synthesis and Analysis) laboratory at the University of Salerno's "E.R. Caianiello" Department of Physics, aimed to provide the stoichiometric ratios of NiFeGdNb films as a function of the Nb power. The instrument was calibrated before each acquisition using a cobalt standard (99.8% Co) to ensure the filament maintained consistent emission efficiency. The measurements were performed by examining five sites on each sample and calculating the average of the results, which yielded the values presented in Table 3.1. To ensure the stability of the electron beam, the process was repeated multiple times, with each iteration followed by a recalibration using the cobalt standard sample. The significant levels of oxygen, silicon, and barium observed in Figure 3.6 are likely a result of electrons penetrating deeply into the film and interacting with the Corning glass substrate beneath. Additionally, the presence of carbon can be attributed to the adhesive used to secure the sample to the sample holder. It is worth noting the presence of other elements originating from the substrate (Figure 3.6), and that the normalized Gd content in the film is lower than in the target; minor peaks are caused by contamination due to the handling of the sample holder. This highlights the importance of this type of analysis. By repeating the analysis on several samples and changing the power delivered to the Nb target, we observed the trend illustrated in Figure 3.7. This figure demonstrates that our chosen power range results in the largest variation in Nb atomic weight within the film, spanning from 10% to 30%.

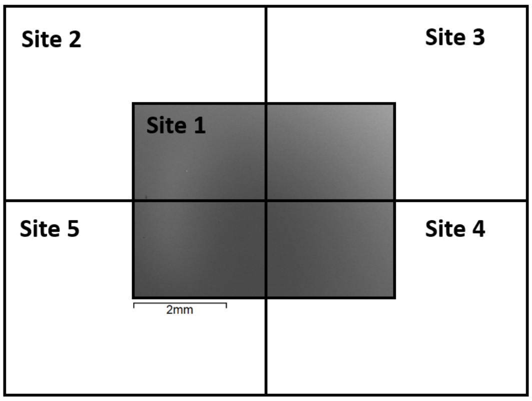

Element	Weight%	Atomic%
Fe	10.88	11.97
Ni	81.16	84.92
Gd	7.96	3.11

Table 3.1: EDS results for the composition analysis of FeNiGd-based alloy film grown on a Corning glass substrate.

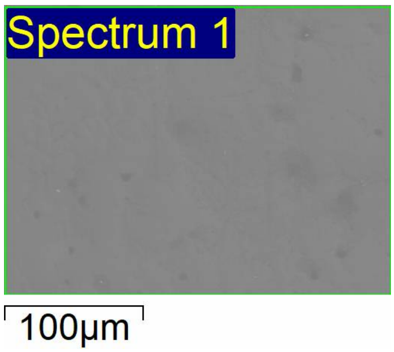

Figure 3.5: SEM image of the sample region.

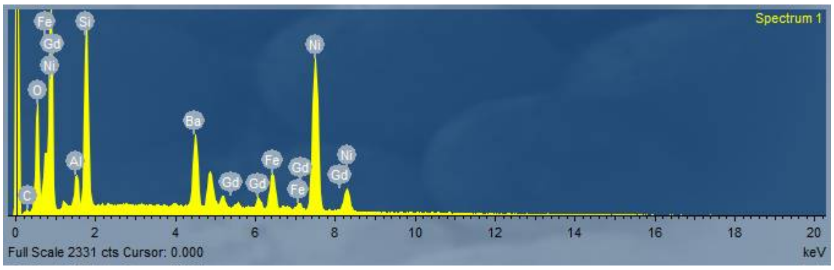

Figure 3.6: EDS spectrum analysis was conducted on the sample region, which comprised a FeNiGd-based alloy film grown on a Corning glass substrate.

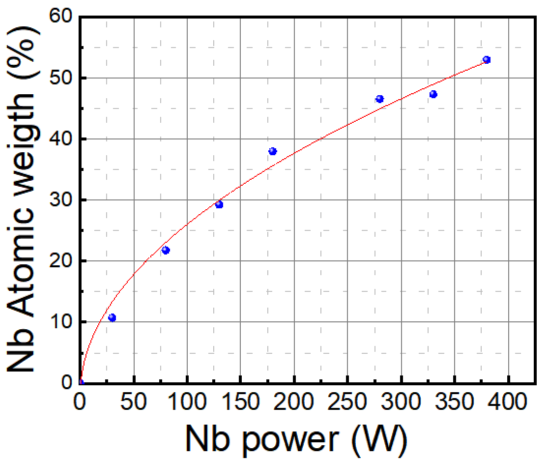

Figure 3.7: The blue dots represent the data, while the red trend line illustrates a square root relationship in the increase of atomic weight.

Atomic Force Microscopy technique (AFM): *Scanning Probe Microscopy* is a branch of microscopy that reconstructs surface images by analyzing the interaction between a physical probe and the sample as the probe scans across it. This approach originated with the invention of the *Scanning Tunneling Microscope* (STM), which maps the tunneling current between a metal tip and a conductive surface to determine surface topography [67]. STM is limited to conductive samples, but *AFM* extends this capability to insulating materials (Figure 3.8). Unlike SEM, AFM does not require high vacuum conditions, allowing analysis in atmospheric or fluid environments. AFM creates nanoscale 3D profiles by measuring the interaction force between a tip and the surface at distances of $0.2 \div 10$ nm. The AFM tip, pyramid-shaped with an apex curvature of less than 5 nm, is attached to a polished cantilever that is $100 \div 200$ mm long. Surface interactions deflect the cantilever, and deflections are measured using the optical method. The cantilever reflects the laser beam onto a photodiode that converts the light intensity into a voltage signal. By processing the signal, the angular deviation and deflection of the cantilever are determined. A feedback circuit controls a piezoelectric scanner that adjusts the samplers position relative to the tip along the z-axis, maintaining constant cantilever deflection. These adjustments allow the tip to trace the

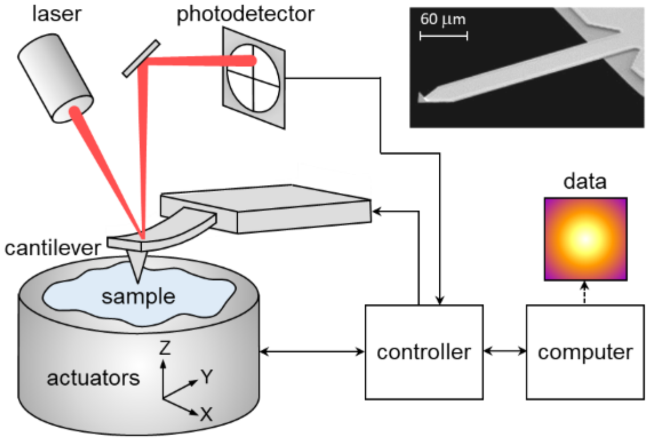

Figure 3.8: Principle of operation of an atomic interaction microscope.

surface irregularities, reconstructing the sample's image from the control signals. AFM operates in three modes (Figure 3.9) [68]:

- **Contact mode:** The tip remains within a few angstroms of the surface, and the interaction force is repulsive. This mode offers high scanning speeds and atomic resolution but risks friction or capillary forces that may distort images or damage soft samples;
- **Non-contact mode:** The tip oscillates $10 \div 100$ Å above the surface, interacting via attractive forces. This technique minimizes forces on both the sample and tip, extending tip life and protecting delicate samples though it may slightly reduce lateral resolution;
- **Tapping mode:** The cantilever oscillates at its resonant frequency, and the tip contacts the surface only at the lowest point of each oscillation. This reduces lateral forces, making it suitable for weakly bound structures and soft materials while preserving image resolution.

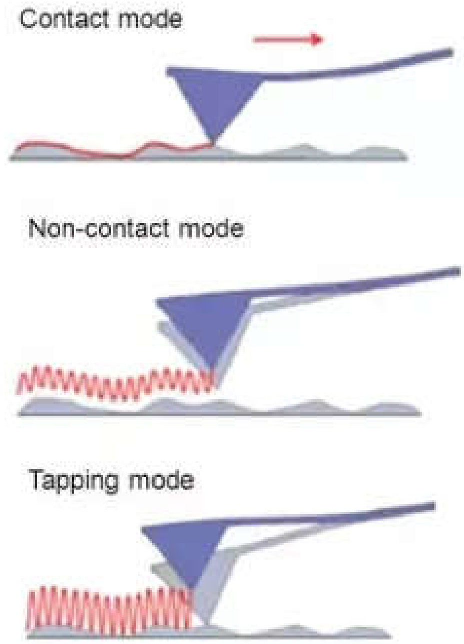

Figure 3.9: AFM image acquisition modes.

AFM's versatility in characterizing various materials and its ability to operate in diverse environments make it an essential tool in nanoscale imaging. However, the choice of mode depends on the sample type and imaging requirements.

AFM results: The analysis of the samples was performed using a Digital Instruments Multi Mode SPM AFM, integrated with Nova analysis software. It was decided to operate in contact mode to obtain higher resolution images.

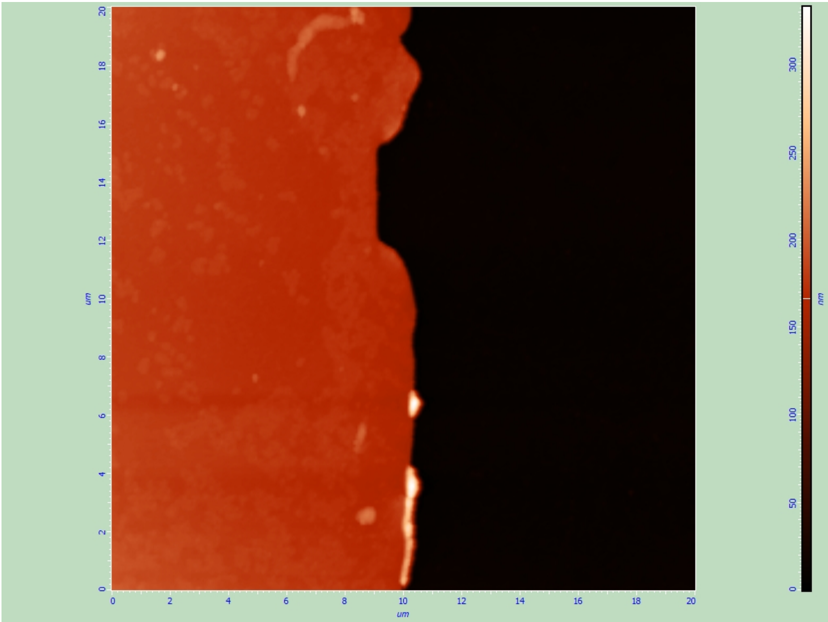

Figure 3.10: AFM image of a 10 μm wide $Ni_{85}Fe_{12}Gd_3$ microstrip obtained by lift-off.

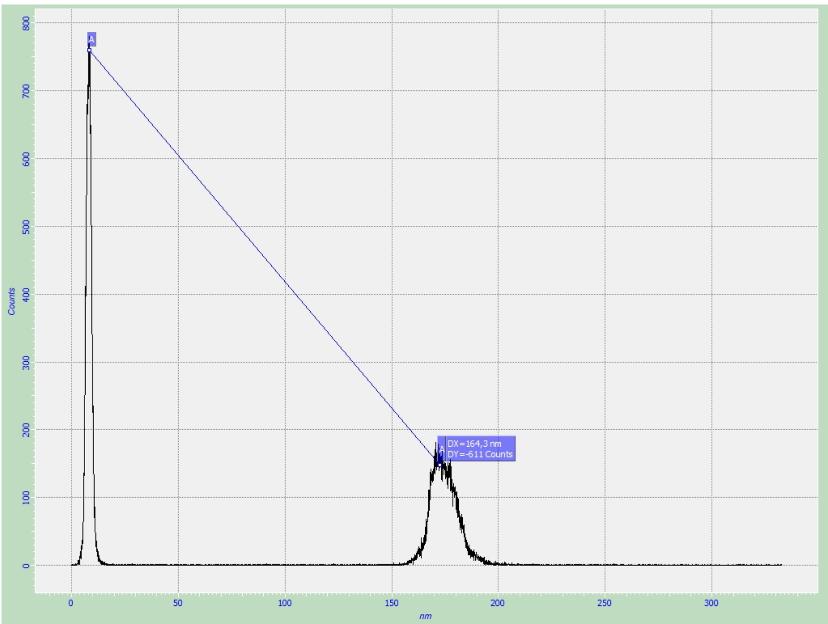

Figure 3.11: *Hystogram step height* function of the Nova program.

Thickness measurements of the microstrips, presented in Figures 3.10 and 3.11, were performed to validate the nominal thickness resulting from the PyGd deposition, which was carried out with a target power of 120 W for 5 minutes, achieving a rate of 0.5 ± 0.1 nm/s. To determine this growth rate, the samples were patterned using lithography and processed with a lift-off technique. These measurements were obtained using the Step Height function within the Nova software, which facilitates relative height determination. Additionally, the surface roughness was

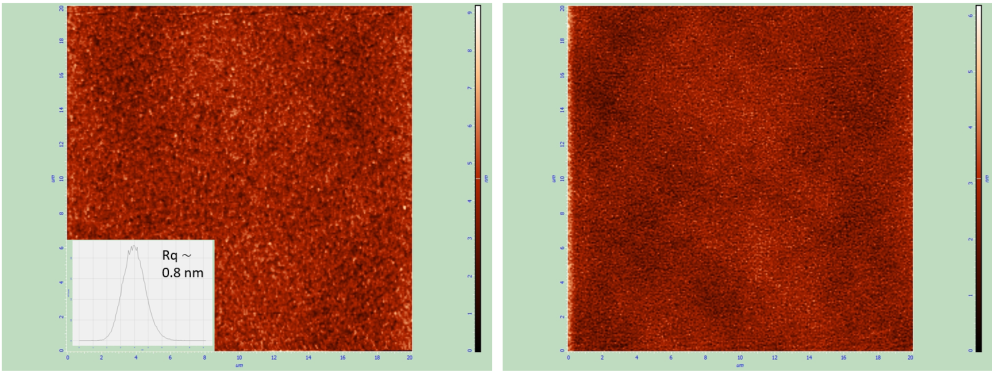

Figure 3.12: AFM image of the surface roughness of the sample before and after etching of the Al film.

evaluated using the Surface Roughness function in the Nova software, yielding a root mean square (RMS) value of 1 nm. This roughness originates directly from the underlying aluminum film, which retains a similar order of magnitude of roughness even after etching, as shown in Figure 3.12. When the ferromagnetic material is deposited, it adopts the same roughness profile as the aluminum film. Even in our case, with 3 nm of permalloy, the roughness remains consistent with that of the aluminum substrate.

3.2 Vibrating sample magnetometer

Magnetic characterization was performed using a *Vibrating Sample Magnetometer* (VSM) shown in Figure 3.13, which enables precise determination of a sample's magnetic moment in a uniform magnetizing field as a function of temperature, field strength, and crystalline orientation, with a resolution of (10^{-6}) emu [69].

Figure 3.13: Vibrating Sample Magnetometer (VSM) from Oxford Instruments-MagLab, available at the laboratory of the "E. Pancini" Physics Department of the University of Naples Federico II.

The VSM indirectly measures the magnetic moment based on Faraday's in-

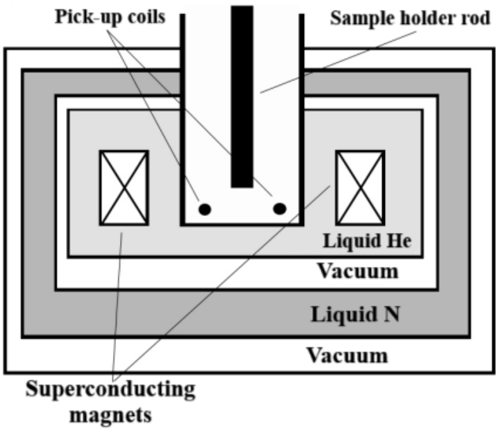

Figure 3.14: System diagram of a Vibrating Sample Magnetometer.

duction law, which states that a time-varying magnetic flux through a circuit generates an induced current. This current, measured in the pickup coils, is directly correlated to the sample's magnetic moment. The sample is attached with Teflon strips to the lower end of a rigid rod and placed in a uniform magnetic field produced by a superconducting magnet made of niobium-titanium filaments embedded in a copper matrix. To generate fields up to 9 T, the magnet is immersed in liquid helium inside a cryostat, thermally isolated from the environment by a liquid nitrogen jacket and a vacuum layer (Figure 3.14). The sample acquires magnetization in response to the field due to the alignment of its magnetic domains or spin moments, which creates an additional magnetic field in the surrounding region. The sample is vibrated to create a time-varying magnetic field, inducing an electromotive force in the *pickup* coils. This signal, proportional to the magnetic moment, is amplified using a *lock-in* amplifier tuned to the sample's vibration frequency [46]. Measurements are performed over a temperature range of $4 \div 300$ K, controlled by a heater, with the magnetic field and temperature monitored via a computer. All operations are managed through *Object Bench* software, which controls the VSM electronics. Sample preparation and positioning in the VSM must be done quickly to minimize air exposure and prevent surface oxidation. Before measurements, the sample is aligned with the pickup coils' point of maximum sensitivity using the "*Moment vs. Z*" function in the software. This process involves controlled movements of the sample along the Z-axis while recording the magnetic moment signal, allowing the optimal Z position to be identified for accurate measurements. Once positioned, the sample is subjected to the external field, and the hysteresis loop is reconstructed by adjusting the field strength through the magnetometer's control software.

3.3 The diluition refrigerator

Before delving into the description of the dilution refrigerator system, it's worth mentioning the theory behind the cooling process. First suggested by H. London in 1951 [70, 71], the operation of dilution is based on the behavior of the $^3He{-}^4He$ mixture according to the phase diagram in Figure 3.15.

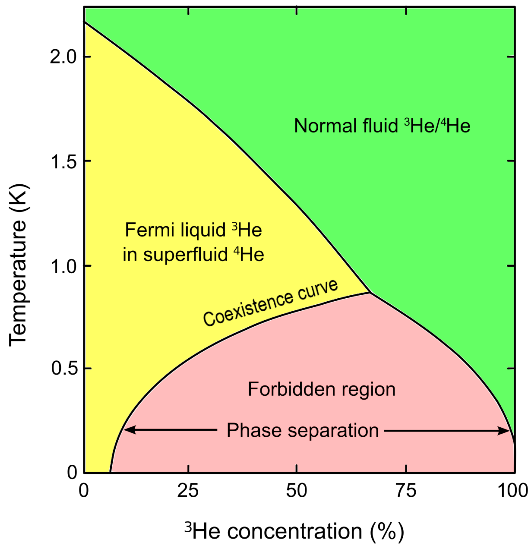

Figure 3.15: Phase diagram of liquid $^3He{-}^4He$ mixtures showing the phase separation.

Above the coexistence curve, occurring at temperatures $T > 0.86\ K$, a homogeneous mixture of ^3He dissolved in ^4He is formed. Depending on the molar concentration of ^3He, this mixture may exhibit either normal or superfluid states. When the temperature is reduced below the coexistence curve for a given concentration $(T, x(\%) \rightarrow T', x'(\%))$, the mixture separates into two distinct phases: one enriched with $^3He(T', x'_C(\%))$, which is lighter, and another richer in $^4He(T', x(\%))$, which is denser. The lighter ^3He phase "floats" on top of the denser phase. To achieve cooling, the ^3He must be extracted from the enriched region by external pumping. Since the vapor pressure of ^4He is negligible at low temperatures, only the ^3He evaporates. This evaporation cools the system by lowering the temperature. In dilution cryostats, the separation process between richer and poorer regions of ^3He varies depending on the system design, with "*wet*" and "*dry*" cryostats being two common configurations. Wet cryostats require cryogenic liquids, while dry cryostats do not.
To conduct D.C. measurements at temperatures as low as 10 mK, we use a Triton refrigerator system from Oxford Instruments. This Triton setup is a cryofree cryostat, signifying that it doesn't require cryogenic fluids to attain temperatures down to several milliKelvin. It comprises multiple stages with descending temperature gradients as shown in Figure 3.16 , all sealed within a cylindrical high vacuum chamber known as the *outer vacuum chamber* (OVC). The tempearture of the plates are:

- the RT-plate, at room temperature;
- the 77K-plate, at ∼70 K;

- the 4K-plate, at ∼4.2 K;
- the Still-plate, at ∼0.7 K;
- the IAP-plate, or cold-plate, at ∼0.1 K;
- the MC-plate, at ∼10 mK, which includes a mixing chamber where the ^{3}He dilution occurs.

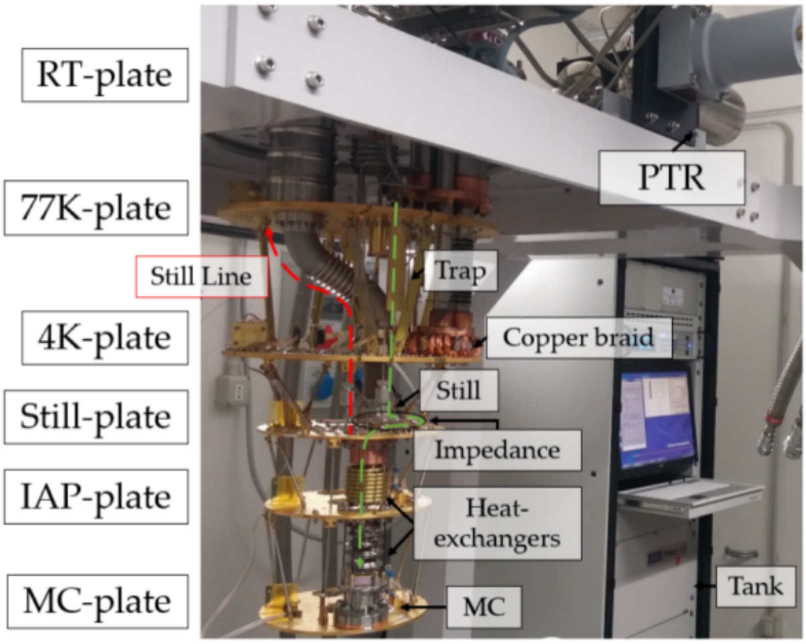

Figure 3.16: The cryostat with the temperatures of each stage and the main cooling lines on the left, while on the right a zoom of the dilution unit.

A high vacuum is necessary to isolate the system from environmental interactions, with the pressure maintained below 10^{-5} $mbarr$. The stages are constructed from copper, with gold and silver-coated plates, thermally isolated by stainless steel supports. The initial cooling stage of the Triton Dilution Refrigerator involves the use of a pulse-tube cooler (A). This stage brings down the system's temperature to around 10 K. The pulse-tube cooler controls pressure waves to compress and expand a gas, resulting in cooling and heat removal. The dilution unit (DU) allows for the condensation of the helium gas mixture into a liquid state, achieving high pressures and low temperatures. It is characterized by the Still, some heat exchanger and the mixing chamber as in Figure 3.16. The dilution refrigerator stage is utilized to achieve extremely low temperatures. It involves a mixture of ^3He and ^4He isotopes. By carefully controlling the dilution process, the mixture undergoes phase separation in the mixing chamber, with ^3He becoming superfluid while ^4He remains in its normal state. This phase separation creates an environment of extremely low temperatures, reaching as low as a few millikelvin (thousandths of a Kelvin). The condensation process of the ^3He gas is achieved using the Joule-Thompson (JT) stage. This stage comprises a highly efficient heat exchanger positioned within the Still pumping line (right in Figure 3.16) and an impedance where the gas can experience isenthalpic expansion. Being more specific, inside the Still, a heat exchanger cools the returning ^3He liquid before it reaches the continuous counter-flow tube-in-tube heat exchanger (top - right in Figure 3.16). The continuous heat exchanger further cools the ^3He to below $0.1K$. Following this, the ^3He passes through several step heat exchangers composed of discrete blocks of sintered silver with internal flow channels. Finally, the ^3He enters the mixing chamber where dilution cooling takes place due to the enthalpy difference between the concentrated (incoming) and diluted (outgoing) liquid. While the incoming liquid is nearly pure ^3He, the diluted liquid predominantly consists of ^4He with a small fraction of ^3He. The diluted ^3He flows from the mixing chamber to the Still, where it is preferentially evaporated and circulated by the pumping system.

3.3.1 Filters

In experiments performed at very low temperatures, measurements are highly susceptible to interference from external factors or noise. Noise is defined as any undesired signals or distortions that may compromise the precision of the measurements. Sources of noise include temperature fluctuations, electronic disturbances, and various environmental elements. Since these measurements predominantly focus on examining quantum effects, maintaining a high degree of accuracy is crucial. The presence of noise in the measurements can skew the results and hinder the extraction of valuable information about the properties under investigation. To address these issues, a series of filters is implemented to reduce unwanted frequency signals. These filters are anchored at different temperature stages, and they include:

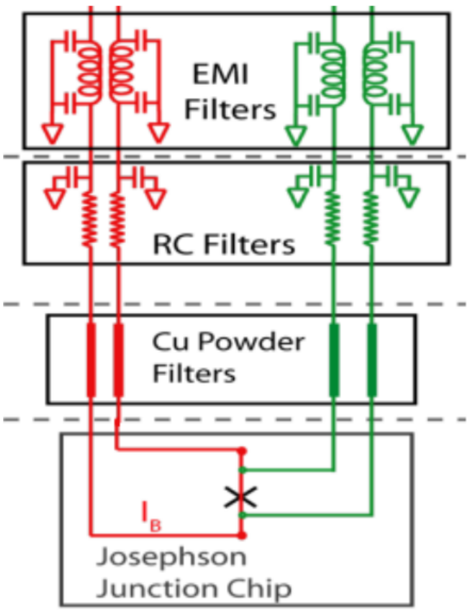

Figure 3.17: Schematic diagram illustrating the filters employed within the Triton system.

- **EMI Filters** (Electromagnetic Interference Filters): Shown (Figure 3.18), these filters are engineered to reduce electromagnetic high frequency peaks. Various sources, such as power lines, radio frequencies, or other electronic gadgets, can produce electromagnetic noise. These filters mitigate unwanted electromagnetic noise by employing impedance matching and frequency-selective attenuation before it reaches sensitive electronic components. Typically, EMI filters comprise passive elements like capacitors, inductors, and resistors, configured in a particular pattern. In our instance, the components are configured to form Pi-filters, which include two capacitors and one inductor, arranged in a triangular formation.

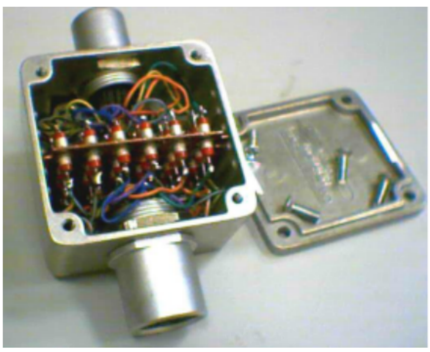

Figure 3.18: The Triton system's installed EMI filters are illustrated.

- **RC Filters:** Within a low-pass RC filter, the resistor is configured in parallel with the input signal, while the capacitor is arranged in series with the output, as depicted in Fig 3.19. This setup permits lower-frequency components to pass and dampens higher frequency components. The cutoff frequency is the threshold where the filter starts to reduce signal strength. In our scenario, the filter is composed of two capacitors, each with a capacitance of $1nF$, and a resistor with a resistance of 100Ω, leading to a cutoff frequency of $1.6MHz$. These filters make up the second stage and are positioned at the still plate ($4K$). It is essential to recognize that the actual performance of an RC filter can be influenced by factors such as component tolerances, temperature changes, and impedance interactions with the load and source. Therefore, to address more precise or stringent filtering needs, Pi-filters are employed alongside the RC filters.

Figure 3.19: Image depicts a sequence of RC filters applied to DC lines within the Triton system.

- **Copper Powder Filters:** Depicted in Figure 3.20, copper mesh filters, also referred to as copper powder sintered filters, represent a category of porous filters created from copper particles or copper powder. These filters are produced by compressing and sintering copper powder particles, resulting in a solid yet porous form. The sintering process entails heating the copper powder to a temperature below its melting point, which causes the particles to fuse and form a network of interconnected pores. In our specific instance, they consist of a spiral coil of insulated wire enclosed within a tube filled with copper powder, having a grain size from 5 to $30\mu m$, yielding an extensive effective surface area. They possess a cutoff frequency in the range of several GHz and are situated at the cold plate ($100mK$). They are chosen for their conductive characteristics, including electromagnetic shielding, EMI/RFI filtering, and grounding functionalities.

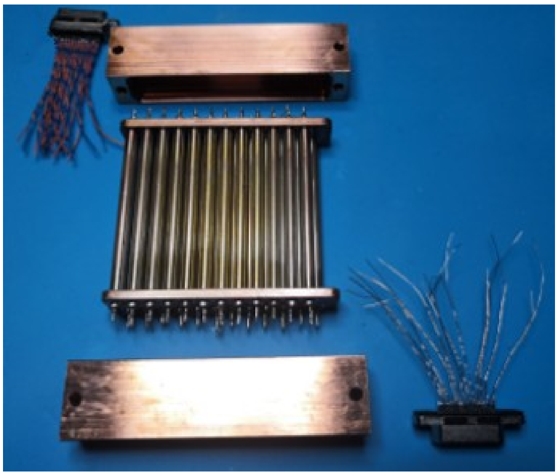

Figure 3.20: Assembly of copper powder filters.

The setup of the cryostat's DC line includes a total of 20 filtered lines, and 6 non-filtered. These are divided into 10 lines for current signals, 10 lines for voltage signals, 4 non filtered lines for a on-chip magnetic control through an *airbridge* (on-chip coil), and 2 non-filtered lines for a NbTi magnetic coil around the sample holder. As the electrical signals travel through the cryostat's plates, they pass through lines made from different materials. For the current signals, copper is used from room temperature to the $4K$ stage. From there to the mixing chamber, NbTi is employed for its superconducting properties, which ensure minimal energy dissipation. For voltage signals, the lines are made entirely of manganin, spanning from room temperature to the mixing chamber. Unfiltered copper lines take an alternative path, beginning at a cinch connector on the RT-plate, proceeding straight to the 4K-plate, and continuing with NbTi filaments (embedded in a copper stabilizing matrix) to a subsequent cinch on the MC-plate.
This arrangement enables the examination of 5 distinct junctions, as well as the management of 2 arbridges and a coil.

3.4 Measurement setup

The electronics are designed for four-contact measurements using two pair of electrodes, one for current bias of the junction and the other for voltage reading. The advantage of this setup is the exclusion of the voltage drop caused by the impedance of the filters, which would add to the voltage drop across the junction. The main instruments used to perform *I(V)* measurements are:

- A *LeCroy Wave Runner 6100A* oscilloscope;
- An *SR570 Standard Research Systems* preamplifier;
- An *Agilent 33120A* waveform generator;
- An *EG&G Princeton Applied Research 5210* lock-in amplifier;

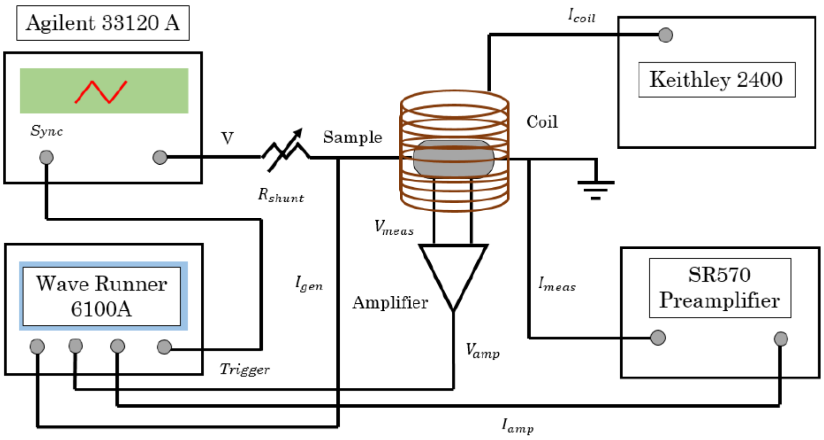

Figure 3.21: Setup configuration for I(V) measurements.

- a *Source Meter Keithley 2400* used as a current generator to produce magnetic fields.

In Figure 3.21 it is shown a scheme of the setup for the four-contact measurements. The current (I_{gen}) originates from a waveform generator signal V_{pp} (peak-to-peak) passing through a variable shunt resistor R_{shunt}, and is directed both to the oscilloscope and the junction input; the resulting output current (I_{meas}) is also monitored by the oscilloscope. The waveform generator simultaneously delivers the same low frequency signal (approximately 1 Hz) as a reference to the oscilloscope. The bias current I_{meas} is given by:

$$I_{\text{bias}} = \frac{V_{pp}}{R_{\text{shunt}} + R_{\text{line}} + R_{\text{junction}}} \sim \frac{V_{pp}}{R_{\text{shunt}}}, \tag{3.1}$$

it is necessary that $R_{\text{shunt}} \gg R_{\text{line}} + R_{\text{junction}}$. The voltage pair V$\pm$ (V_{meas}) is routed to a preamplifier, which amplifies the signal before transmitting it to the oscilloscope. To avoid noise caused by the electrical network, the preamplifiers are operated mainly in battery mode, and the generators are decoupled from the ground of the laboratory.
A diode thermometer with a low sensitivity to temperature, approximately 1×10^{-4} K, is used for precise thermal evaluations. While the precise quantification of temperature error poses challenges due to its dependence on the temperature range, it is effectively minimized through multiple filtering and thermal anchoring techniques in the cryostat. The current-voltage (I-V) characteristics derived from junction transport studies reveal a noise band attributed to both thermal and electromagnetic sources. Figure 3.22 illustrates an enlarged depiction of this noise band at zero voltage for a benchmark superconducting nanostructure, exhibiting a width of $\Delta V = 7\mu V$. This results in a relative error of $\Delta V/V = 1\%$ in the measurement of potential V, which consequently affects the I_C.

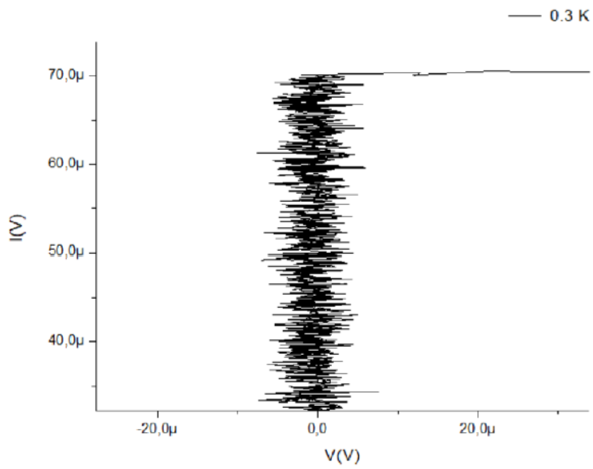

Figure 3.22: Detailed examination of the I-V curve for the Al nanowire at 0.3K: noise region associated with the zero voltage condition

To perform measurements in the presence of an external magnetic field, the Source Meter Keithley 2400 is employed as a current source. It is connected to a superconducting NbTi coil, which is mechanically fixed to the mixing chamber of the Triton dilution refrigerator. The coil's current-to-magnetic field conversion factor is 0.1 T/A, with a current-induced magnetic field error specified at 0.5% of the applied current. The measurement process begins by ramping the magnetic field from zero to an upper limit (virgin curve), followed by sweeping the field from a positive maximum to a negative maximum (down curves) and then returning to the positive maximum (up curves). During the process, IV characteristics are recorded for each magnetic field value. The current step size (ΔI_{coil}) and the waiting time between measurements (t_w) are optimized for accuracy, with $t_w = 1\,\text{s}$. An average of 20 sweeps is used for data acquisition. The Keithley 2400 is interfaced with a PC through a GPIB (General Purpose Interface Bus) connection, and the measurements are automated via LabVIEW software.

Chapter 4

Data analysis

The most widely used superconducting qubit design, the transmon, has led to significant progress in the realization of quantum circuits and quantum computers, but still faces some architectural challenges. The frequency-tunable transmon enables fast two-qubit gates, but its sensitivity to flux noise in SQUIDs affects phase coherence times, which typically scale to values of the order of a few μs. Additionally, the milliampere currents used to control the flux lines inductively coupled to the SQUID cause heat dissipation and introduce qubit cross-talk, complicating the scalability of the overall circuit. To mitigate these challenges, a junction incorporating a ferromagnetic layer that enables in-plane tunability has been proposed in the so-called ferrotrasmon architecture (Section 2.4). In this chapter, we will discuss some key aspects for the experimental validation of the ferrotransmon. We will begin by comparing the behavior of SIS and SIsFS junctions, where the F-layer is made of Permalloy (Py = $Ni_{80}Fe_{20}$) [72]. We will evaluate their potential in the development of the ferrotransmon due to their low-dissipation and energy scales, while also considering its drawbacks, such as the need for fields exceeding 40 mT to exhibit the required properties of switching. To address this issue, we have focused our efforts on optimizing FeNiNb alloys to reduce their coercive fields, as demonstrated in the magnetic measurements with the VSM presented in Section 4.2. To further assess whether this material enables on-chip control of the SIsFS junction, we have characterized flux coils capable of providing in-plane fields on the order of 5 mT - a novel approach, as SQUIDs typically require out-of-plane magnetic fields. The comparative analysis led us to identify $(Ni_{85}Fe_{12}Gd_3)_{80}Nb_{20}$ as a promising alloy for the development of ferromagnetic junctions compatible with the ferrotransmon.

4.1 SIS and SIsFS junctions

It is worth noting that qubits composed of Nb possess shorter coherence times when compared to their Al counterparts, as indicated in previous studies [73, 74, 75]. Consequently, the research initiated by investigating SIsFS junctions using Al electrodes and Py as the F barrier. The choice of Py ($Ni_{80}Fe_{20}$), a strong ferromagnet, was motivated by its ability to scale SIsFS junctions down to submicron dimensions [61]. As previously discussed in Section 2.1, this material exhibits high remanence and vanishing in-plane magnetic anisotropy (Figure 2.2), which are crucial for stabilizing distinct memory properties in nanoscale devices. Unlike softer ferromagnets, such as $Pd_{99}Fe_{01}$ [59], which suffer from percolative exchange interactions at reduced dimensions, Py provides superior magnetic properties for reliable operation.

Here is a brief summary of the fabrication process of the SIsFS JJs analyzed in this thesis. An $Al/AlO_x/Al$ trilayer has been deposited in an ultra-high vacuum system using dc magnetron sputtering onto a 3-inch oxidized Si wafer that had been patterned via optical lithography. The base and top Al layers have thicknesses of 200 nm and 35 nm, respectively. The AlO_x tunnel barrier was formed by introducing dry oxygen into the chamber up to 200 Torr after depositing the bottom layer. After the liftoff procedure, the junction areas were defined using optical lithography and created through an anodization process, where the top Al layer was fully anodized under constant current. Additional insulation was provided by a 150 nm thick SiO_2 film, deposited using rf magnetron sputtering. The next step involved depositing a Py layer via dc magnetron sputtering after soft Ar ion cleaning of the top Al surface. Finally, a 350 nm thick top Al counter electrode was deposited using a subsequent dc sputtering and lift-off process, resulting in the overall SIsFS structure. For reference, conventional SIsS JJs were also fabricated from the same wafer, excluding the ferromagnetic layer deposition. Further details can be found in the reference [76].

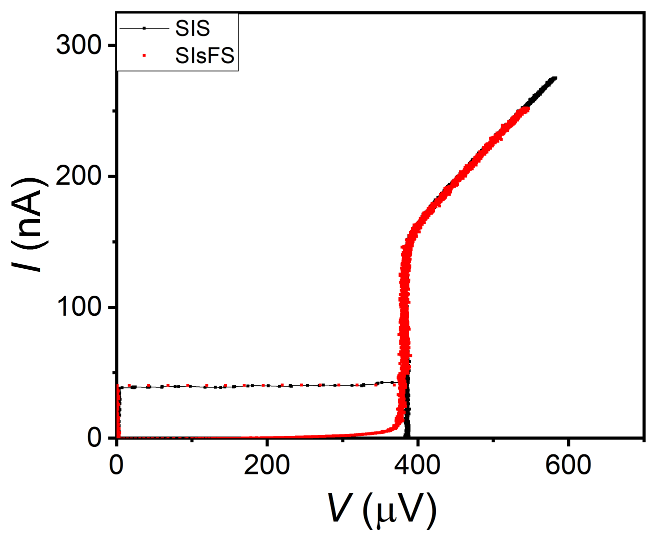

Figure 4.1: I-V curve characteristic at base temperature 10 mK: for a SIS junction (AI (200 nm)/AlO_x (3 nm)/AI (350 nm)) (black curve) and for a SIsFS junction (Al (200 nm)/AlO_x (3 nm)/Al (30 nm)/Py (3 nm)/Al (350 nm)). Both JJs are circular junctions with a diameter of 4 μm (red curve).

An in-depth examination of the I-V characteristics permits the determination of fundamental transport parameters (Figures 4.1 - 4.2). These include the critical

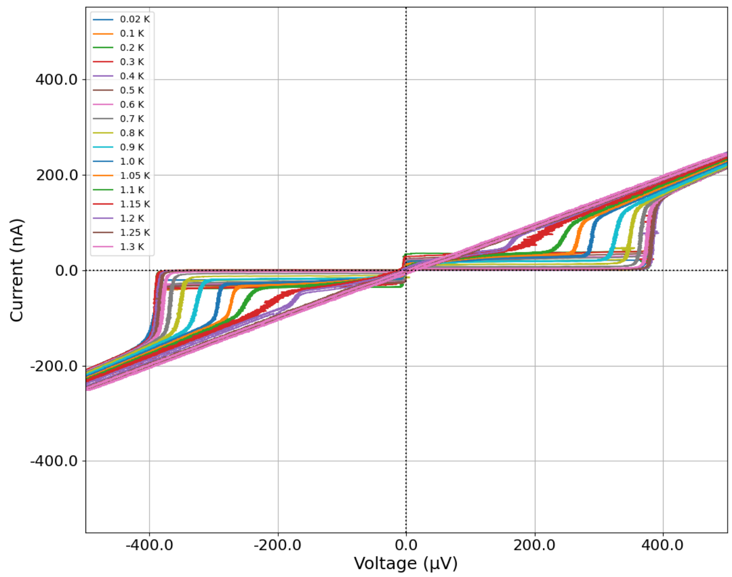

Figure 4.2: I-V characteristics of the SIsFS as function of the temperature, as depicted in the label.

current, denoted I_C, normal resistance R_N, and the gap voltage V_{gap}. Given the stochastic nature of the switch from superconducting to ohmic branch, each individual curve comprises an average of 100 measurements. For the estimation of the critical current, we set a voltage threshold to determine when the device switches to the resistive branch both for positive and negative values, labeled as I_{C_+} and I_{C_-}, respectively. We then calculate the final critical current I_C as $= \frac{|I_{C_+}|+|I_{C_-}|}{2}$, incorporating a measurement uncertainty of 3%. This estimation is grounded in the switching current distributions observed in previously examined SIsFS junctions [77]. To estimate the gap voltage, V_{gap}, for each temperature curve, one can differentiate the I-V curve and determine the voltage where the dI/dV exhibits its maximum. To enable a comprehensive comparison between the SIsFS and SIS data, both sets were subjected to analysis using a fitting procedure based on the BCS approximation relations [78] within the weak coupling limit, which describes the temperature dependence of $V_{gap} = \frac{2\Delta}{e}$, and the Ambegaokar-Baratoff expression for the behavior of $I_c R_N$ [79]:

$$\frac{2\Delta}{e} = \frac{2\Delta_0}{e} \tanh\left(1.74\sqrt{1 - \frac{T}{T_c}}\right), \tag{4.1}$$

$$I_c R_N = A\frac{\pi}{2}\frac{\Delta(T)}{e} \tanh\left(\frac{\Delta(T)}{2k_B T}\right). \tag{4.2}$$

In these expressions, the fit provided estimates of the critical temperature $T_C = 1.3$ K and the zero-temperature superconducting gap $2\Delta_0/e = 390$ μV. The factor A serves as a fitting parameter to account for any observed suppression relative to the theoretical predictions [72]. The suppression of I_C can ultimately be attributed to either the existence of paramagnetic impurities within the insulating barrier or the development of thin normal layers on the surface of the superconducting electrodes [80]. In our case A is of order of ~ 0.3. The corresponding trends are illustrated in Figures 4.3 and 4.4.

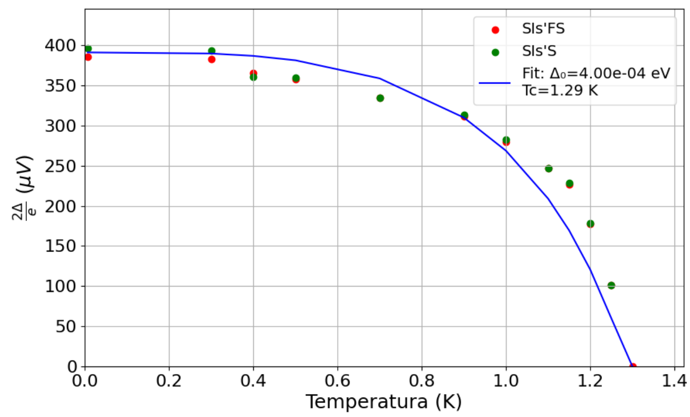

Figure 4.3: The evolution of $\frac{2\Delta}{e}$ as a function of the temperature is illustrated here. The dataset for a circular SIsS junction is represented in green, while the data corresponding to SIsFS is shown in red. Both JJs are circular junction with a diameter of 4 μm. The fitting curve, depicted in blue, has been determined using equation 4.1.

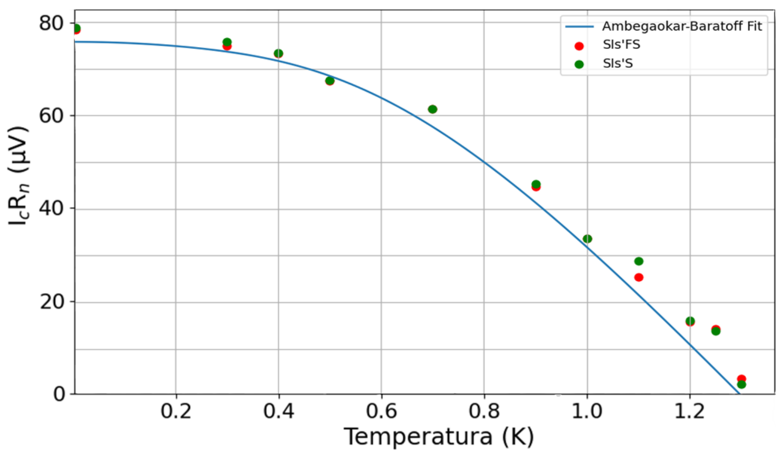

Figure 4.4: The evolution of I_CR_N as a function of the temperature is illustrated here. The dataset for a circular SIsS junction is represented in green, while the data corresponding to SIsFS is shown in red. Both JJs are circular junction with a diameter of 4 μm. The fitting curve, depicted in blue, has been determined using equation 4.2.

JJs	D (μm)	J$_c$ (A/cm^2)	R$_N$ (kΩ)	I$_c$R$_N$ (μV)	$2\Delta_0/e$ (μV)	Q factor	E$_J$ (μeV)
SIS	4	0.32±0.06	1.73±0.06	69 ± 3	395 ± 4	10	82 ± 2
SISFS	4	0.32±0.06	1.75±0.06	70 ± 3	403 ± 4	10	82 ± 2

Table 4.1: Parameters of the SIS and SIsFS Josephson junctions at $T = 10$ mK. The quality factor $Q = 10$ is calculated using the relation $Q = \sqrt{2eI_cR_N^2C/\hbar}$, where the capacitance C is derived from the empirical relation established in [81].

A summary of the main electrodynamic parameters at 10 mK can be found in the table 4.1. The error in the critical current density J_c is calculated through error propagation, considering a 10% uncertainty in the JJ area due to a standard lithography process. The 3% error in R$_N$ is derived from the noise bar observed in the superconducting branch, with a 2% voltage error and a 1% current error, as discussed in the Section 3.4. To calculate the capacitance C, the empirical relation from Maezawa et *al.* [81] is employed: $\frac{1}{C_S}$ (cm^2/μF) $= 0.2 - 0.043 \log_{10} J_c$ $\left(\text{kA/cm}^2\right)$, where C_S is the specific capacitance. As explained in Section 2.4, the consistency of the I$_C$R$_N$ values across the entire temperature range confirms that the SIsFS junctions work in Mode 1 (a), as outlined in the theoretical framework for hybrid SIsFS structures [58]. This regime occurs when the ferromagnetic layer thickness d_F is small and the s-thickness interlayer d_s is large compared to the superconducting critical thickness d_{sc}. In this regime, the SIsFS junction behaves as a series combination of an SIS and an SFS junction, and since $I_{C_{SIS}} \ll I_{C_{SFS}}$, the transport is dominated by the SIS part of the junction. Since the device operates in Mode 1 (a), the insulating barrier (I) effectively suppresses leakage currents, confining quasiparticle tunneling primarily to the sFS interface. Indeed, both junctions show a subgap resistance three orders of magnitude higher than the normal-state resistance $R_N/R_{sg} \approx 10^{-3}$, maintaining the low dissipation characteristic of SIS junctions, as shown in Figure 4.1. Therefore, the SIsFS configuration enables a fabrication process that begins with a conventional SIS junction, followed by the *ex-situ* deposition of the ferromagnetic layer, without compromising the transport properties or the integrity of the tunnel barrier. Additionally, the observed E_J values (82 μeV $\approx$ 20 GHz) are comparable to the typical range for conventional transmons ($E_J \sim$ 10-30 GHz) [82], and compatible with a ferrotransmon design [57].

4.1.1 Magnetic patterns

As explained in Section 1.2.2, the relationship between the critical current of a Josephson junction and an externally applied magnetic field reflects diffractive phenomena. This occurs because the external magnetic field, H, induces a phase variation in the macroscopic wave function of the bulk superconductors, directly affecting the critical current. Magnetic field measurements are performed using a current-polarized NbTi superconducting coil, which generates a magnetic field H orthogonal to the junction. The current-voltage (IV) characteristics are measured at a base temperature of 20 mK as a function of the magnetic field, which is swept over ranges on the order of millitesla. The critical current is then determined as a function of the applied magnetic field, and the behavior of the I-V characteristics is analyzed under varying magnetic fields. The resulting patterns for the tunnel junction and the SIsFS junction, which includes a ferromagnetic layer of $Ni_{80}Fe_{20}$, are presented below.

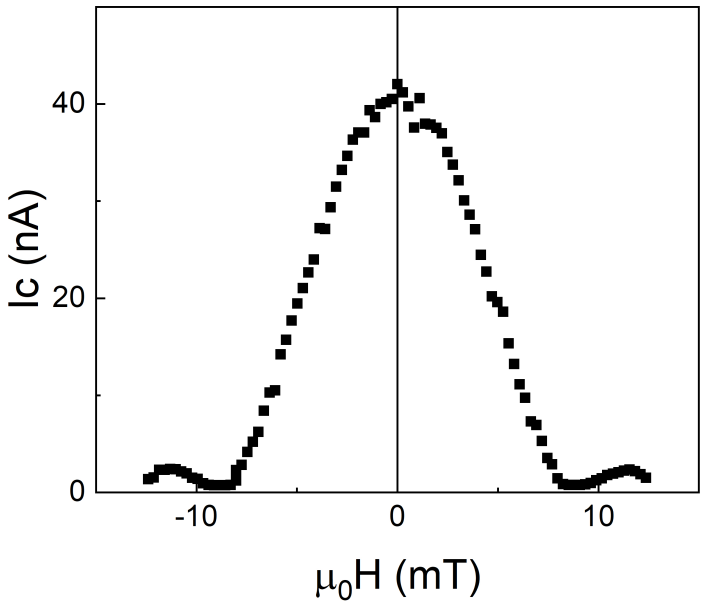

Figure 4.5: Plot of I_C in function of magnetic field at 20 mK for the SIsS junction.

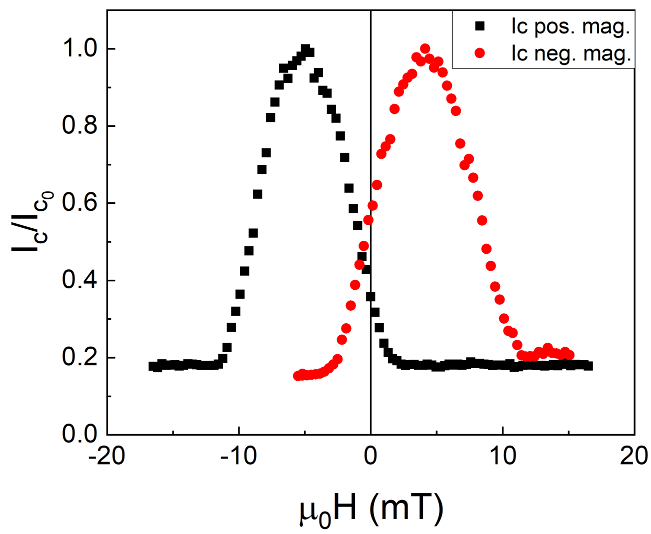

Figure 4.6: Plot of I_C in function of magnetic field at 20 mK for the SIsFS junction after the application of a 50 mT external field.The red and black curves illustrate the magnetic pattern in the down and up direction of the magnet, respectively.

To ensure that the SIsFS junction behaves as a series connection of a SIS and a SFS junctions, while still preserving the magnetic hysteresis characteristic of a SFS junction, it has to satisfy the condition $d_s < \lambda_L$ (where d_s is the superconducting layer thickness and λ_L is the London penetration depth). For a tunnel SIS JJ, the London penetration depth can be estimated from the first minimum $\mu_0 H_{min}$, corresponding to the magnetic flux $\Phi = 1.22\Phi_0$. Considering the geometrical parameter of our SIS JJs, the London penetration depth for aluminum is estimated as $\lambda_L \approx 35\,\text{nm}$, which is larger than the sample thickness d_s. This ensures that the SIsFS junction behaves as a single element in external magnetic fields, exhibiting hysteretic $I_c(H)$ behavior.
Experimentally, by applying cycles of an progressively strong magnetic field, we observed that the junction did not exhibit irreversible behavior below 50 mT and only a standard pattern centered in 0 is observed (Figure 4.5). To prevent flux trapping, and given that the critical field for aluminum is merely 10 mT [83], it was essential to heat the sample to roughly 2 K (above T_C), then apply a magnetic field of $H = 50$ mT in one direction. Subsequently, the sample was cooled to the base temperature to stabilize this remanent state. This process induced a negative shift in the Fraunhofer pattern due to the positive remanent magnetization. The temperature was then raised once again to 2 K and a magnetic field of $H = -50$ mT was applied in the opposite direction. Finally, the sample was cooled again to the base temperature to verify the new remanent state, leading to a shift of the I_c(H) curve towards positive fields. This technique ensured a controlled acquisition of remanent magnetization in the ferromagnetic layer, facilitating repeatable and precise adjustments of the Fraunhofer pattern. Experimental observations in Figure 4.6 confirm that SIsFS junctions serve as viable switchable magnetic elements, as also indicated by prior research [46, 84]. It is crucial to reduce the applied magnetic field strength to enable an on-chip control and to avoid flux trapping in the aluminum electrodes. In the following section, we will illustrate how doping the Py with Nb and Gd enhances the magnetic properties of the F barrier, thus enabling the magnetic switch of the SIsFS JJs at significantly lower magnetic fields.

4.2 VSM measurements

To scale square-shaped Josephson junctions (JJs) to submicron dimensions, robust ferromagnetic materials exhibiting substantial remanent magnetization and in-plane magnetic anisotropy are essential for distinguishing between the two critical current states [61]. Thin ferromagnetic layers typically exhibit an easy magnetization axis aligned parallel to the film plane to minimize magnetostatic energy contributions arising from shape anisotropy [85]. However, certain materials, such as Co/Ni multilayers [86], CuNi [87], PdNi [88], and Co-based alloys [89], display out-of-plane anisotropy, which prevents the shift of the I_c(H) curves. Despite these challenges, the NiFeGd alloy we discussed in Section 3.1.2 fulfills the necessary criteria due to their high remanence, in-plane anisotropy, and favorable switching characteristics, including relatively low coercive fields. NiFe alloys [90, 91], specifi-

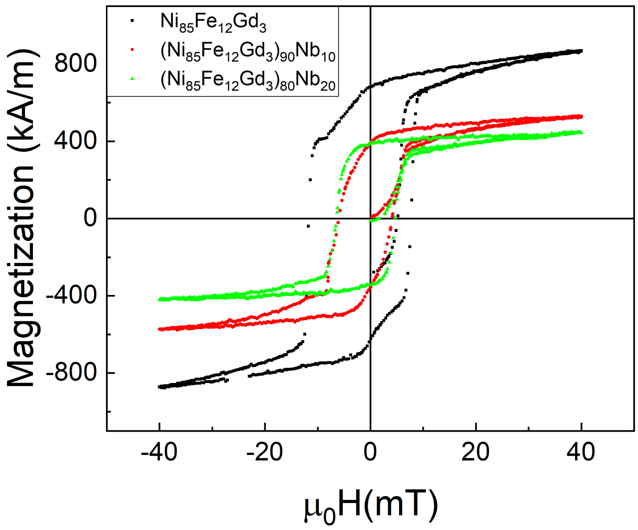

Figure 4.7: Hysteresis loops recorded at 40 mT for a 6-nm-thick FeNiGd alloy with varying concentrations of Nb doping. Data for only the first three samples are shown for clarity. The progressive decrease in magnetization with increasing Nb content highlights the role of Nb in diluting the ferromagnetic matrix.

cally NiFeNb have been investigated in magnetic Josephson junctions with Nb layers for spintronics and digital electronics applications [92, 93]. Given our interest in fabricating ferromagnetic junctions with aluminum electrodes for implementing hybrid superconducting quantum circuits, it is essential to characterize the magnetic response of such films on aluminum, considering the potential influence of the substrate on the properties of the F film due to factors such as elastic strains, surface anisotropy, magnetostatic interactions, and others [94]. Most importantly, so far the primary goal for superconducting memories has been to achieve a sharp switch to distinguish between two logic states (0 and 1), typically realized through magnetization processes involving coherent rotation of the magnetic moment [77]. In contrast, our approach aims to exploit minor hysteresis loops to achieve discrete tuning of the device, going beyond simple binary switching, and thus seek an alternative to the SQUID in transmon architecture, allowing transitions between discrete steps that mimic continuous behavior. This strategy would eliminate the need for a static magnetic field during qubit operations, which could otherwise affect the qubit coherence [77].

Taking this into account, we have thus characterized the F film through a vibrating sample magnetometer (Section 3.2) to examine the impact of Nb doping on its magnetic properties. The measurement with the magnetometer showed that an increased Nb content in the FeNiGd alloy resulted in a reduction of the saturation magnetization, as illustrated in Figures 4.7 and 4.8.

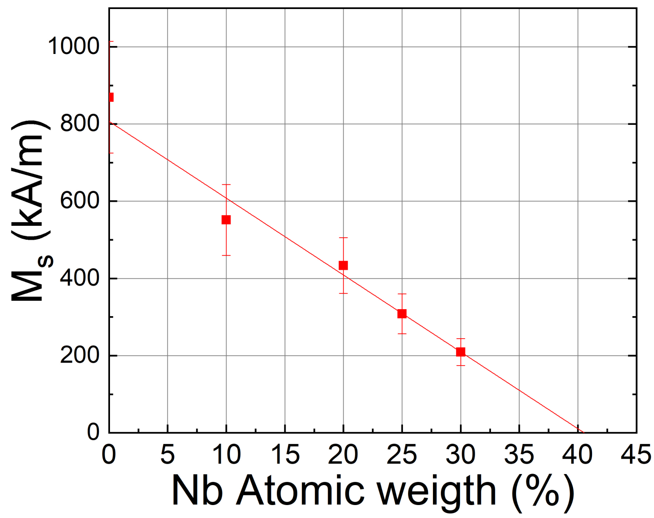

Figure 4.8: Graph depicting the saturation magnetization in relation to various Nb doping levels in a FeNiGd alloy with a 6 nm thickness. Error bars are calculated from the roughness-to-thickness ratio, approximately 16.7% of M_S. The red trend line represents the linear fit, intersecting zero at 40.5% Nb, indicating the maximum doping limit.

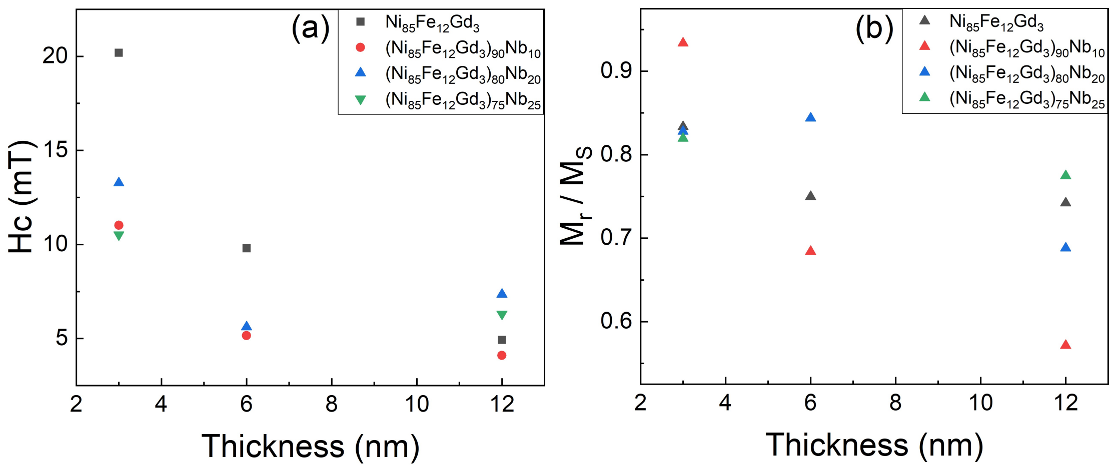

Figure 4.9: Dependence of magnetic properties on film thickness and Nb doping. (a) A consistent reduction in H_c is observed with increasing Nb content, indicating a softening of the magnetic material. (b) The M_r/M_s ratio decreases with thickness, reflecting changes in domain wall dynamics [95].

As shown in Figure 4.9, magnetization and coercive field decrease across all thicknesses with increasing Nb doping. The reduction in coercive field suggests that the magnetization process is dominated by domain wall motion rather than rotation [96]. This behavior is advantageous for reducing hysteresis losses and enabling low-field control, such as at 5 mT. Similar effects of Nb doping, such as a reduction in coercive fields and an enhancement of material susceptibility, have been reported in the literature for other diluted thin ferromagnetic systems [97].

The magnetic properties of thin films, particularly coercivity (H_C), are strongly influenced by structural imperfections, such as surface roughness and defects. Surface roughness, which in this study is approximately 1 nm (Figure 3.12), acts as pinning sites for domain walls. These pinning effects are known to increase coercivity, as domain walls require additional energy to overcome the barriers created by roughness and defects [96, 98]. When surface roughness is significant relative to the film thickness, it disrupts the smooth propagation of domain walls, leading to higher coercivity. This effect is particularly pronounced in thinner films, where the roughness-to-thickness ratio is larger. For instance, in NiFeCr alloys, it has been observed that coercivity increases more rapidly in thinner films due to enhanced pinning by defects and surface irregularities [96], consistent with the data shown for 3 nm-thick films in Figure 4.9. Similarly, in Cu-permalloy alloys, surface roughness and grain boundaries have been shown to contribute to domain wall pinning, resulting in higher coercivity values [97]. The addition of Nb to the FeNiGd alloy likely mitigates some of these effects by reducing the overall magnetic anisotropy and softening the material, as evidenced by the decrease in coercivity with increasing Nb content (Figure 4.9). This softening effect is consistent with findings in other alloy systems, where doping with non-magnetic elements reduces the influence of defects and surface roughness on domain wall dynamics [97]. Following the analysis of major hysteresis loops, we examined minor hysteresis loops at 5 mT, with data presented in Figure 4.10. From the analysis of Figure 4.9,

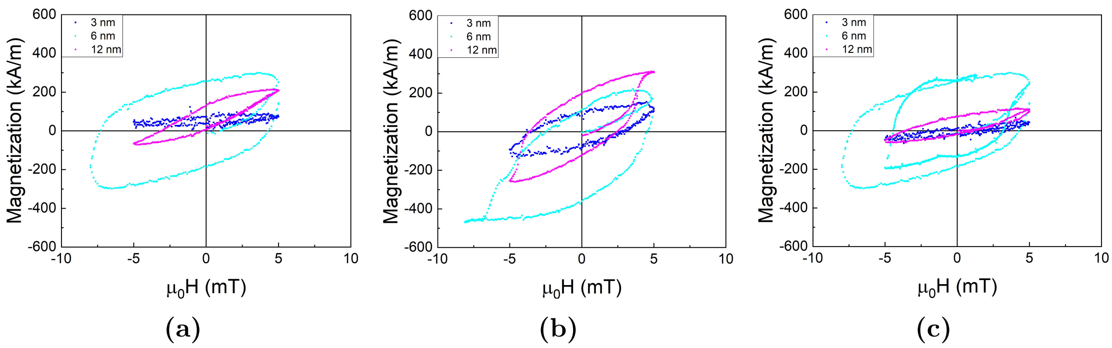

Figure 4.10: Magnetic hysteresis curves for $Ni_{85}Fe_{12}Gd_3$ (a) and $(Ni_{85}Fe_{12}Gd_3)_{1-x}Nb_x$ samples with 10% (b) and 20% (c) Nb, measured at thicknesses of 3 nm, 6 nm, and 12 nm. Among the samples, the 6-nm-thick films exhibit a balance between reduced coercive field and sufficient magnetization, suggesting this thickness as the optimal choice for low-field control applications.

which illustrates the thickness-dependent trends in coercive field and magnetization, and the minor loops shown in Figure 4.10, we identified the 6-nm-thick film with 20% Nb doping as the most suitable candidate for realizing a SIsFS JJs in the perspective of the ferrotrasmon. This specific composition and thickness provide a balanced combination of soft magnetic properties and sufficient magnetization. Most importantly, the asymmetry in the minor loops suggests that magnetization reversal can be selectively driven by field pulses of alternating polarity, bypassing the need for static bias fields. Future work could explore further reducing surface roughness or optimizing the film microstructure to minimize the impact of defects, potentially leading to even lower coercivity and improved device performance [99].

4.3 Characterization of in-plane magnetic flux line on-chip

Although the use of coils did not limit the experimental investigation of magnetic Josephson junctions, they are not ideal for implementing scalable quantum processing units. A coil-generated magnetic field would affect all qubits simultaneously, which is undesirable. Each qubit requires a dedicated line for localized tuning. Therefore, a key step towards the validation of the ferro-transmon is to find circuit solutions capable of generating in-plane magnetic fields that are compatible with both the required dimensions and magnetic strength parameters. This is a relatively uncommon requirement, as the magnetic field direction for flux-tunable transmons is typically perpendicular to the chip, generated by a superconducting 50 Ω-matched transmission line inductively coupled to the transmon DC-SQUID.
Given the limitations of traditional designs, we developed a novel flux line in collaboration with Quantware. The proposed design includes a Helmholtz coil structure integrated on-chip as shown in Figure 4.11 [99]. This innovative solution enables the generation of an in-plane magnetic field sufficient for the ferrotransmon while maintaining device coherence. The coil is designed as a single bridge structure, expected to produce approximately 1 mT per 10 mA of current (Figure 4.11b). To characterize this new design, a tunnel Al/AlO$_x$/Al Josephson junction with an active area of 36 μm^2 was fabricated by standard shadow mask evaporation technique [100] beneath the bridge. The junction consists of a 35-nm-thick bottom aluminum electrode, thermally oxidized to form the insulating barrier, followed by a 150-nm-thick top aluminum layer. The flux coil itself comprises a 150-nm-thick NbTiN base layer and a 500-nm-thick aluminum-titanium-aluminum (Al/Ti/Al) top layer, patterned via electron-beam lithography and etched to form the 3D bridge structure. Fabrication included a reflow process to achieve rounded bridge profiles, ensuring electrical continuity and mechanical stability. Simulations [99] demonstrated reasonable magnetic field uniformity across the junction area, critical for consistent switching behavior.

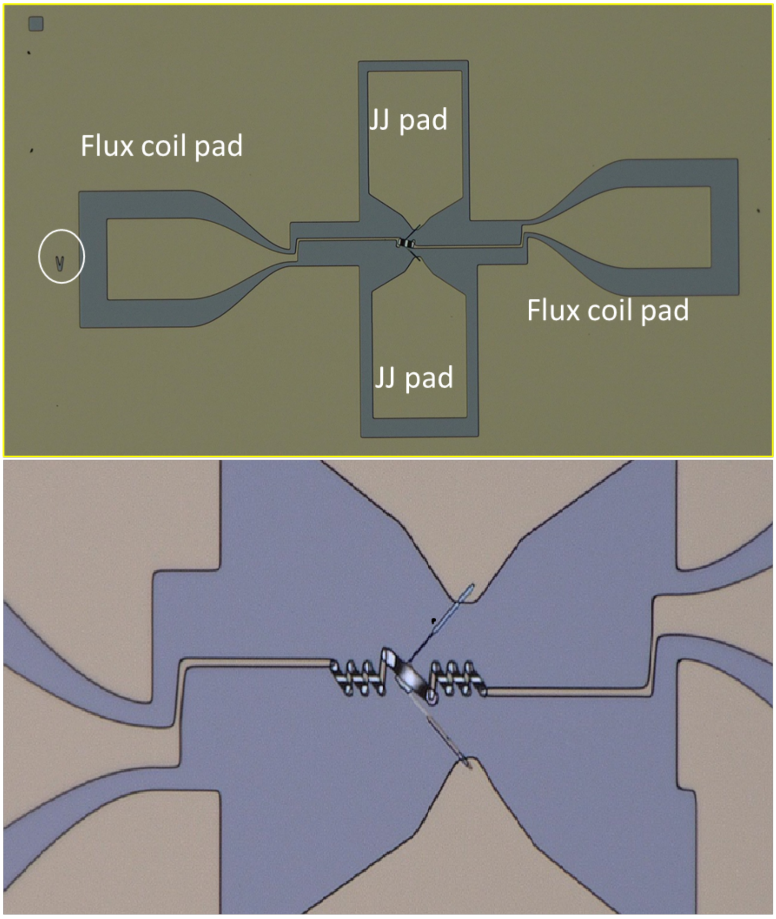

Figure 4.11: (above) Optical image showcasing the entire device, the top-bottom pads are contacts for the Josephson junction, meanwhile the left-right pads are the contacts for the airbridge; (below) Magnified image highlighting the Josephson junction and the airbridge, delineated in black.

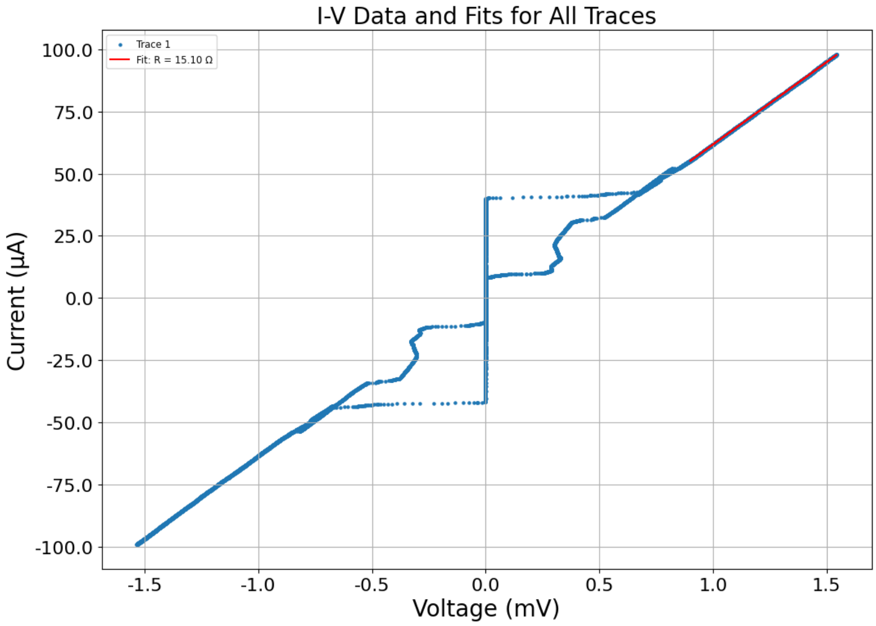

Figure 4.12: I-V characteristic at the base temperature of 17 mK for the SIS junction with an area of 36 μm^2 (Al (35 nm)/AlO_x /Al (150 nm).

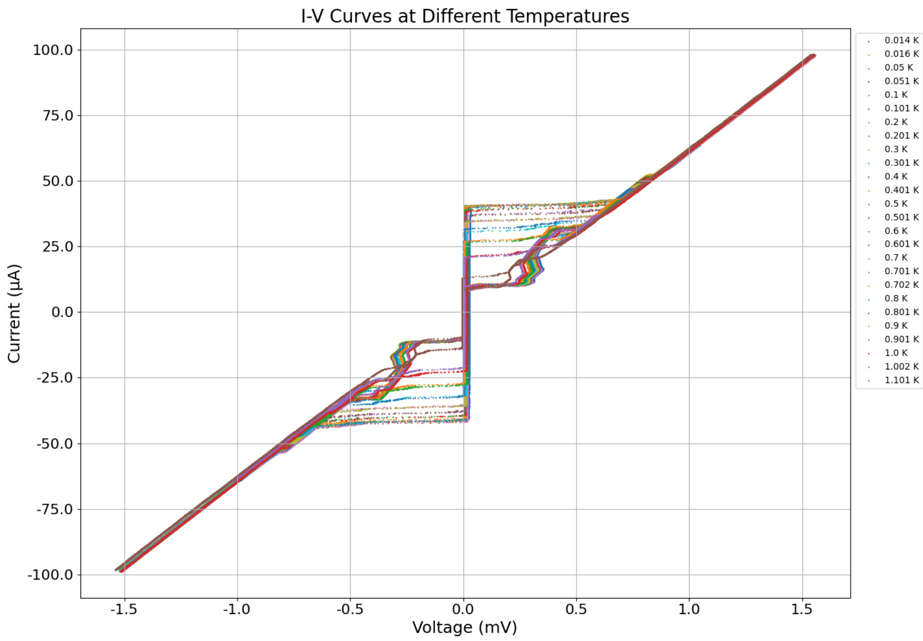

Figure 4.13: The temperature-dependent I-V characteristics of the SIS junction are presented.

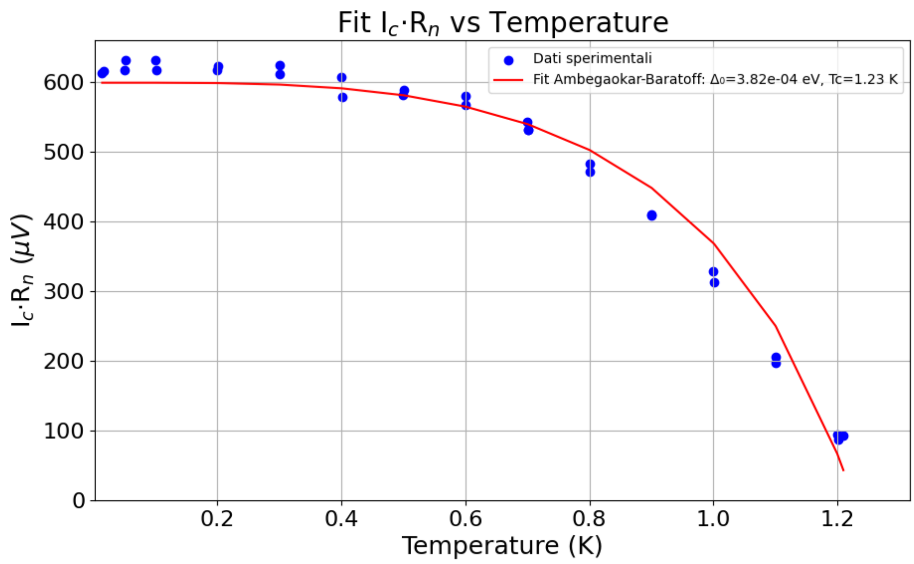

Figure 4.14: Plot of the evolution of $I_C R_N$ as a function of the temperature. The dataset for the square SIS junction, having an area of 36 μm^2 (Al (35 nm)/AlO$_x$ /Al (150 nm), is represented in blue. The fitting curve, depicted in red, has been determined using equation 4.2.

A (μm^2)	**J$_c$ (A/cm^2)**	**R$_N$ (Ω)**	**I$_c$R$_N$ (μV)**	**Q factor**	**E$_J$ (meV)**
36	110 ± 10	15.1 ± 0.5	608 ± 12	6	83 ± 14

Table 4.2: Parameters of the SIS Josephson junction. The quality factor $Q = \pm 1$ is calculated using the relation $Q = \sqrt{2eI_cR_N^2C/\hbar}$, where the capacitance C is derived from the empirical relation established in [81].

A micrometer-scale junction is necessary to observe a first minimum in the Fraunhofer pattern at a small magnetic field, thus providing better resolution for airbridge calibration. The lateral size of the junction fabricated to test the airbridge is thus 6 μm; however, the shadow mask evaporation method used for fabrication is more suitable for submicron junctions [101]. In micrometer-scale geometries, limited resist thickness leads to overlapping electrode layers that extend beyond the intended junction area, creating parasitic current paths. The absence of oxide surrounding the junction also allows leakage currents outside the barrier, which affects the retrapping branch (Figure 4.12). The measurements of the I-V curves by varying the temperature in Figure 4.13 has the primary goal to investigate whether non-filtered control lines the on-chip flux lines introduced undesired thermal effects, such as Joule heating that could suppress the critical current or add noise. Notably, the Ambegaokar-Baratoff behavior in Figure 4.14 confirms that the junction transport properties remain thermally unaffected up to approximately 0.5 K. This allows us to definitively attribute deviations of the critical current to the applied magnetic field from the on-chip coil (Figure 4.15), rather than parasitic heating or fabrication defects. The lack of secondary lobes in Figure 4.15 is precisely due to the fact that the current was limited to 5 mA to avoid excessive heating, as the system temperature increased by 0.5 K above this current level.

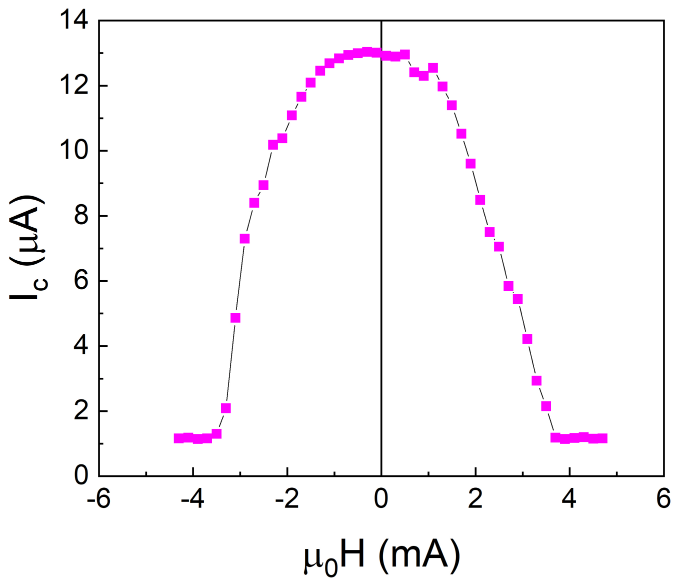

Figure 4.15: Dependence of I_C on the magnetic field generated by the on-chip airbridge at 17 mK. The SIS junction, with an area of 36 μm^2 (Al (35 nm)/AlO_x/Al (150 nm)), is aligned parallel to the field.

Measurements using the airbridge-generated field at 17 mK have been compared to coil-generated field data at both 45° junction alignments (Figure 4.16) and 0° (Figure 4.17). A Fraunhofer fit was applied to the normalized I_C(H) curves, specifically to resolve the minima positions and quantify field uniformity.

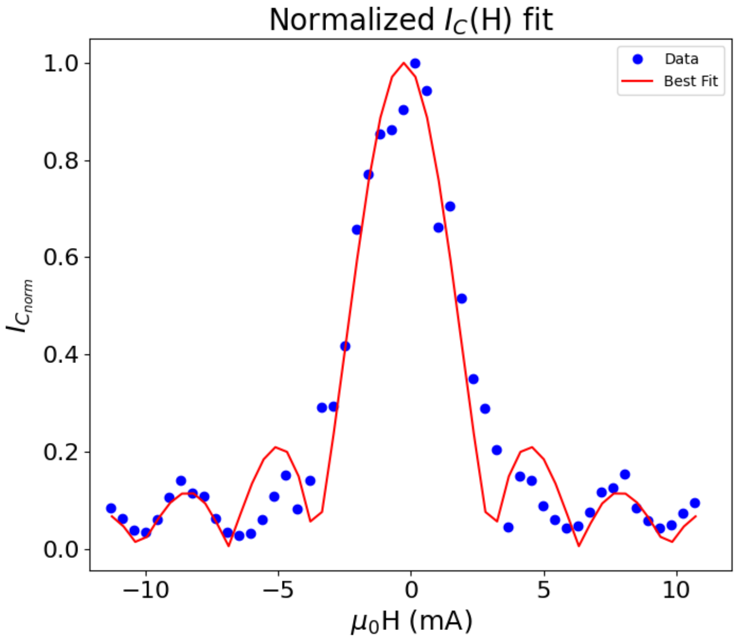

Figure 4.16: Normalized dependence of I_C on the magnetic field generated by an external coil at 17 mK. The SIS junction, with an area of 36 μm^2 (Al (35 nm)/AlO_x/Al (150 nm)), is oriented at a 45° angle relative to the field. In red, the Fraunhofer pattern is represented.

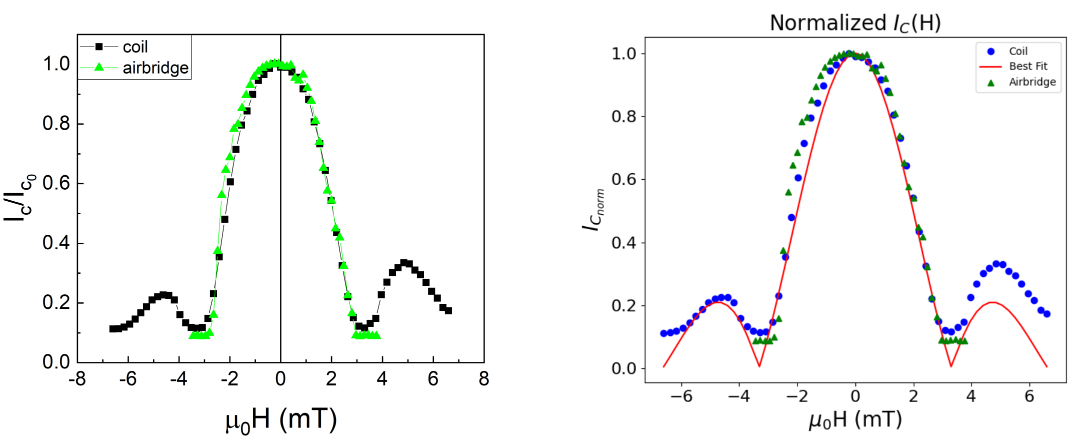

(a) **(b)**

Figure 4.17: (a) Comparison of I_C dependence on the magnetic field for the airbridge and external coil at 17 mK, with the SIS junction (area 36 μm^2, Al (35 nm)/AlO_x/Al (150 nm)) aligned parallel to the field. (b) Fit of the normalized I_C(H) curve, showing experimental data (blue points) and the best-fit curve (red line).

The characterization of on-chip airbridges (Figs. 4.15 and 4.17) reveals critical parameters for ferrotransmon implementation. The measured field conversion efficiency, 1.25 mA $\rightarrow$ 1 mT, shows a slight deviation from the simulated 10 mA $\rightarrow$ 1 mT ratio. This discrepancy may arise from factors unaccounted in the simulations, such as the kinetic inductance contribution of the junction itself or magnetic field redistribution due to the Meissner effect in the superconducting electrodes, which could compress the field geometry. While the normalized $I_C(H)$ curve aligns well with experimental data, further studies are required to fully resolve the quantitative mismatch. The airbridge generates sufficient in-plane magnetic fields (approximately 5 mT) to control the $Ni_{85}Fe_{12}Gd_3$/Nb ferromagnetic interlayer, while preserving the superconducting state of the Al electrodes ($H_c^{\mathrm{Al}} \approx 10$ mT). This correlates with the observed decrease in coercive field noted in VSM measurements (Fig. 4.10c), where an H_c of ≈ 5 mT was obtained through Nb doping. In summary, the experimental investigations discussed in this chapter address critical challenges in realizing the ferrotransmon architecture, yielding the following key results:

- It has been demonstrated that SIsFS junctions exhibit comparable transport properties (critical current I_C, normal resistance R_N, and gap voltage V_{gap}) to conventional SIS junctions, with $I_C R_N \approx$ 75-78 μV and $E_J \approx$ 21-22 GHz, suitable for transmon qubits. Most importantly, the working functioning in Mode 1 (a), where the SIsFS behaves as a serial connection of a SIs and sFS enables the integration of ferromagnetic layers without degrading the tunnel properties.

- Coercive fields (H_C) were reduce in NiFeGd alloys through Nb doping, achieving $H_C \approx 5$ mT for 6-nm-thick $(Ni_{85}Fe_{12}Gd_3)_{80}Nb_{20}$. The asymmetric minor hysteresis loops at low fields (~ 5 mT) will pave the way for a tuning of the critical current states of JJs incorporating this material at zero-bias static field.

- A novel airbridge flux line generating in-plane magnetic fields (~ 1 mT per 1.25 mA) has been developed compatible with Al electrodes ($H_c^{\mathrm{Al}} \approx 10$ mT). The field uniformity and efficiency via Fraunhofer pattern analysis confirms compatibility with ferrotransmon requirements.

Conclusion

In the quest for scalable quantum computing architectures, conventional Josephson junctions face fundamental limitations, including flux noise, quasiparticle dissipation, and the inability to integrate localized magnetic control. These challenges have hindered progress toward fault-tolerant quantum processors requiring precise, low-noise tunability. In this scenario, SIsFS junctions could play a crucial role, as they synergize superconducting coherence with magnetic functionality. Unlike SQUID-based systems, which rely on external flux lines prone to crosstalk, SIsFS junctions intrinsically embed ferromagnetic layers enabling on-chip magnetic control of Josephson energy (E_J) through magnetic field pulses, thus in principle removing the use of a static field during qubit operation.

The central objective of this thesis was to establish these junctions as a promising platform for the ferrotransmon qubit by addressing critical challenges in material design, magnetic tunability, and on-chip integration. To this end, the development of a novel ferromagnetic alloy was crucial. By employing engineered $(Ni_{85}Fe_{12}Gd_3)_{80}Nb_{20}$, we have demonstrated a reduction of coercive fileds to $H_C \sim 5$ mT via Nb doping. Structural analyses revealed that reduced surface roughness (~ 1 nm) and minimized defect-mediated pinning further optimized magnetic response, ensuring reliable switching with retained remanence ($M_r/M_s \sim 0.85$). This softening was due to enhanced domain wall motion over coherent rotation of the magnetic moment. Moreover, it facilitated precise low field control, making this devices suitable for scalable quantum systems.

Besides material innovation, an on-chip Helmoltz flux coil was designed to generate in-plane magnetic fields with a conversion efficiency of ≈ 1.25 mT/mA. Experimental validation confirmed the airbridge's seamless integration, preserving the Ambegaokar-Baratoff regime and introducing no measurable dissipation or thermal noise. This advancement eliminates reliance on external coils, mitigating crosstalk and enhancing scalability. Critically, the integration of an on-chip coil per qubit ensures that each device has its own dedicated flux line, which is essential for independent and precise magnetic control in multi-qubit architectures.

For quantum applications, these innovations position SIsFS junctions as a transformative alternative to SQUID-based transmons. By leveraging minor hysteresis loops, quasi-continuous tunability of Josephson energy (E_J) can be achieved, approximating densely spaced states for high-fidelity operations. The junctions address persistent challenges like flux noise, inductive heating, and limited tunability.

Looking forward, future work will focus on refining ferromagnetic layer microstructures to further suppress coercivity, alongside noise spectroscopy to disentangle magnetic and quasiparticle contributions to decoherence.

Bibliography

[1] Charles P. Poole, Horacio A. Farach, Richard J. Creswick, and Ruslan Prozorov. 12 - type ii superconductivity. In C. P. Poole, H. A. Farach, R. J. Creswick, and R. Prozorov, editors, Superconductivity (Second Edition), pages 337 – 383. Academic Press, Amsterdam, second edition edition, 2007.

[2] P. Mangin and R. Kahn. LONDON THEORY, pages 13–48. Springer Cham, 12 2017.

[3] V. L. Ginzburg and L. D. Landau. On the Theory of superconductivity. Zh. Eksp. Teor. Fiz., 20:1064–1082, 1950.

[4] LP Gor'Kov. On the energy spectrum of superconductors. Sov. Phys. JETP, 7(505):158, 1958.

[5] Philip W. Anderson. Higgs, anderson and all that. Nature Physics, 11(2):93–93, Feb 2015.

[6] L P Gor'kov. Microscopic derivation of the ginzburg–landau equations in the theory of superconductivity. Sov. Phys. - JETP (Engl. Transl.); (United States), 9-6, 1 1959.

[7] M. Tinkham. Introduction to Superconductivity: Second Edition. Dover Books on Physics. Dover Publications, 2004.

[8] A. Barone and G. Paternò. Physics and applications of the Josephson effect. UMI Out-of-Print Books on Demand. Wiley, 1982.

[9] P. W. Anderson and J. M. Rowell. Probable observation of the josephson superconducting tunneling effect. Phys. Rev. Lett., 10:230–232, Mar 1963.

[10] K. K. Likharev. Superconducting weak links. Rev. Mod. Phys., 51:101–159, Jan 1979.

[11] K. K. Likharev. Dynamics of Josephson Junctions and Circuits. Gordon and Breach Science Publishers, 1986.

[12] R. Gross and A. Marx. Physics of Josephson Junctions: The Voltage State. Walther-Meißner-Institut, 2021. Discusses characteristic frequencies and picosecond-scale dynamics in conventional Josephson junctions.

[13] P. S. Lomdahl, O. H. Soerensen, and P. L. Christiansen. Soliton excitations in josephson tunnel junctions. Phys. Rev. B, 25:5737–5748, May 1982.

[14] A. Zorin, K. Likharev, and S. Turovets. Dynamics of josephson tunnel junctions with a finite-width riedel peak. IEEE Transactions on Magnetics, 19(3):629–632, 1983.

[15] M. Zgirski, S. Kafanov, J. Burnett, T. Nieminen, and A. Tzalenchuk. Efficient quasiparticle traps with low dissipation through gap engineering. Physical Review B, 100:144514, Oct 2019.

[16] R. Benevides, M. Drimmer, G. Bisson, F. Adinolfi, U. v. Lüpke, H. M. Doeleman, G. Catelani, and Y. Chu. Quasiparticle dynamics in a superconducting qubit irradiated by a localized infrared source. Phys. Rev. Lett., 133:060602, Aug 2024.

[17] H. A. Kramers. Brownian motion in a field of force and the diffusion model of chemical reactions. Physica, 7(4):284–304, 1940.

[18] P. Hanggi, P. Talkner, and M. Borkovec. Reaction-rate theory: fifty years after kramers. Rev. Mod. Phys., 62:251, 1990.

[19] A. J. Leggett. Macroscopic quantum systems and the quantum theory of measurement. Prog. Theor. Phys. Suppl., 69:80–100, 1980.

[20] A. J. Leggett et al. Dynamics of the dissipative two-state system. Reviews of Modern Physics, 59(1):1–85, 1987.

[21] J. Clarke and F. K. Wilhelm. Superconducting quantum bits. Nature, 453(7198):1031–1042, 2008.

[22] T.T. Heikkilä. The Physics of Nanoelectronics: Transport and Fluctuation Phenomena at Low Temperatures. Oxford Master Series in Physics. OUP Oxford, 2013.

[23] Alexandre Blais, Arne L. Grimsmo, Steven M. Girvin, and Andreas Wallraff. Circuit quantum electrodynamics. Reviews of Modern Physics, 93(2):025005, 2021.

[24] S. E. Nigg, S. M. Girvin, et al. Black-box superconducting circuit quantization. Physical Review Letters, 108:240502, 2012.

[25] M. H. Devoret and R. J. Schoelkopf. Superconducting circuits for quantum information: An outlook. Science, 339(6124):1169–1174, 2013.

[26] P. Krantz, M. Kjaergaard, F. Yan, T. P. Orlando, S. Gustavsson, and W. D. Oliver. A quantum engineer's guide to superconducting qubits. arXiv preprint arXiv:1904.06560v5, 2021.

[27] J. Koch, T. M. Yu, J. Gambetta, A. A. Houck, D. I. Schuster, J. Majer, A. Blais, M. H. Devoret, S. M. Girvin, and R. J. Schoelkopf. Charge-insensitive qubit design derived from the cooper pair box. Physical Review A, 76(4):042319, 2007.

[28] J. A. Schreier, A. A. Houck, J. Koch, D. I. Schuster, B. Johnson, J. M. Chow, J. M. Gambetta, J. Majer, L. Frunzio, M. H. Devoret, et al. Suppressing charge noise decoherence in superconducting charge qubits. Physical Review B, 77(18):180502, 2008.

[29] M. Kjaergaard, M. E. Schwartz, J. Braumüller, P. Krantz, J. I.-J. Wang, S. Gustavsson, and W. D. Oliver. Superconducting qubits: Current state of play. Annual Review of Condensed Matter Physics, 11(Volume 11, 2020):369–395, 2020.

[30] R. Kleiner et al. Superconducting quantum interference devices: state-of-the-art and applications. Proceedings of the IEEE, 92(10):1533–1547, 2004.

[31] Stephen J. Blundell. Magnetism in Condensed Matter. Oxford University Press, 2001.

[32] N. Goldenfeld. Lectures on Phase Transitions and the Renormalization Group. Addison-Wesley, 1992.

[33] C. Kittel. Introduction to Solid State Physics. Wiley, 8th edition, 2004.

[34] S.R. Trout, B.D. Cullity, and C.D. Graham. Introduction to Magnetic Materials. Wiley, 2024.

[35] R. M. Bozorth. Ferromagnetism. Wiley-IEEE Press, 1993.

[36] R. Evans, S. Jenkins, A. Meo, L.E. Elliott, S.K. Piotrowski, M. Bapna, R.W. Chantrell, and S.A. Majetich. Magnetic stray fields in nanoscale magnetic tunnel junctions. Journal of Physics D: Applied Physics, 53(4):044001, 2019. ArXiv preprint available: `https://arxiv.org/abs/1907.11798`.

[37] J. M. D. Coey. Magnetism and Magnetic Materials. Cambridge University Press, 2010.

[38] G.Y. Chin. New developments in technologically important magnetic materials. Journal of Magnetism and Magnetic Materials, 9(4):283–298, 1978.

[39] N. O. Birge and N. Satchell. Ferromagnetic materials for josephson π junctions. APL Materials, 12(4):041105, 04 2024.

[40] A. I. Buzdin. Proximity effects in superconductor-ferromagnet heterostructures. Rev. Mod. Phys., 77:935–976, 2005.

[41] G. E. Blonder, M. Tinkham, and T. M. Klapwijk. Transition from metallic to tunneling regimes in superconducting microconstrictions: Excess current, charge imbalance, and supercurrent conversion. Physical Review B, 25(7):4515, 1982.

[42] R. J. Soulen, J. M. Byers, M. S. Osofsky, B. Nadgorny, T. Ambrose, S. F. Cheng, P. R. Broussard, C. T. Tanaka, J. Nowak, J. S. Moodera, et al. Measuring the spin polarization of a metal with a superconducting point contact. Science, 282(5386):85–88, 1998.

[43] A. I. Larkin and Yu. N. Ovchinnikov. Inhomogeneous state of superconductors. Soviet Physics JETP, 20:762, 1964.

[44] P. Fulde and R. A. Ferrell. Superconductivity in a strong spin-exchange field. Physical Review, 135(3A):A550, 1964.

[45] F. S. Bergeret, A. F. Volkov, and K. B. Efetov. Odd triplet superconductivity and related phenomena in superconductor-ferromagnet structures. Reviews of Modern Physics, 77(4):1321–1373, 2005.

[46] V. V. Ryazanov, V. A. Oboznov, A. Y. Rusanov, A. V. Veretennikov, A. A. Golubov, and J. Aarts. Coupling of two superconductors through a ferromagnet: Evidence for a π junction. Phys. Rev. Lett., 86:2427–2430, Mar 2001.

[47] E. A. Demler, G. B. Arnold, and M. R. Beasley. Superconducting proximity effects in magnetic metals. Phys. Rev. B, 55:15174–15182, Jun 1997.

[48] A.S. Sidorenko, V.I. Zdravkov, A.A. Prepelitsa, C. Helbig, Y. Luo, S. Gsell, M. Schreck, S. Klimm, S. Horn, L.R. Tagirov, and R. Tidecks. Oscillations of the critical temperature in superconducting nb/ni bilayers. Annalen der Physik, 515(1-2):37–50, 2003.

[49] V. I. Zdravkov, J. Kehrle, G. Obermeier, S. Gsell, M. Schreck, C. Müller, H.-A. Krug von Nidda, J. Lindner, J. Moosburger-Will, E. Nold, R. Morari, V. V. Ryazanov, A. S. Sidorenko, S. Horn, R. Tidecks, and L. R. Tagirov. Reentrant superconductivity in superconductor/ferromagnetic-alloy bilayers. Phys. Rev. B, 82:054517, Aug 2010.

[50] A. A. Golubov, M. Yu. Kupriyanov, and E. Il'ichev. The current-phase relation in josephson junctions. Rev. Mod. Phys., 76:411–469, Apr 2004.

[51] A. K. Feofanov, V. A. Oboznov, V. V. Bol'ginov, V. V. Ryazanov, A. N. Rossolenko, M. I. Khabipov, D. Balashov, A. B. Zorin, J. Niemeyer, A. V. Ustinov, et al. Implementation of superconductor/ferromagnet/superconductor π-shifters in superconducting digital and quantum circuits. Nature Physics, 6(8):593–597, 2010.

[52] T. Yahamashita and colleagues. Advanced phase control in superconducting quantum circuits using ferromagnetic junctions. Physical Review Applied, 21:034015, 2024.

[53] E. Goldobin, D. Koelle, R. Kleiner, and A. Buzdin. Josephson junctions with second harmonic in the current-phase relation: Properties of φ junctions. Phys. Rev. B, 76:224523, Dec 2007.

[54] H. Sickinger, A. Lipman, M. Weides, R. G. Mints, H. Kohlstedt, D. Koelle, R. Kleiner, and E. Goldobin. Experimental evidence of a φ josephson junction. Phys. Rev. Lett., 109:107002, Sep 2012.

[55] T. S. Khaire, W. P. Pratt, and N. O. Birge. Critical current behavior in josephson junctions with the weak ferromagnet pdni. Phys. Rev. B, 79:094523, Mar 2009.

[56] V. V. Bol'ginov, V. S. Stolyarov, D. S. Sobanin, A. L. Karpovich, and V. V. Ryazanov. Magnetic switches based on nb-pdfe-nb josephson junctions with a magnetically soft ferromagnetic interlayer. Journal of Experimental and Theoretical Physics Letters, 95(7):366–371, 2012.

[57] H. G. Ahmad, V. Brosco, A. Miano, L. Di Palma, M. Arzeo, D. Montemurro, P. Lucignano, G. P. Pepe, F. Tafuri, R. Fazio, and D. Massarotti. Hybrid ferromagnetic transmon qubit: Circuit design, feasibility, and detection protocols for magnetic fluctuations. Phys. Rev. B, 105:214522, Jun 2022.

[58] S. V. Bakurskiy, N. V. Klenov, I. I. Soloviev, V. V. Bol'ginov, V. V. Ryazanov, I. V. Vernik, O. A. Mukhanov, M. Yu. Kupriyanov, and A. A. Golubov. Theoretical model of superconducting spintronic SIsFS devices. Applied Physics Letters, 102(19):192603, 05 2013.

[59] T. I. Larkin, V. V. Bol'ginov, V. S. Stolyarov, V. V. Ryazanov, I. V. Vernik, S. K. Tolpygo, and O. A. Mukhanov. Ferromagnetic josephson switching device with high characteristic voltage. Applied Physics Letters, 100(22):222601, 05 2012.

[60] M. D. Hutchings, J. B. Hertzberg, Y. Liu, N. T. Bronn, G. A. Keefe, Markus Brink, Jerry M. Chow, and B. L. T. Plourde. Tunable superconducting qubits with flux-independent coherence. Phys. Rev. Appl., 8:044003, Oct 2017.

[61] L. Parlato, R. Caruso, A. Vettoliere, R. Satariano, H. G. Ahmad, A. Miano, D. Montemurro, D. Salvoni, G. Ausanio, F. Tafuri, G. P. Pepe, D. Massarotti, and C. Granata. Characterization of scalable josephson memory element containing a strong ferromagnet. Journal of Applied Physics, 127(19):193901, 05 2020.

[62] Polytechnic of Porto School of Engineering. Sputtering physical vapour deposition (pvd) coatings: A critical review on process improvement and market trend demands. Coatings, 8(11):402, 2018.

[63] V. Bol'Ginov, V. Stolyarov, D. Sobanin, A. Karpovich, and V. Ryazanov. Magnetic switches based on nb–pdfe–nb josephson junctionswith a magnetically soft ferromagnetic interlayer. JETP Letters, 95:366–371, 06 2012.

[64] M. Hughes. What is sputtering? magnetron sputtering? Semicore Equipment, Inc, November 2014.

[65] A. Palmero and N. Martin. Advanced strategies in thin films engineering by magnetron sputtering. Coatings, 10(4), 2020.

[66] Thermo Fisher Scientific. Sem resolution | scanning electron microscopy.

[67] G. Binnig, H. Rohrer, C. Gerber, and E. Weibel. Surface studies by scanning tunneling microscopy. Physical review letters, 49(1):57, 1982.

[68] B. Bhushan. Springer handbook of nanotechnology. Springer Science & Business Media, 2010.

[69] S. Foner. Vibrating sample magnetometer. Review of Scientific Instruments, 27(7):548–548, 07 1956.

[70] R. Radebaugh. Historical Summary of Cryogenic Activity Prior to 1950, pages 3–27. Springer New York, New York, NY, 2007.

[71] P. Das, R. B. de Ouboter, and K. W. Taconis. A realization of a london-clarke-mendoza type refrigerator. In J. G. Daunt, D. O. Edwards, F. J. Milford, and M. Yaqub, editors, Low Temperature Physics LT9, pages 1253–1255, Boston, MA, 1965. Springer US.

[72] A. Vettoliere, R. Satariano, R. Ferraiuolo, L. Di Palma, H. G. Ahmad, G. Ausanio, G. P. Pepe, F. Tafuri, D. Montemurro, C. Granata, L. Parlato, and D. Massarotti. Aluminum-ferromagnetic josephson tunnel junctions for high quality magnetic switching devices. Applied Physics Letters, 120(26):262601, 06 2022.

[73] J. C. Lee, W. D. Oliver, K. K. Berggren, and T. P. Orlando. Nonlinear resonant behavior of a dispersive readout circuit for a superconducting flux qubit. Phys. Rev. B, 75:144505, Apr 2007.

[74] J. Lisenfeld, A. Lukashenko, M. Ansmann, J. M. Martinis, and A. V. Ustinov. Temperature dependence of coherent oscillations in josephson phase qubits. Phys. Rev. Lett., 99:170504, Oct 2007.

[75] E. Hoskinson, F. Lecocq, N. Didier, A. Fay, F. W. J. Hekking, W. Guichard, O. Buisson, R. Dolata, B. Mackrodt, and A. B. Zorin. Quantum dynamics in a camelback potential of a dc squid. Phys. Rev. Lett., 102:097004, Mar 2009.

[76] A. Vettoliere, R. Satariano, R. Ferraiuolo, L. Di Palma, H. G. Ahmad, G. Ausanio, G. P. Pepe, F. Tafuri, D. Massarotti, D. Montemurro, C. Granata, and . Parlato. High-quality ferromagnetic josephson junctions based on aluminum electrodes. Nanomaterials, 12(23), 2022.

[77] H. G. Ahmad, R. Satariano, R. Ferraiuolo, A. Vettoliere, C. Granata, D. Montemurro, G. Ausanio, L. Parlato, G. P. Pepe, F. Tafuri, and D. Massarotti. Phase dynamics of tunnel al-based ferromagnetic josephson junctions. Applied Physics Letters, 124(23):232601, 06 2024.

[78] J. Bardeen, L. N. Cooper, and J. R. Schrieffer. Microscopic theory of superconductivity. Phys. Rev., 106:162–164, Apr 1957.

[79] V. Ambegaokar and A. Baratoff. Tunneling between superconductors. Phys. Rev. Lett., 10:486–489, Jun 1963.

[80] I.O. Kulik. Magnitude of the critical josephson tunnel current. Journal of Experimental and Theoretical Physics (JETP), 22(4):841, 1966. Russian original - ZhETF, Vol. 49, No. 4, p. 1211, April 1966.

[81] M. Maezawa, M. Aoyagi, H. Nakagawa, I. Kurosawa, and S. Takada. Specific capacitance of nb/alox/nb josephson junctions with critical current densities in the range of 0.1–18 ka/cm2. Applied Physics Letters, 66(16):2134–2136, 04 1995.

[82] J. Koch, T. M. Yu, J. Gambetta, A. A. Houck, D. I. Schuster, J. Majer, A. Blais, M. H. Devoret, S. M. Girvin, and R. J. Schoelkopf. Charge-insensitive qubit design derived from the cooper pair box. Phys. Rev. A, 76:042319, Oct 2007.

[83] J. F. Cochran and D. E. Mapother. Superconducting transition in aluminum. Phys. Rev., 111:132–142, Jul 1958.

[84] I.A. Golovchanskiy, V. Bolginov, N. Abramov, V. Stolyarov, A. Ben-Hamida, V. Chichkov, D. Roditchev, and V. Ryazanov. Magnetization dynamics in dilute pd1-xfex thin films and patterned microstructures considered for superconducting electronics. Journal of Applied Physics, 120, 10 2016.

[85] O. Fruchart and A. Thiaville. Magnetism in reduced dimensions. Comptes Rendus. Physique, 6(9):921–933, 2005.

[86] E. C. Gingrich, P. Quarterman, Yixing Wang, R. Loloee, W. P. Pratt, and Norman O. Birge. Spin-triplet supercurrent in co/ni multilayer josephson junctions with perpendicular anisotropy. Phys. Rev. B, 86:224506, Dec 2012.

[87] A. Ruotolo, C. Bell, C. W. Leung, and M. G. Blamire. Perpendicular magnetic anisotropy and structural properties of nicu/cu multilayers. Journal of Applied Physics, 96(1):512–518, 07 2004.

[88] G. Wild, C. Probst, A. Marx, and R. Gross. Josephson coupling and fiske dynamics in ferromagnetic tunnel junctions. The European Physical Journal B, 78(4):509–523, Dec 2010.

[89] N. Satchell, T. Mitchell, P. M. Shepley, E. Darwin, B. J. Hickey, and G. Burnell. Pt and cob trilayer josephson π junctions with perpendicular magnetic anisotropy. Scientific Reports, 11(1):11173, May 2021.

[90] A. E. M. Qader, R. K. Singh, S. N. Galvin, L. Yu, J. M. Rowell, and N. Newman. Switching at small magnetic fields in josephson junctions fabricated with ferromagnetic barrier layers. Applied Physics Letters, 104(2):022602, 01 2014.

[91] B. M. Niedzielski, E. C. Gingrich, R. Loloee, W. P. Pratt, and N. O. Birge. S/f/s josephson junctions with single-domain ferromagnets for memory applications. Superconductor Science and Technology, 28(8):085012, jul 2015.

[92] B. Baek, W. H. Rippard, S. P. Benz, S. E. Russek, and P. D. Dresselhaus. Hybrid superconducting-magnetic memory device using competing order parameters. Nature Communications, 5(1):3888, May 2014.

[93] B. Baek, M. L. Schneider, M. R. Pufall, and W. H. Rippard. Phase offsets in the critical-current oscillations of josephson junctions based on ni and ni-$(\mathrm{ni}_{81}\mathrm{fe}_{19})_x\mathrm{nb}_y$ barriers. Phys. Rev. Appl., 7:064013, Jun 2017.

[94] C A F Vaz, J A C Bland, and G Lauhoff. Magnetism in ultrathin film structures. Reports on Progress in Physics, 71(5):056501, apr 2008.

[95] W. Zhao et al. Domain wall structure and dynamics in thin films: The role of surface roughness and structural factors. Journal of Applied Physics, 89:1325–1332, 2001.

[96] W. Joshua, S. M. Swapna, M. K. Robert, J. E. Nicholas, L. Reza, and O. B. Norman. Comparison of nifecr and nife in ferromagnetic josephson junctions, 2025.

[97] M. A. Qader, A. Vishina, L. Yu, C. Garcia, R.K. Singh, N.D. Rizzo, M. Huang, R. Chamberlin, K.D. Belashchenko, M. van Schilfgaarde, and N. Newman. The magnetic, electrical and structural properties of copper-permalloy alloys. Journal of Magnetism and Magnetic Materials, 442:45–52, 2017.

[98] G. Choe and M. Steinback. Surface roughness effects on magnetoresistive and magnetic properties of nife thin films. Journal of Applied Physics, 85(8):5777–5779, 04 1999.

[99] H. G. Ahmad, R. Ferraiuolo, G. Serpico, R. Satariano, A. Levochkina, A. Vettoliere, C. Granata, D. Montemurro, M Esposito, G. Ausanio, L. Parlato, G. P. Pepe, A. Bruno, F. Tafuri, and D. Massarotti. Towards novel tunability schemes for hybrid ferromagnetic transmon qubits, 2024.

[100] G. J. Dolan. Offset masks for lift-off photoprocessing. Applied Physics Letters, 31(5):337–339, 09 1977.

[101] E V. Moskalev23, D. O. an Zikiy, A. A. Pishchimova, D. A. Ezenkova, N. S. Smirnov, A. I. Ivanov, N. D. Korshakov, and I. A. Rodionov. Optimization of shadow evaporation and oxidation for reproducible quantum josephson junction circuits. Scientific Reports, 13(1):4174, 09 2023.